UNIVERSITY OF
LIVERPOOL

# Proof of Concept Study of a Semiconductor Compton Camera to Be Used for Prompt Gamma Ray Imaging During Proton Therapy

Thesis submitted in accordance with the requirements of
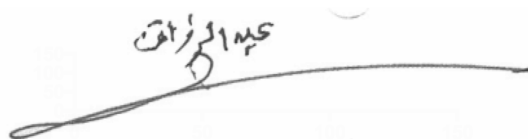the University of Liverpool for the degree of Doctor in Philosophy
by

**Hamed Alshammari**

Supervised by
**Professor Laura Harkness-Brennan**
&
**Professor Andrew Boston**

June, 2022

# Dedication

To my father: Abdulrzaq

عبد الرزاق

# Acknowledgements

First and foremost, I would like to express my deepest gratitude to my supervisors. A massive thanks goes to Professor Laura Harkness-Brennan, without whose support, guidance and encouragement, I would not have been able to overcome the challenges I faced in working on my thesis. You made my PhD journey a most rewarding experience for me. My thanks also go to Professor Andy Boston for his constructive comments and recommendations throughout my work.

Second, I want to thank Dr Dan Judson for his patient and supportive advice and for always being there when things became complicated. I am also grateful to Dr Ellis Rintoul and Dr Adam Caffrey for answering my endless questions about the Compton camera and to past and present members of the nuclear physics group, especially Dr Muneerah Alaqeel, Dr Jaimie Platt, Hannah Brown and Ahmad Alharbi, for their help.

Thanks must also go to my friends in Liverpool (Diwaniah group), who have always supported me. A special thanks goes to my close friend Meshal Alshammari, who, although thousands of kilometres away, was close enough to share a joke with me almost every day.

A special thanks go to my sponsor, Imam Abdulrahman bin Faisal University and my mentors, Dr Ghazi Alotaibi and Dr Ali Alghamdi, for their endless support.

Finally, but most importantly, I would like to extend my sincere appreciation to my family—to my mum, elder brother "Theyab", brothers and sisters, who always encouraged and believed in me; to my wife, Suad, who has always been by my side, sharing with me every moment of my life journey; and to my kids, Jinan, Hanan, Omar and Ghaith (the new arrival who started his life journey while I was writing these words), whose laughter and smiles brighten every day of my life.

# Abstract

Protons are used in radiation therapy of cancerous tissue as they have the potential benefit of sparing dose to healthy tissue. Given the accuracy of the proton beam range and treatment plan uncertainties, a large safety margin has been used in planning and delivery. Using the prompt gamma (PG) for range verification and the monitoring of dose delivery in real-time is proposed to provide better control of beam direction and reduce currently used safety margins. A gamma-ray imaging system (Gri+) that includes a three-tier semiconductor Compton camera system has been evaluated to assess its potential to image prompt $\gamma$ rays emitted during proton therapy. This work has been able to show the imaging capabilities of the Gri+ system for high-energy $\gamma$ ray and propose sets of operational recommendations for future measurements in the proton radiotherapy facility. The Gri+ system can successfully image a high-energy $\gamma$-ray of 1.8 MeV for single and multiple interaction events in the system. This significantly increases the Gri+ system imaging efficiency from 27 % to 70 % but degrades the imaging resolution. Using an offline algorithm can mitigate the image resolution degradation. The image resolution was 7.2 $\pm$ 0.6 mm and 10.5 $\pm$ 0.8 mm for single and multiple interaction events in the system, respectively. The Gri+ system shows a limited count rate capability that can be linked to digitiser cards within the digital data acquisition system. The maximum Compton imaging rate that the Gri+ system could process is 1400 CPS. There is a critical situation where the system loses the ability to process the Compton imaging events at a true count rate of 49k CPS. A collaboration with the manufacturer is recommended to rectify the count rate loss issue and a minor modification to data processing hardware to maximise the operational energy range. A preliminary analysis of the operational environment in a proton therapy delivery room has also been undertaken using data that was available from Clatterbridge Cancer Centre. Results of the work have been used to inform the proposal of a systematic set of data for full evaluation in future work.

# Contents

# List of Figures

ix

xi

xiii

# List of Tables

# Chapter 1

# Introduction

Proton therapy is an emerging technique for the treatment of cancer. Recently, the number of proton therapy centers has increased to over 89 therapy facilities worldwide. Proton therapy is beneficial because it can spare healthy tissues due to its unique physical properties, which lead to different dose distributions. Proton therapy can mitigate or prevent treatment side effects like a decline in IQ, reduced function and quality of life, and the risk of developing secondary cancer(s) from irradiation. Thus, this therapy is very suitable for complex cancers, especially childhood cancers. Given the accuracy of the proton beam range and treatment plan uncertainties, a large safety margin has been used in planning and delivery. The development of methods for range verification and the monitoring of dose delivery in real time would provide better control of beam direction and reduce currently used safety margins.

Several research groups are currently developing imaging systems for proton range monitoring based on two main imaging modalities: positron emission tomography (PET) and prompt gamma imaging (PGI). However, the challenges associated with monitoring the proton beam range are significant and complex, calling for the need to continue developing imaging systems.

One of the PGI imaging modalities is using a Compton imaging camera to image the prompt gamma rays emitted from irradiated tissue during therapy. Compton cameras utilize Compton kinematics to back trace the location of the gamma source. The typical configuration of a Compton camera comprises two positions and energy-sensitive detectors. The University of Liverpool have developed a gamma-ray imaging system (Gri+),which is a three-tier semiconductor Compton camera system ideally suited to imaging high $\gamma$-rays. This thesis aims to evaluate the performance of the Gri+ system by experimentally exploring its limitations and opportunities for PGI during proton radiotherapy. In addition, it proposes a sets of recommendations for the future measurements in a proton radiotherapy

facility.

The main research objective is to evaluate the Gri+ system in a setting that approximates the proton radiotherapy environment. To achieve this objective, the following methodology is proposed.

**First** Radioactive sources emitted high energy $\gamma$ rays in experiments at the University of Liverpool will be used to evaluate the following:

(a) The event sequence recorded in the system.

(b) The image resolution for high-energy $\gamma$-rays and for $\gamma$-rays which intent in complex paths.

(c) The suitability of the digital data acquisition (D-DAQ) system for processing data from higher energy $\gamma$-ray events and propose the recommended settings for imaging at high levels of gamma-ray energy.

**Second** a high-count-rate source will be used to evaluate the system's performance and to explore its count rate limitation.

**Third** a spectroscopy measurement will be conducted at the Clatterbridge Cancer Centre to explore the radiation present in the treatment room and determine the best detection position for the Gri+ system in future in-situ evaluations.

## 1.1   Thesis outline

**Chapter 2:** presents an overview of the proton beam therapy including gamma-ray emissions. In addition, a literature review is conducted to survey previous studies on PGI systems undertaken by different research groups.

**Chapter 3:** presents an overview of the fundamental physics related to radiation detection. This chapter discusses the gamma-ray interaction mechanisms and the operational characteristics of semiconductor detectors.

**Chapter 4:** describes the Gri+ system's component, as each part of the system plays a specific role in achieving gamma-ray imaging. In addition, it outlines the specifications for the detectors and data acquisition systems, as well as the software and methods used to achieve data sorting.

**Chapter 5:** examines the Gri+ system in a setting that approximates the Clatterbridge Cancer Centre's environment by evaluating the system's response to high energy gamma-rays. This is achieved by evaluating the energy deposited in the detectors and validating a calculation method to predict the

energy deposited in the detector during proton therapy, in addition to exploring the complexity of the event sequence, according to the number of interactions per gamma in each detector. This chapter studies the usefulness of Compton imaging resolution at high energy of gamma-ray and in relation to more complex event sequences than reported in previous studies. It also specifies the Gri+ system's setup and the most suitable setting for prompt gamma-ray imaging.

**Chapter 6:** evaluates the Gri+ system's performance in a high-count-rate scenario. This is because of the high level of radiation present in the proton therapy environment. In addition, the maximum count rate that the Gri+ system can process when it is set up for Compton imaging is determined. This is achieved by using a phantom filled with a high-activity radioactive solution. In addition, a detailed count rate investigation for the digital DAQ is conducted by comparing it to analogue pulse counting.

**Chapter 7:** discusses the findings regarding the radiation present in the proton therapy environment to inform how the Gri+ system can operate there in the future. This was achieved by evaluating spectrometry measurements conducted at the Clatterbridge Cancer Centre by the members of the nuclear physics group at the University of Liverpool prior to this thesis. This chapter reports the effect of using different targets, shield materials, and detection angles to determine the detection visibility of 4.44 MeV and 6.13 MeV gamma rays.

# Chapter 2

# Review of proton beam validation methods

The number of cancer treatment centres using proton beams is growing, as this technique provides advantages over conventional radiation therapy for some tumours. However, a developed method for verifying the beam range and the doses delivered during proton therapy is crucial. This chapter begins with a detailed introduction to proton beam therapy, including $\gamma$-ray emission during proton therapy. Finally, a literature review is provided to survey previous studies conducted by different research groups on prompt gamma imaging systems.

## 2.1   Introduction to Proton beam therapy

When treating cancers, rather than photons being utilised, proton beam therapy sees protons used during the patient's radiation therapy. Notably, the unique physical properties of protons lead to different dose distributions than when photons used. Figure 2.1 shows the relative dose deposited as function of depth in the tissue for protons and photons. The proton beam shows low dose in superficial depth, most of the dose is within the tumor volume and the area beyond tumor has negligible dose. However, the conventional x-ray photon radiotherapy beam deposits large dose in superficial depth and then falls off exponentially as tissue depth increases. In addition, a spread-out Bragg peak, which consists of multiple Bragg peaks of various energies is produced to extend an uniform dose covering the tumor area.
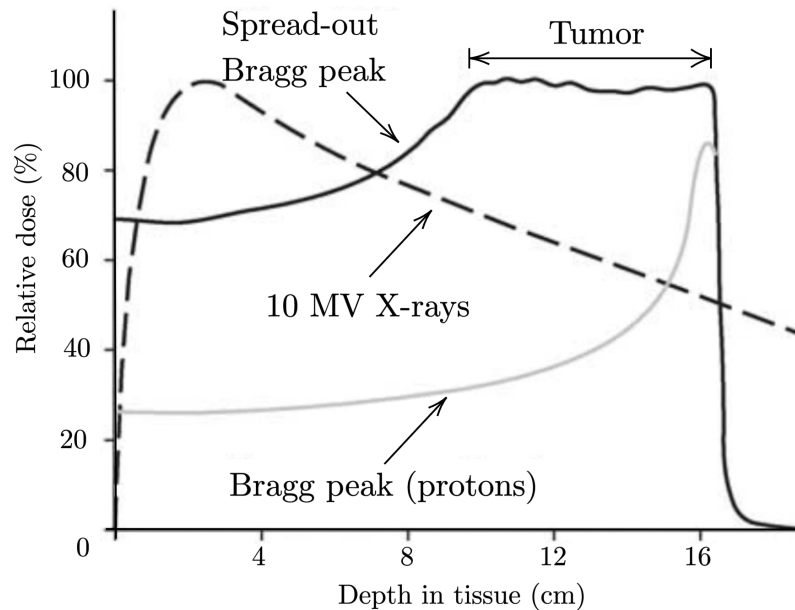
**Figure 2.1:** The relative dose deposited as function of depth in the tissue for a proton beam, a single Bragg peak (grey), a spread-out Bragg peak (black) and conventional x-ray photon radiotherapy beam (dashed). Adapted from [1].

Because the protons are heavy charged particles, they experience different interactions with matter than a photon. The main interactions are Inelastic Coulomb interaction with atomic electrons, Elastic Coulomb interaction with atomic nuclei, and Non-elastic nuclear interaction, Bremsstrahlung as shown in Figure 2.2. Bremsstrahlung is theoretically possible, but at therapeutic proton beam energies, this effect is negligible [2].

These interactions result in the proton energy loss is summarised as follows. **Inelastic Coulomb interaction with atomic electrons** result in the proton beam losing energy where the proton energy lost is inversely proportional to the square of the proton velocity due to an increase in the stopping power [3]. Thus, the proton energy (velocity) is much higher near the tissue surface and gets slow as the depth in the tissue increases until it stops completely. This result is most of the energy being deposited in the Bragg peak region, as shown in Figure 2.1. **Elastic Coulomb interaction with atomic nuclei** results in deflection of proton trajectory by repulsive Coulomb elastic scattering with a nucleus. The proton rest mass is 1832 times greater than an electron and for this reason, most protons travel in a nearly straight line. In contrast, the proton experiences a repulsive elastic Coulombic scattering when it passes close to the atomic nucleus with a large atomic mass, deflecting the proton from its original straight-line trajectory. **Non-elastic nuclear interaction** removes the primary proton and creates secondaries such as proton, electron, neutron and prompt gamma rays [2].
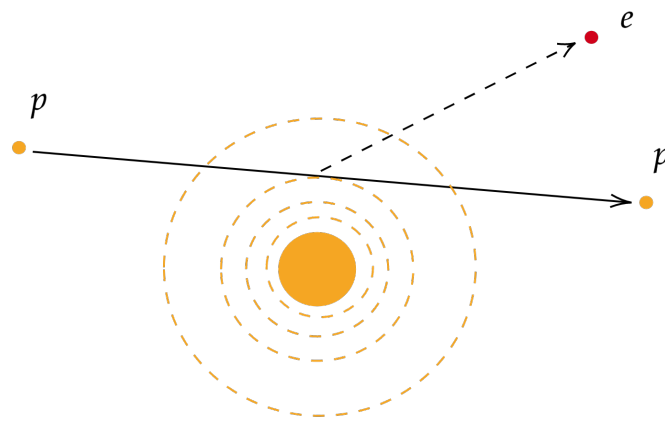
**(a)** Inelastic Coulombic
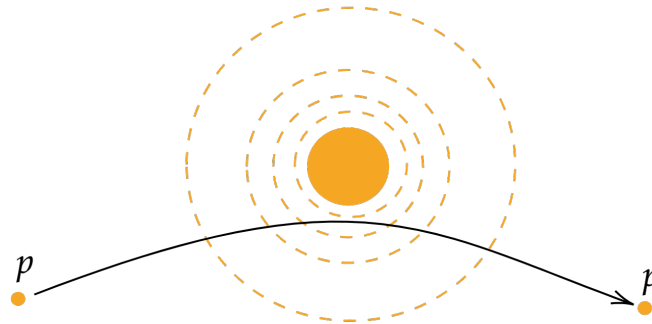


**(b)** Elastic Coulombic interactions
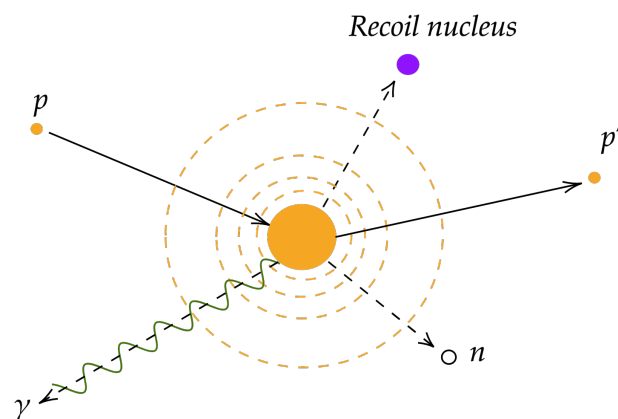


**(c)** Non-elastic nuclear interaction

**Figure 2.2:** Schematic of the proton interaction mechanism with matter (a) inelastic Coulombic interactions result in the energy loss, (b) elastic Coulombic interactions result in deflection of proton trajectory, and (c) non-elastic nuclear interaction result in remove the primary proton and creates secondaries such as proton, electron, neutron and prompt gamma rays. Reproduced from [2].

The advantages of proton therapy include decreased radiation doses to normal tissue and reduced late radiation toxicity, thereby making this therapy suitable for complex, especially childhood, cancers [4]. In order to avoid under or overdosing the tumour, the beam range needs to be well defined owing to the steep dose deposited at the Bragg peak's distal edge. Therefore, dose distribution monitoring is required to reduce the safety margins (uncertainty) and obtain better control of the beam's direction [5]. The safety margin considered in the proton therapy ranges from 2.4% to 6.3% of the beam energy + 1.2 mm to 3 mm [6], [7].
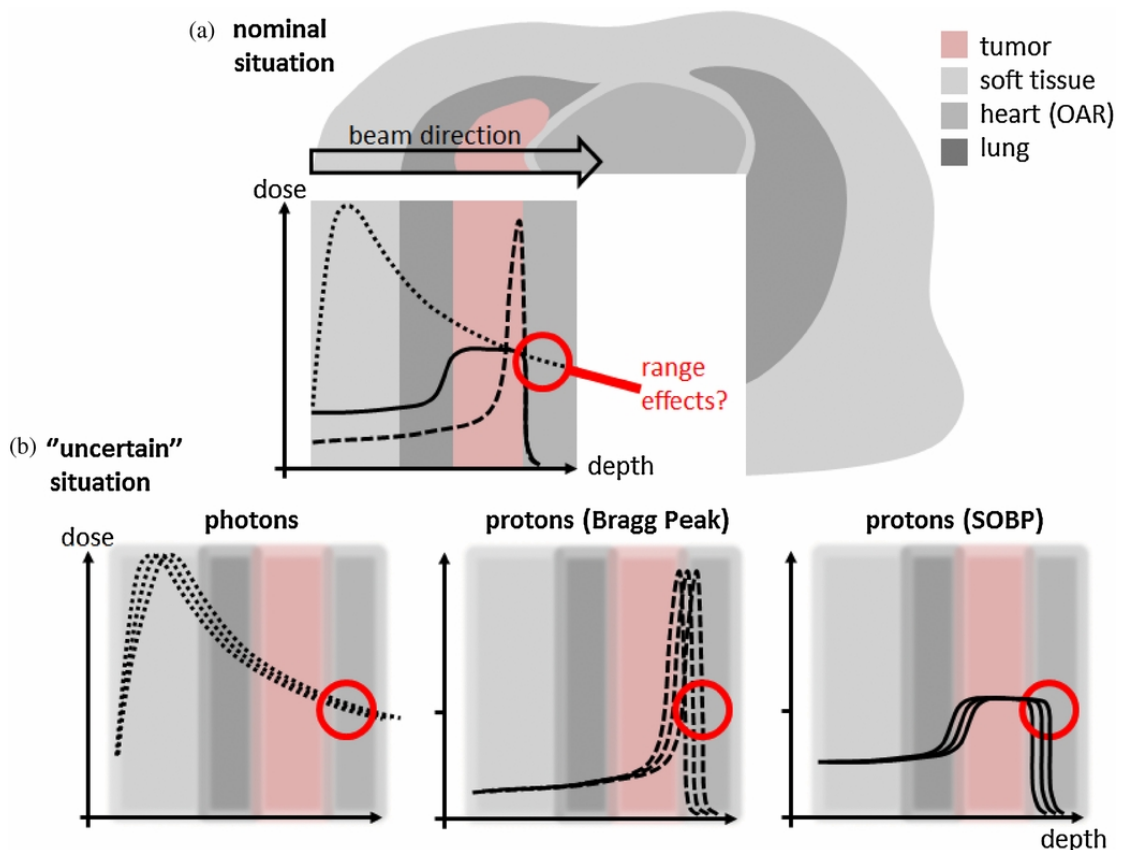


**Figure 2.3:** The dose deposited as a function of depth in the patient for proton beam, a single Bragg peak, a spread-out Bragg peak (SOBP) and conventional radiotherapy beam for (a) nominal situation where it is an ideal situation without uncertainty and (b) an uncertain situation. Red circles point to the area affected by the beam range's uncertainty. Reproduced from [5].

Figure 2.3 shows the dose deposited as a function of depth in the patient for, a single proton beam Bragg peak, a spread-out proton beam Bragg peak and conventional x-ray radiotherapy beam. It shows two situations: a nominal situation where it is an ideal situation without uncertainty and an uncertain situation where a red circle points to the uncertainty contributing to the delivered dose. It can be seen in Figure 2.3 (b) that the uncertainty in the proton beam introduced a

larger dose to the healthy tissue than the conventional x-ray radiotherapy beam. It is because, for conventional x-ray radiotherapy, there is a small change in dose at that tumour depth, so the uncertainty is also less, but the impact is large for the proton beam because of the very narrow Brage peak. It is believed that the source of uncertainty arises in the treatment planning process of proton therapy. Computer tomography (CT) images are the common approach to defining the proton beam range. The information of electron density distributions achieved from this CT image are used to calculate the relative proton stopping power [8]. The anatomical changes occurring between treatment plan and treatment delivery as well as the organ motion could emerge additional source of uncertainty [7].

## 2.2   Gamma ray emission during proton therapy

Proton-nucleus interactions produce two different forms of secondary photons during proton therapy. These are positron annihilation photons and characteristic prompt gammas (PG). Positron annihilation photons arise from short-lived, positron-emitting isotopes created by proton-nuclear interactions that produce two coincident annihilation photons of energy 511 keV. Positron emission tomography (PET) is used as indirect monitoring of the proton beam dose. However, PET scans are commonly conducted in a separate room, and owing to the lag time, the results of the scans can be affected by both the physical and biological washout phenomenon and decay half-lives related to PET activity. Therefore, this option is better used as a post-irradiation control rather than a real-time monitoring solution [9].

As a consequence of the deexcitation of tissue nuclei following non-elastic nuclear interaction, characteristic gamma rays are produced during proton irradiation. Using the prompt gamma (PG) rays is proposed as a noninvasive approach to verify the proton beam ranges [8]. This correlation occurs up to a few mm of the proton beam range, where the proton energy falls below the Coulomb barrier threshold [10]. In addition, a study revealed that the 6.13 MeV prompt gamma-ray from oxygen is directly proportional to the amount of oxygen in the sample [11]. However, the PG rays can only be correlated to but not directly match the delivered dose due to intrinsic physical differences between non-elastic nuclear and inelastic Coulomb interaction [7]. The spatial distribution of prompt gamma rays is highly correlated to the proton's range. Indeed, they can potentially be used to verify the proton dose [8].
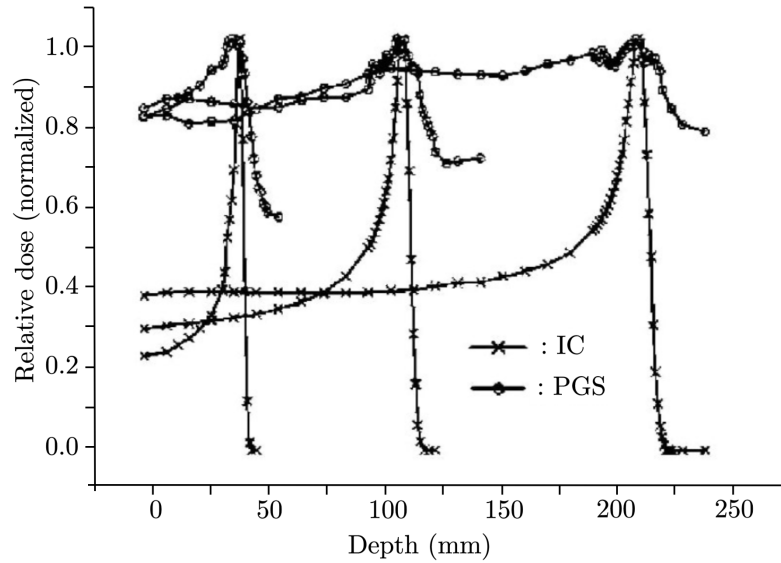
**Figure 2.4:** The depth-dose distributions at three different proton energies of 100, 150, and 200 MeV using an ionization chamber (IC) with the PGS measurements. Reproduced from [8].

The first experimental study that reported the actual dose distribution using the gamma measurements was repated in Ref [8]. The depth-dose distributions were measured by using a parallel-plate ionization chamber and the prompt gamma scanner (PGS). These measurements were at three different proton energies of 100, 150, and 200 MeV in a water phantom, as shown in Figure 2.4. The prompt gamma scanner PGS consists of a CsI(Tl) scintillator and three layers of shielding against neutrons generated from the phantom. Figure 2.4 shows a clear correlation between the peaks of prompt gamma distributions (summing the gammas of over 4 MeV) and the Bragg peaks of the dose distributions around 1-2 mm at 100 MeV; however, at higher proton beam energy, the detection system suffers from high neutron count rate as expected from a simulation study [8]. The same study reported the gamma ray count distributions as a function of depth with different energy thresholds. This energy threshold defines the minimum gamma energies used in the final gamma-ray count distributions. Using 4 MeV threshold showed a good correlation between the peaks of prompt gamma distributions and the Bragg peaks of the dose distributions within 1–2 mm at 100 MeV.

The main isotopes in human tissue are carbon and oxygen. Murphy et. al. [12] reported the main gamma line produced from inelastic reactions with carbon and oxygen, therefore they focused on the transitions that decay to the ground state with the largest cross sections at low proton beam energies. The main gamma lines from $^{12}$C are 4.44 and 15.1 MeV, and the cross sections for production of those gamma lines are shown in Figure 2.5a.
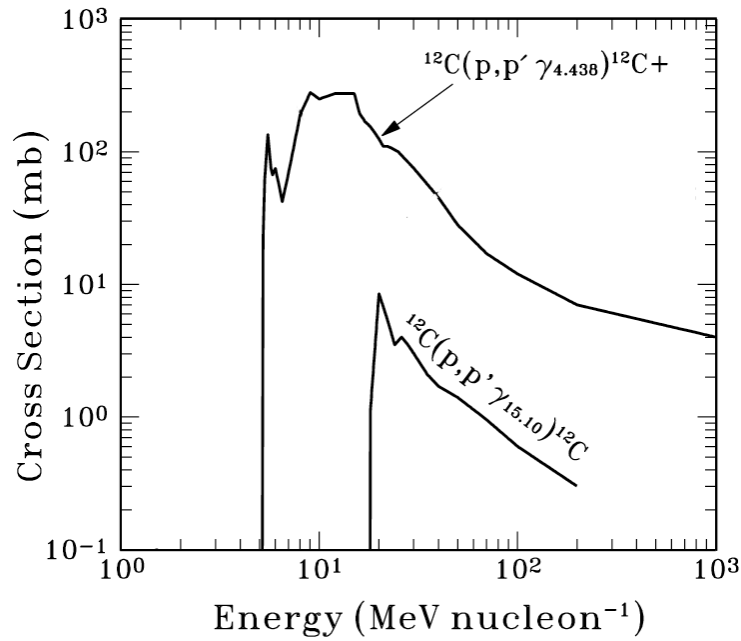
**(a)** The cross sections for production of 4.4 MeV and 15.1 MeV $\gamma$'s emitted from $^{12}$C.
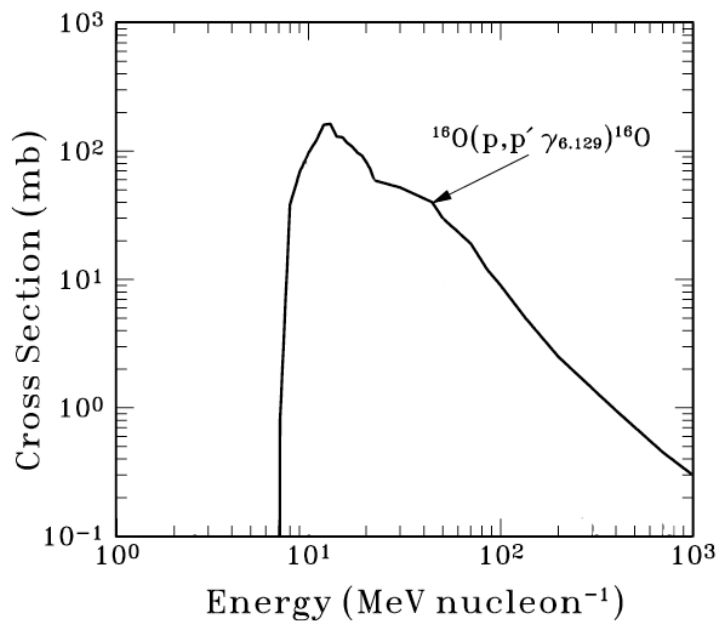


**(b)** The cross sections for production of 6.13 MeV $\gamma$'s emitted from $^{16}$O

**Figure 2.5:** The Cross sections for production from proton reaction with (a) 4.4 MeV and 15.1 MeV $\gamma$'s emitted from $^{12}$C; (b) 6.13 MeV $\gamma$'s emitted from $^{16}$O. Reproduced from [12].

It can be noticed that the 4.44 MeV has a large cross section compared to 15.1 MeV especially at low proton energy which makes it a promising candidate for proton beam validation. For oxygen, the main gamma lines from $^{16}$O are 6.13,

6.92 and 7.12 MeV. The 6.13 MeV gamma line has been used because it is the lowest gamma energy with high cross-section emitted from $^{16}$O, and also, this gamma line has been the subject of a large number of experimental studies.

Both the production gamma line cross sections, as shown in Figure 2.5, increased by a factor of about 2 near the end of the proton range. In addition to this study, several experimental and simulation studies reported that the cross-section of both the 4.4 MeV and 6.13 MeV gamma line are dependent on the proton beam energy [13][14].

Additionally, since these PGs are emitted non-isotopically, there is an angular presentation to the PGs' production cross-sections [15]. This is because the angular distribution of gamma emission depends on the proton energy and the nuclear levels structure [16]. The absolute cross sections measured by Kiener et al [16] used a set of eight HPGe detectors with BGO shielding for Compton suppression at six different angles. The proton beam energy was 14 MeV and the irradiated target was collodion foils with chemical composition $C_{12}H_{16}N_4O_{18}$. The angular distributions of 4.4 MeV and 6.13 MeV at a proton energy of 14 MeV shown in Figure 2.6. Understanding the angular distribution is important to optimise the in-situ position of a prompt gamma detection system.
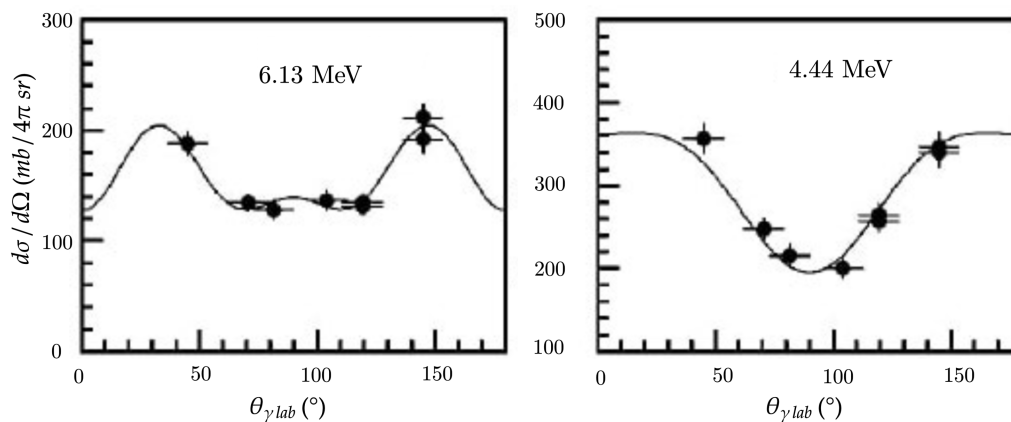


**Figure 2.6:** The angular distributions of 4.4 MeV and 6.13 MeV at a proton energy of 14 MeV. The vertical error and horizontal error bars are determined by the statistical error of the detector efficiency and the opening angle of the detectors respectively. The solid curves are Legendre polynom fits to the data. Reproduced from [16].

A considerable number of photons are emitted over 1 MeV, which on average has approximately 0.16 per proton at 160 MeV beam energy. The treatment dose is delivered as a fraction of 2 Gy, so the estimated number of gamma-rays is about $10^9$ gamma-ray emissions per second [17]. The advantages of using higher energy gammas include fewer scattering effects on their way out of the patient into the detectors which enhance the localisation regarding dose falloff. The ability to

perform real-time verification wherein prompt gammas can be detected instanta-neously, that is within a few nanoseconds, following nuclear interactions enables the monitoring of the treatment without additional doses being required.

## 2.3   Prompt gamma imaging systems for proton beam range verification

With many research methods adopted to realise clinical prototypes, numerous approaches to monitoring prompt gamma rays have been proposed and investigated. The various prompt gamma imaging systems can be categorised into those that use mechanical collimation, in which a physical collimator is used, such as tungsten and lead, and those that use electronic (Compton camera) collimation. The radiation detection methods will be describe in detail in Chapter 3.

### 2.3.1   Mechanical collimation systems

This system is similar to the gamma camera concept used in nuclear medicine but with a thicker collimator. The system consists of a scintillation detection system in conjunction with a thick collimator made of high-density material (i.e. tungsten or lead). The collimation should be thick enough to attenuate the high energy gamma-ray. The collimation perforation pattern should be well designed to project the distribution of the prompt gamma emitted during irradiation of the patient by the proton beam onto the scintillation detector.

The first feasibility study of a collimated single detector was undertaken by Min et al. [8]. There is a huge challenge facing the mechanical collimation systems because stopping high energy gamma rays in a collimator is difficult. A sufficiently thick collimator is required to stop the high energy gammas that scatter through the collimator, resulting in degraded signal to noise. In addition, designing mechanical collimation that allows detection of sufficient gamma-rays for good image quality is challenging. Since the feasibility study, many studies have tried to overcome the limitations associated with mechanical collimation. Some incremental changes include changing the collimation design and using different detector types and increasing the number of detectors where most prototypes report a limited field of view. The mechanical collimation system is still limited to provide the longitudinal prompt gamma rays distribution profile (1D information). Some of those researchers have been able to conduct the first clinical trials. However, the trade-off between camera detection efficiency and spatial resolution are challenging particularly for prompt $\gamma$ energies.

The most promising prototype was developed by [18]–[20]. This prototype

consists of a knife-edge shaped slit collimator in conjunction with scintillation detectors of 40 LYSO slabs mounted on a trolley for flexible positioning and alignment. It was the first prototype that reached clinical trials stage with encouraging results. The inter-fractional range variations were in the range of $\pm$ 2 mm for all evaluated fractions. The key literature material for the mechanical collimation systems is highlighted in Table 2.1.

**Table 2.1:** The key literature material for the mechanical collimation systems highlighted the detector type, the collimator type, experiment setup and reported results.

| Author | Detector type | Collimation type | Reported result | Study |
|---|---|---|---|---|
| [8] | CsI(Tl) scintillator 15x30x40 mm$^3$ | Collimation hole | First experimental study shows correlation between the gamma distributions and the distal falloff region of the proton beam. | Experimental study at 100,150 and 200 MeV |
| [21] | CsI(Tl) scintillator 15x30x40 mm$^3$ | Collimation hole | Simulation and experimental result shows the location of the distal dose edge can be determined within 1-2 mm from the distribution of the prompt gammas. Only the longitudinal prompt gamma rays distribution profile was reported and low proton beam energy was used. | Experimental study at 38 MeV |
| [22] | CsI(Tl) scintillator 50x30x3 mm$^3$ | Multislit | The result shows the location of the distal dose edge can be determined within 4 mm from the distribution of the prompt gammas. Only the longitudinal prompt gamma rays distribution profile was reported | Experimental study and simulation at 80, 150 and 220 MeV |
| [23] | Bismuth germanium oxide (BGO) scintillator 50x100x250 mm$^3$ | Multislit | This study proposes two collimation designs. The precision of bragg peak position intrinsically depends on statistics of incoming protons. The trade-off between camera detection efficiency and spatial resolution was reported. This system has a limited field of view. | Simulation study at 160 MeV |

**Table 2.1 continued from previous page**

| Author | Detector type | Reported result | Collimation type | Study |
|---|---|---|---|---|
| [24] | CsI(Tl) scintillator 15x30x40 mm$^3$ | Experimental results claim that the gamma distribution was sensitive to variations in the proton beam range of the order of 1 mm in water. Only the longitudinal prompt gamma rays distribution profile was reported. | Knife-edge | Experimental and simulation study at 50 MeV |
| [25] | Five square-shaped silicon drift detectors (SDD) of 1 cm$^2$ | This study establishes the feasibility of proton beam range measurements with millimetre accuracy in a homogeneous PMMA target. The possibility of achieving a 1–2 mm standard deviation on range estimation for low doses was reported. Limited FOV and count rate up to 5000 counts. | Knife-edge | Experimental and simulation study at 100 and 160 MeV |
| [26] | LYSO scintillator detector | The sensitivity needs to improve over small size prototype by one magnitude to achieve precision of 2 and 1 mm for the entrance rise and fall-off positions respectively and a precision for the total range of 2.2 mm was reported. The system need to be adjusted to align with the Bragg peak during the treatment. Low efficiency and limited FOV. | Knife-edge | Experimental study at 160 MeV |

**Table 2.1 continued from previous page**

| Author | Detector type | Collimation type | Reported result | Study |
|---|---|---|---|---|
| [18]–[20] | Scintillation detector two rows of 20 LYSO slabs | Knife-edge | A precision (2 sigma) in shift retrieval of 4 mm was reached with different delivered dose and different proton energy. Better precision in detecting the fall-off than the entrance point. The shifts in the proton range on the order 2–5 mm can be visualized for passive beam. Low efficiency was observed and the detection precision strongly depends on the target composition. Limited sensitivity to detect the range shift of the proton therapy at low statistics. **A clinical trial** was conducted by [20] in the head and neck tumor treatment. The inter-fractional global range variations were in the range of ± 2 mm for all evaluated fractions. Need to have background subtraction to improve the signal to noise ratio. The current trolley setup is limited to specific target sites and beam directions due to geometrical limitation. | Experimental study at 100, 110, 160 and 230 MeV |

## 2.3.2   Electronic collimation systems

There is a higher detection efficiency, electronic collimation system that use Compton cameras. These are to overcome the aforementioned limitations by removing the standard collimator in order to increase quantity of data. The dominant interaction mechanism of the prompt gammas (several MeV) will be the Compton scattering interaction, which is more suitable for the Compton cameras operation than for collimated systems. The concept of the Compton camera for gamma imaging is its use of Compton kinematics to reconstruct the incident gamma-ray path. The configuration of a typical Compton camera comprises two position and energy-sensitive detectors. In the first detector, the gamma-ray ideally undergoes Compton scattering at the angle ($\theta$) and deposits part of its initial energy ($E_1$). In the second detector, the gamma-ray ideally undergoes photoelectric absorption and deposits the rest of its energy ($E_2$), as depicted in Figure 2.7. Therefore, the first detector is named the 'scatterer' detector and the second the 'absorber' detector. The geometry and material of these detectors needs to be selected in order to achieve the best performance as part of the Compton camera system for a specified gamma energy range.
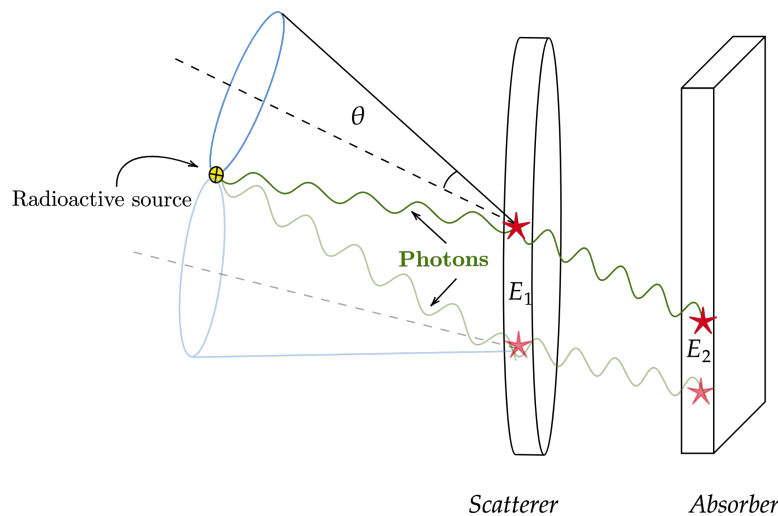


**Figure 2.7:** Schematic diagram of a semiconductor Compton camera.

The Compton image is created by producing a cone that can reflect the active source position, for which the cone apex angle and cone axis must be known. The cone apex angle is equivalent to twice the scattering angle $\theta$ for the $\gamma$-ray undergoing Compton scattering. By assuming that the gamma-ray scattered only once in the scatterer detector and was completely absorbed in the absorber detector, then the interaction with both detectors results in the deposition of all the initial gamma-ray's energy ($E_1$+$E_2$), which can be used to calculate the Compton

scattering angle $\theta$ [27]. The Compton scattering formula has been rearranged to calculate the Compton scattering angle $\theta$:

$$cos\left(\theta\right) = 1 + mc^2\left(\frac{1}{E_1 + E_2} - \frac{1}{E_2}\right) \qquad (2.1)$$

where $mc^2$ is the electron rest mass. From this equation, the cone apex angle is known. The cone axis can be drawn from a vector drawn between the position of interaction in both detectors. Now, the cone has been drawn where a point on the surface of this cone is the position at which the active source is located; indeed, it is necessary to produce more cones from other $\gamma$-rays emitted by the same source to determine the exact source location on the cone surface by overlapping the produced cones, as shown in Figure 2.8.
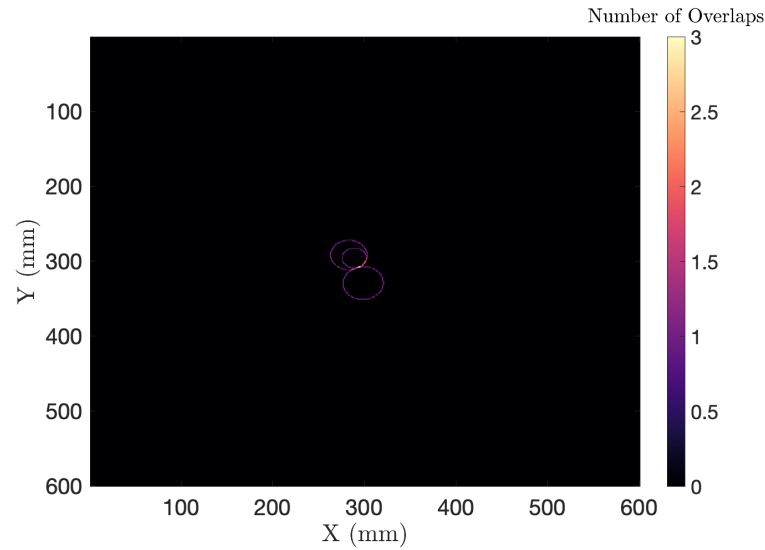
**(a)** Three events used to produce the image.
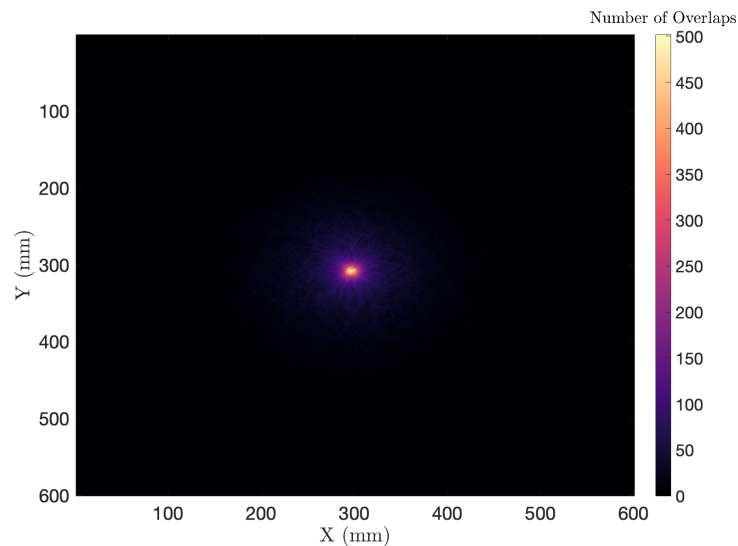


**(b)** 4000 events used to produce the image.

**Figure 2.8:** Example of Compton images produced from three events and 4000 events.

The first researcher to propose using Compton cameras for medical imaging was Everett et al. [28]. Various prototype detectors have been considered in PG imaging systems, including scintillators (LaBr$_3$ and BGO), semiconductors (Si and CZT), and a combination of scintillator and semiconductor detectors. Several research groups report encouraging preliminary results, and some of them manage to test the system in a clinical proton beam. However, the challenge remains to achieve sufficient statistics and imaging accuracy to determine the range of the proton beam in clinical routine. In the routine clinical treatment, about $10^8$ protons were produced in single PBS spots, which were delivered in less than 10 milliseconds. The production rate of PG per proton is about 0.1, which

produces about $10^9$ gamma-rays per second [29]. This amount of the gamma-ray rate, in addition to the secondary neutron production, in a short time will cause a huge load in the detection system. Compton cameras revealed the potential capability of providing better spatial resolution. They are capable of 3D imaging in comparison with collimated systems (1D profile). The development of Compton cameras has required several different concepts and approaches to overcome the detection efficiency limitation and handle the high count rate. In addition, a dedicated real-time 3D image reconstruction code is needed. There is a demand to continue the development process to overcome the current challenges of Compton imaging systems.

The most promising result was reported by [30]–[32]. This group's research uses a semiconductor Compton camera consisting of pixelated CZT detectors, using a new method to enhance the spatial resolution, such as the distance of the closest approach and the Compton line filter. The 2D images of the BP range were detectable with shift, and for 1D profiles, the detection of 3 mm shifts of the fall-off position was reported. However, this prototype has limited count statistics, and the authors suggest increasing the detector size to overcome this limitation. However, this will significantly increase the cost of system, as it is not possible to manufacture large blocks of CZD with sufficient spectroscopic performance. The key literature material for the mechanical collimation systems is highlighted in Table 2.2.

**Table 2.2:** The key literature material for the electronic collimation systems highlighted the detector type, experiment setup and reported results.

| Author | Detectors type | Reported result | Study |
|---|---|---|---|
| [33]–[35] | The monolithic lanthanum bromide (LaBr$_3$) crystals of 16 × 18 × 5 mm and silicon photomultipliers elements of 3 × 3 mm | This prototype allows for two and three layers and has simulation tested with energy between 2 and 7 MeV from point-like sources and were reconstructed with 3–5 mm resolution. It experimental tested at a 150-MeV proton beam. A 7 mm is reported shift in the Bragg peak location from the reconstructed profiles. This prototype shows about 10% deviation from linearity at 3.44 MeV. In addition, poor time resolution (25 ns FWHM in coincidence mode) and limited count statistics were reported. Another limitation was reported that there is a lack of dedicated image reconstruction code to include more complex events and reconstruct the image online. | Simulation (2-7 MeV) and experimental at 150 MeV proton beam. |
| [36], [37] | Sensitive scintillator array and multi-pixel photon counter arrays with a dimension of 14× 15× 16 cm (2.5 kg) | This prototype evaluates the differences between the gamma peak positions and the Bragg peak position calculated by simulation and experiment. For this evaluation, two low gamma energy of 511 keV and 718 keV were used. From the simulation result, the differences between the gamma peak positions and the Bragg peak position using 511 keV and 718 keV were calculated as 7 mm ± 2 mm and 3 mm ± 8 mm, respectively. However, experimentally this prototype could not report a clear conclusion about the correlation between the prompt gamma rays and the Bragg peak position. | Simulation and experimental at 70 MeV proton beam |

**Table 2.2 continued from previous page**

| Author | Detectors type | Reported result | Study |
|--------|----------------|-----------------|-------|
| [38], [39] | Double-sided silicon strip detectors (DSSDs) as scatterers and scintillation BGO detectors as absorbers | This prototype result reported only by simulation study. Using 160 MeV proton beam, the precision is reported to be about 2.6 mm with an LM-MLEM reconstruction code. However, limited statistics was reported, and the system cannot retrieve the PG profile fall-off with high intensity proton beam, due to the contamination of background events | Simulation at 160 MeV proton beam. |
| [40], [41] | CZT detector and three BGO crystals | The system was tested with monoenergetic 4.44 MeV photons. The findings demonstrated a relative energy resolution of 3.5% (FWHM) at 511 keV for the CZT detector, and an energy resolution of 10% at 4.44 MeV (Proton capture of $^{15}$N ) for the BGO detector. There is no report for the whole system image resolution. The limited detection efficiency for this prototype was reported. | Experimental at monoenergetic 4.44 MeV photons |

**Table 2.2 continued from previous page**

| Author | Detectors type | Reported result | Study |
|---|---|---|---|
| [42], [43] | A beryllium plate of 1 mm thickness as the electron converter. Two layers of DSSD (Silicon) of 50 × 50 mm² with thicknesses of 150 and 300 $\mu m$ as electron tracking hodoscopes. A plastic scintillation detector of 100 ×100 ×20 mm³ serving as a calorimeter. | This prototype used a different method called gamma electron vertex imaging (GEVI). The purpose of GEVI is to track the electrons produced from converting the prompt gammas into electrons. The GEVI system imaging capability was tested by imaging a $^{90}$Sr beta source with maximum energy of 546 keV and 2284 keV, a $^{60}$Co gamma source and a 45 MeV proton beam in a PMMA phantom. The system demonstrated its ability to image the vertices of prompt gammas without reporting the whole system image resolution. However, the system suffers from long system dead-time and low image sensitivity by about 100 times lower than the expected value obtained by simulation. | Simulation and experimental using $^{90}$Sr beta source (546 keV and 2284 keV), a $^{60}$Co gamma source and a 45 MeV proton beam |

**Table 2.2 continued from previous page**

| Author | Detectors type | Reported result | Study |
|--------|----------------|-----------------|-------|
| [30]–[32] | A $2 \times 2$ array of pixelated CZT detectors ($2 \times 2 \times 1.5$cm each) | This prototype was built and evaluated at 662 keV, where the energy resolution was 9.7 keV (FWHM). The raw absolute efficiencies were measured using a $^{60}$Co and were $2.2 \times 10^{-5}$ and $5.8 \times 10^{-7}$ for double and triple scatter events, respectively. Spatial resolution has been enhanced by the adoption of new methods such as the distance of closest approach and the Compton line filter. These filters work to remove undesirable interactions from data samples. This prototype was tested with clinical proton beams of 114 and 150 MeV by irradiating a water target. The 2D images of the BP range were detectable with shift, and for 1D profiles, the detection of 3 mm shifts of the fall-off position. This prototype has limited count statistics. | Experimental at 114 and 150 MeV proton beam. |

# Chapter 3

# Fundamentals principles of the Gri+ Compton camera

The Gri+ Compton camera system produces images of gamma-ray sources based on the interaction and detection of gamma-rays within semiconductor detectors. To investigate and optimise the Gri+ performance, it is essential to understand the gamma-ray interaction mechanisms and properties of the detection materials. This chapter will outline the concepts of how gamma-rays interact in matter and the characteristics of semiconductor detectors.

## 3.1 Interaction of Gamma Rays with Matter

Gamma-rays have different mechanisms of interaction with matter, depending on the gamma energy and the absorber atomic number (Z). There are three dominant mechanisms within the energy range of interest in this thesis, 1 keV to 6.2 MeV: photoelectric absorption (pa), Compton scattering (cs) and pair production (pp) [44]. The summation of the linear attenuation coefficient for these three mechanisms contributes to the total linear attenuation coefficient $\mu_t$ and can be determined by:

$$\mu_t = \mu_{pa} + \mu_{cs} + \mu_{pp} \qquad (3.1)$$

where $\mu_{pa}$, $\mu_{cs}$ and $\mu_{pp}$ are the probability that a gamma-ray is removed per unit length by photoelectric absorption, Compton scattering and pair production interaction mechanism, respectively. Figure 3.1 shows the relative probabilities of Compton scattering, photoelectric absorption and pair production as a function of Z for the detection material and incident gamma-ray energy. It also highlights the atomic numbers of the two detecting materials used in this study, Z= 14 for silicon used as the scatterer detector where the Compton scattering probability is dominant at gamma ray energy about 0.05 MeV to 15 MeV, and Z= 32 for

the germanium used as the first absorber detector where the Compton scattering probability is dominant at gamma ray energy about 0.2 MeV to 6 MeV. For the gamma-ray energies range investigated in this thesis, such as 1.8 MeV, 4.4 MeV and 6.1 MeV, it shown that the gamma ray is more likely to experience Compton scattering in both detectors rather than experience Compton scattering in the scatterer detector then photoelectric absorption in the first absorber detector. Using a Compton camera at higher gamma energy needs to use an extra absorber detector, which will be explained in Chapter 4. Gamma-rays will either be scattered or absorbed through these interaction processes, which is shown to have an exponential dependence on the linear attenuation coefficient. The intensity (I) of a collimated monoenergetic gamma-ray beam after travelling a distance (z) through an absorbing medium can be related to the linear attenuation coefficient by:

$$I = I_0 e^{-\mu_t z} \tag{3.2}$$

where $I_0$ is the intensity of the gamma-ray beam before it enters the absorbing material.
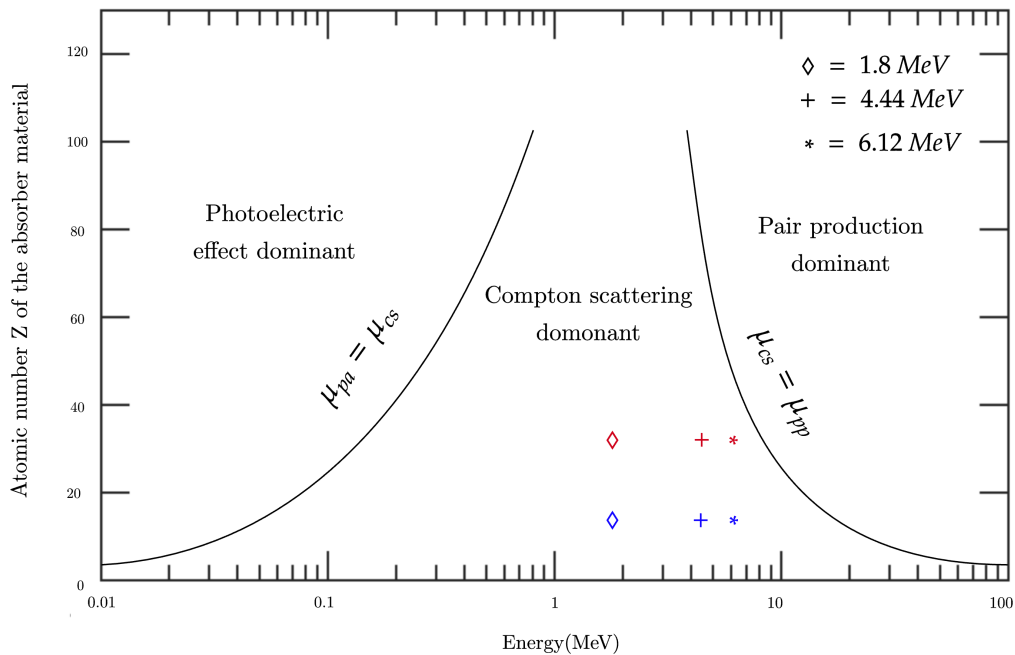


**Figure 3.1:** The relative probabilities of $\mu_{pa}$, $\mu_{cs}$ and $\mu_{pp}$ as a function of Z for the detection material. The energy labels are shown for germanium (Ge) (red) and silicon (Si) (blue). Image reproduced from [44]

.

### 3.1.1  Photoelectric Absorption

In the photoelectric absorption process, the gamma-ray is entirely absorbed by a bound atomic electron, transferring all the gamma-ray energy to that electron. A photoelectric is then ejected from the absorber atom, leaving a vacancy in one of its bound shells which is filled by the rearrangement of higher-state orbital electrons or free electrons. Therefore, a characteristic x-ray is released as shown in Figure 3.2, which is usually reabsorbed close to the interaction site. Escape of the x-ray from radiation detectors may occur if the interaction site is close to the surface of the absorbing material. The photoelectron energy ($E_e$) depends on the energy of the incident gamma-ray ($E_\gamma$) and the binding energy of the electron ($E_b$) of its original shell. It can be calculated using the following equation:

$$E_e = E_\gamma - E_b \tag{3.3}$$

Photoelectric absorption is the dominant interaction mechanism for low-energy gamma rays incident on materials with a high atomic number (Z), as shown in Figure 3.1. The probability that such an interaction will occur is given by:

$$\sigma PA \propto \frac{Z^n}{E_\gamma^{3.5}} \tag{3.4}$$

where n is a number between 4 and 5 dependent on the gamma-ray energy (E) [44].
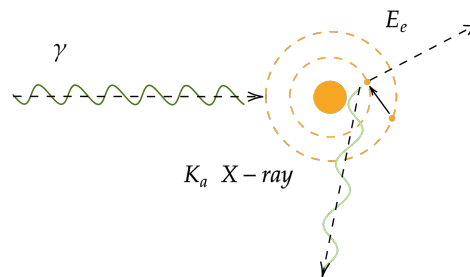


**Figure 3.2:** Schematic of the photoelectric absorption mechanism and the emission characteristic X-ray.

### 3.1.2  Compton Scattering

Compton scattering interactions in radiation detectors are essential in the operation of a Compton camera. The Compton scattering process involves the interac-

tion of a gamma-ray with an outer shell electron in the absorbing material. The gamma-ray is deflected by a scattered angle from its original path and transfers part of its energy to the electron, which is assumed to be initially at rest, as shown in Figure 3.3. The scattering angle $\theta$ can range from 0° to 180° and is related to the energy transferred to the recoil electron due to the conservation of energy and momentum [44]. The scattered photon energy ($E'_\gamma$) is given by the following equation:

$$E'_\gamma = \frac{E_\gamma}{1 + \frac{E_\gamma}{mc^2}(1 - cos\theta)} \tag{3.5}$$

where the rest mass energy of the electron (0.511 MeV) is mc$^2$.
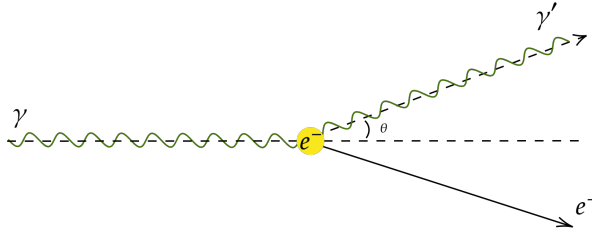


**Figure 3.3:** Schematic diagram of Compton scattering.

The Compton scattering probability depends on the number of electrons available as scattering targets and thus increases linearly with the number of protons (Z). The angular distribution of scattered gamma rays can be estimated by using the Klein-Nishina formula for the differential scattering cross-section ($\frac{d\sigma}{d\Omega}$) as:

$$\frac{d\sigma}{d\Omega} = Zr_2^0\left(\frac{1}{1 + \alpha(1 - cos\theta)}\right)^2\left(\frac{1 + cos^2\theta}{2}\right)\left(1 + \frac{\alpha^2(1 - cos\theta)^2}{(1 + cos^2\theta)[1 + \alpha(1 - cos^2\theta)]}\right) \tag{3.6}$$

where $\alpha$ is equal to $E_\gamma/mc^2$ and $r_0$ is the electron radius. Figure 3.4 shows the angular distribution of scattered gamma rays for selected gamma-ray energies that are relevant to this thesis such as 0.141, 1.836, 4.44 and 6.12 MeV. It can be seen that higher gamma rays such as, 1.836, 4.44 and 6.12 MeV are preferentially forward focused, whereas at low energies such 0.141 MeV, the distribution becomes nearly symmetrical about the 90° axis with more backward scattering.
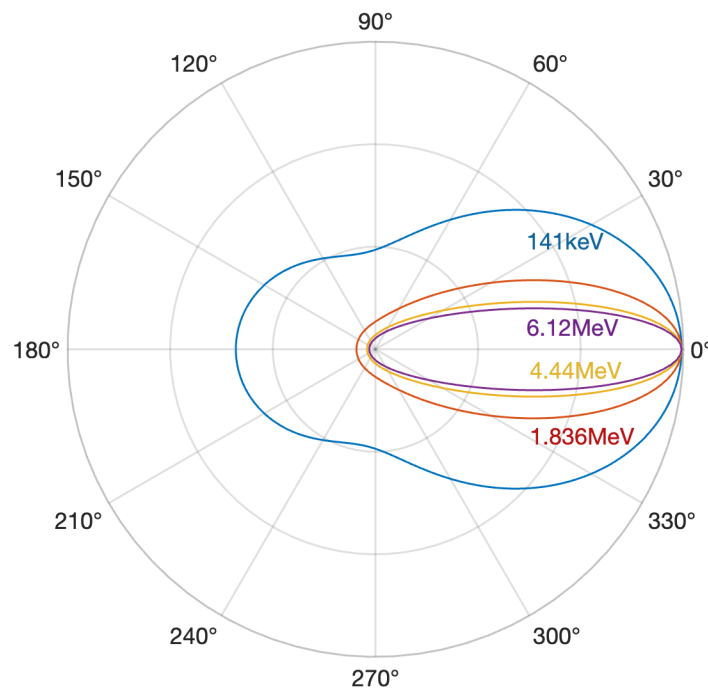
**Figure 3.4:** Angular distribution of scattered gamma rays of 0.141, 1.836, 4.44 and 6.12 MeV using the Klein-Nishina formula for the first absorber detector Z=32.

### 3.1.3   Pair Production

The pair production process can occur when the gamma-ray energy is more than twice the rest mass energy of the electron (1.02 MeV) and becomes the dominant interaction process when the gamma-ray energy reaches several MeV. It is therefore important to consider in this thesis since the prompt gamma emissions during proton beam radiotherapy are expected to be 4.4 MeV and 6.1 MeV. In the pair production process, the gamma-ray disappears in the Coulomb field of the nucleus and is replaced by an electron-positron pair. Creating this pair requires the total rest mass energy of the particle pair, 0.511 MeV + 0.511 MeV, while any additional energy transferred by the initial gamma-ray is shared between the positron and the electron as kinetic energy. Two 0.511 MeV annihilation photons, 180° from each other, are emitted as secondary products of the interaction because the positron annihilates after slowing down in the medium as shown in Figure 3.5. If the photons are absorbed in the same material, all energy remains in the system as full peak features in gamma-ray spectra. However, if one or both of these gamma rays escape the material, escape peak features in gamma-ray spectra are present as a single or double escape peak [44], at energies corresponding to initial gamma energy minus 0.511 MeV and initial gamma energy minus 1.022 MeV, respectively.

These escape peaks add complexity to the gamma-ray spectrum if there are several high energy gamma-ray emitters.
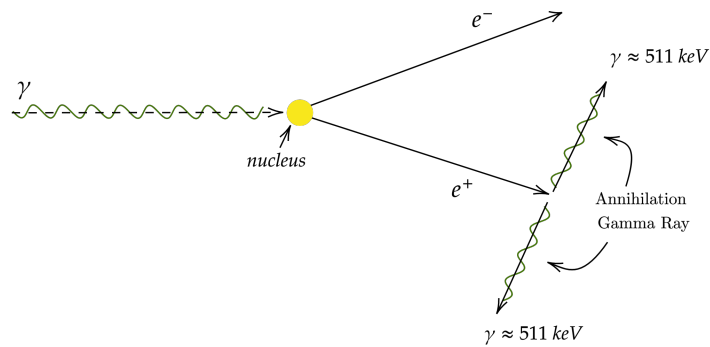


**Figure 3.5:** Schematic diagrams showing pair production with secondary annihilation gamma rays.

## 3.2   Gamma-Ray Detectors

Scintillator and semiconductor detectors have been used in gamma-ray detection since the mid-20$^{th}$ century. Detector performance characteristics, including operating environment, energy resolution and efficiency, are the primary considerations for any gamma-ray detection application. For some end uses, other characteristics such as time resolution and position resolution become important too. Semiconductor detectors have better energy resolution than scintillator detectors but are typically less efficient and with poorer time resolution. This thesis uses semiconductor detectors as the primary focus because the Gri+ uses three semiconductor detectors. The following section will explore the properties and detection operation of semiconductors in more detail.

### 3.2.1   Semiconductor detectors

Semiconductor detectors have been used since the early 1960s in many nuclear physics experiments where energy resolution is essential. In routine use, these detectors achieve the best energy resolution from radiation spectroscopy. Using a semiconductor detector in imaging the prompt gamma emitted during proton beam therapy will be a challenge because of the extreme radiation environments (such as high neutron flux) and the prompt gamma-rays have high energies. Imaging high gamma-ray energy needs a detector with adequate thickness to attenuate these gammas and eventually fully absorb them whilst having an imaging system with a clinically acceptable size. Despite being relatively high radiation-induced

damage sensitivity, semiconductor detectors have several other desirable features in addition to superior energy resolution. These features include compact size and an adequate thickness that can be varied to meet the requirements of many applications. Silicon and germanium are commonly used semiconductor detectors; while using high-purity silicon can limit the depletion region depth to 1-2 mm, high purity germanium (HPGe) can offer depletion depths of several centimetres. Meanwhile, fabricating the silicon using a lithium drifting process can extend the depletion region depth to 5-10 mm. Silicon detectors are mainly used for charged-particle spectroscopy but can detect very low-energy gamma rays up to 50 keV or X-rays because of the high probability of photoelectric absorption as shown in Figure 3.1. In contrast, germanium is more widely used for gamma-ray measurements [44]. The advantage of superior energy resolution and compact size can be justified by explaining the properties of semiconductor material. Semiconductor material is high density material, so the size of semiconductor detectors that are used to measure a high-energy gamma-ray can be small [44]. The fundamental detection operation in semiconductor detectors relies on the creation of charge carriers (electron-hole pairs) as the incident radiation (gamma-ray) interacts in the detector. In an applied electric field, the motion of the electron-hole pair generates an electrical signal from the detector [45]. The following sections explain the fundamental principles of semiconductor materials and how they can be used as radiation detectors.

**Band Structure**

The crystalline periodic lattice of germanium and silicon builds band structure, which defines the allowed energy range for the electrons within these materials. The valence band is the lower band which consists of outer-shell electrons, while the conduction band is the upper band, where the electrons are free to move throughout the crystal lattice. The bandgap lies in between those two bands where the electron needs to cross the bandgap to reach the conduction band; the bandgap size defines the solid material conductivity into an insulator or a semiconductor as shown in Figure 3.6. The bandgap size for the insulator material is greater than 5 eV, which is hard to overcome by the electron. However, the semiconductor bandgap size is about 1 eV, for which thermal excitations are sufficient to allow valence electrons to move to the conduction band. This movement of electrons results in a deficiency of electrons in the valence band called a hole. This deficiency of electrons in the valence band may be filled by one of the neighbouring electrons and move through the valence band [46].
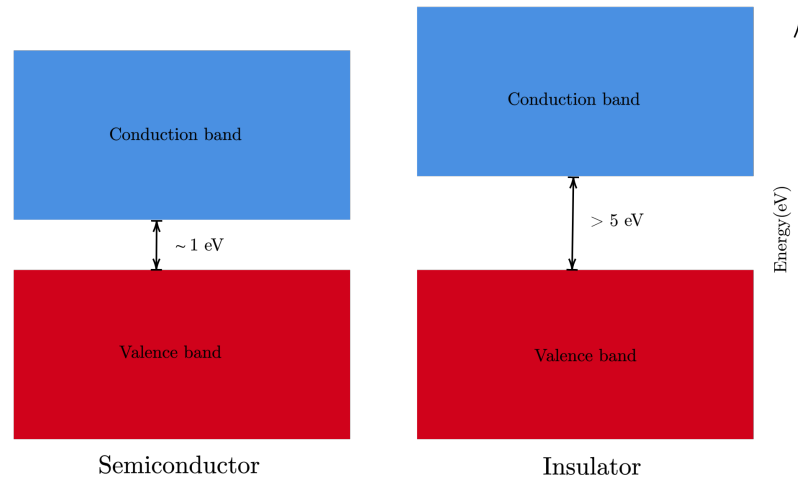
**Figure 3.6:** Schematic diagram of the band structure in a semiconductor and insulator.

**Charge Carriers**

When valence electrons move to the conduction band, this results in a deficiency of electrons, or 'holes' in the valence band. The electron is free to move rapidly through the semiconductor, but the hole is free to migrate through the valence band. Both electron (negative) and hole (positive) charge carriers are only moved in the opposite path under the influence of an applied electric field and contribute to the total electric current [47]. The charge carriers experience different generation and transport mechanisms before being either collected at an electrode or recombination. Charge carriers can be generated by different mechanisms, including thermal agitation and ionization by incident radiation, which supplies the carriers with necessary energy. Thermal generation of charge carriers can occur in some semiconductor materials at room temperature. In this mechanism, the thermal energy can be sufficient for the valence electron to overcome the bandgap and reach the conduction band, so semiconductor radiation detectors operate in low temperatures to avoid the thermal noise superimposed onto the signal. Charge carriers can be generated by receiving sufficient energy from ionising radiation to excite the valence electron and pass the bandgap to the conduction band [44]. In the semiconductor detector, when an incident gamma-ray transfers its energy to an atomic electron, a large number of excitations and ionisations take place as the electron comes to rest. This occurs over a small volume in the detector called the charge cloud. The number of electron-hole pairs (N) that are created in the semiconductor detector can be estimated from the energy of the incident gamma-ray ($E_\gamma$) and the average energy necessary to create an electron-hole pair

($E_{pair}$) of the absorbing material:

$$N = \frac{E_\gamma}{E_{pair}}$$

(3.7)

Charge carriers can be transported by two mechanisms, drift and diffusion. In the electric field's absence, the average charge carrier's movement will be zero because of random motion. However, when an external electric field is applied, charge carrier drift can occur and the charge carriers will move parallel to the direction of this field. At low electric field strength, the drift velocity shows a proportional relation to the strength of the applied electric field. However, at a higher electric field, the drift velocity slowly increases with the increased electric field until it reaches saturation velocity when the velocity becomes independent of any increases in the electric field [44]. The drift velocity of the charge carriers can be defined by:

$$\nu_h = \mu_h E$$

(3.8)

$$\nu_e = \mu_e E$$

(3.9)

where $\mu_e$ is the mobility of electrons, $\mu_h$ the mobility of holes and E is the electric field strength. In addition to the drift, diffusion of the charge carrier can occur as a result of inhomogeneous distribution of charge carriers and doping concentration in a semiconductor material. In the absence of an electric field, the average movement of a charge carrier is zero and there is a high probability that charge carriers will move from the high concentration side to the low concentration side [44]. The diffusion of the charge carriers can affect the arrival position, which leads to a limitation regarding the precision of the position measurements [47]. This effect can be characterised as a Gaussian distribution and calculated by:

$$\sigma = \sqrt{\frac{2kTx}{eE}}$$

(3.10)

where k is Boltzmann constant, T is absolute temperature, $x$ is the drift distance and E is electric field magnitude [47].

**Doping**

The doping process can be achieved by adding a specific type of atoms to a pure semiconductor material (intrinsic) to increase the number of free charge carriers. This results in an extrinsic semiconductor material with different electron and hole numbers in the band structure. There are two types of doping; n-type, where the extrinsic semiconductor material has more electrons and p-type, which

is electron-deficient. The type of doping can be distinguished by added impurities, which act either as donor or acceptor impurities. The n-type semiconductor has donor impurities that contribute to a free-electron position close to a conduction band called the donor level. Meanwhile, p-type semiconductors have acceptor impurities with one fewer valence electron than the surrounding semiconductor atoms, resulting in electron deficiency (hole). This hole lies on the acceptor level close to the valence band as shown in Figure 3.7 [47].
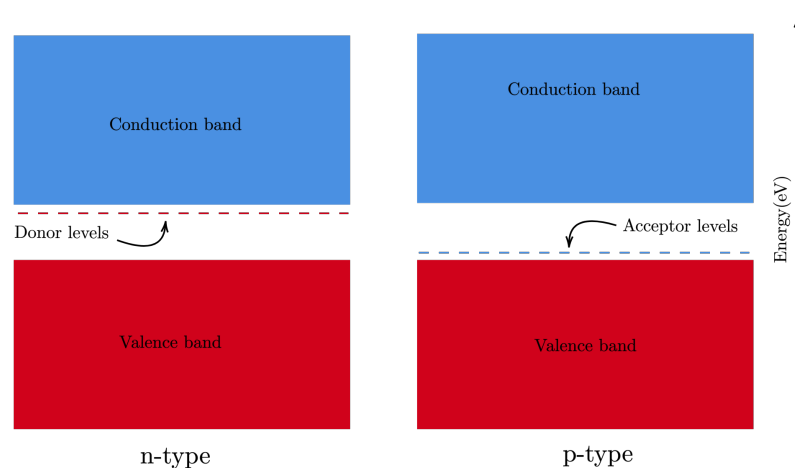


**Figure 3.7:** Schematic diagram of the band structure of n-type and p-type semiconductors, showing the donor and acceptor levels.

### The p-n Junction

The p-n junction combines an n- and p-type semiconductor material together under thermal equilibrium to be used as radiation detectors. Practically, it is hard to combine the two types of material without a small gap that is considered large compared to the interatomic lattice spacing. To that end, the doping process will be different for either side of the junction to the other in the same crystal. The p-n junction has a different charge carrier concentration on each side, which causes diffusion. The n-type side of the junction has a higher density of conduction electrons than the p-type side, so the electrons diffuse towards the p-type side and produce a net positive space charge; the hole density is higher on the p-type side of the junction, so it diffuses towards the n-type side and produces a net negative space charge, resulting in an electric potential difference ($V_{internal}$) across the junction. At equilibrium, the generated internal electric field will be adequate to prevent further diffusion and therefore establish a steady-state charge distribution. The region where the internal electric field extends free of charge is called the depletion region [44]. This is an essential component in detecting

radiation because of the electric field effect in this region and is mainly influenced by semiconductor impurity concentrations and the intensity of the electric field. Any radiation interaction in the depletion region produces charge carriers that are swept back toward the n-type side for electrons and the p-side for a hole. Eventually, the motion of the charge carriers forms an electrical signal that can be collected through electrical contacts placed on either side of the junction. In the small thickness of the depletion region, the charges can be trapped due to a relatively slow movement to the contacts and incomplete charge collection. A sufficient external voltage is applied to the junction as a reverse bias ($V_{bias}$) where a negative voltage is applied to the p-type side or a positive bias is applied to the n-type side. This increases the thickness of the depletion region as shown in Figure 3.8. The depletion region width (W) can be determined by calculating:

$$W \cong \sqrt{\frac{2\epsilon V_{bias}}{qN}} \tag{3.11}$$

where N is the impurity concentration, $\epsilon$ the dielectric constant of the medium and q the carrier charges [48].
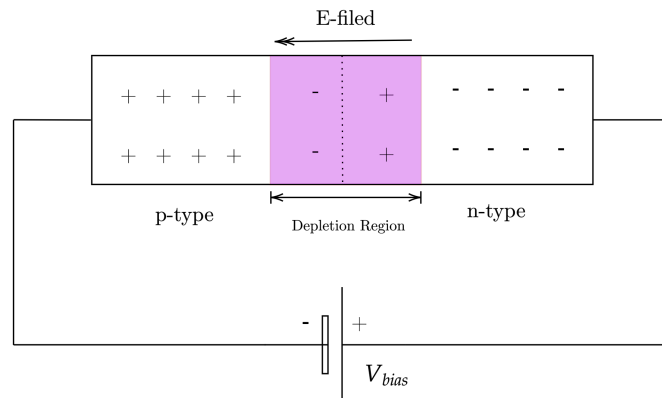


**Figure 3.8:** Schematic diagram of p-n junction with applied external voltage $V_{bias}$, reproduced from [46]

**Generation of electrical signals**

The interaction of radiation within the depletion region of a semiconductor detector produces free charge carriers along the gamma-ray path. With the presence of the electric field produced by $V_{bias}$, the charge carriers will move toward the electrodes to be collected either toward anode for electrons or toward cathode for holes. The movement of charge carriers induces an electric current on the electrodes, which continues until all charge carriers are collected as described by the

Shockley-Ramo theorem.  A time and a position-dependent signal can then be produced [49], the magnitude of which can be used to determine gamma-ray energy. The time evaluation of this signal gives an essential knowledge of the effects of the radiation interaction position on the shape of the pulse [44]. To that end, it is essential to understand how to calculate the amount of induced charge on the electrode, the electric field and the weighting potential through the detector's volume.  The Shockley-Ramo theorem can be used to determine the amount of instantaneous induced current ($i$) on the electrode and is given by:

$$i = -q \overrightarrow{\nu}.\overrightarrow{E_0}\left(x\right) \tag{3.12}$$

where q is the charge, $\overrightarrow{\nu}$ is the instantaneous velocity of the carrier and $(\overrightarrow{E_0})$ is the weighting field [44].  The same principle can be used to calculate the total induced charge (Q) by using the variation in the weighting potential ($\varphi_0$) from location $x_i$ to location $x_f$:

$$Q = -q\left[\varphi_0\left(x_f - \varphi_0\left(x_i\right)\right)\right] \tag{3.13}$$

The weighting field and the weighting potential measure electrostatic coupling between the external charge and the electrode and describe the electric field and potential at the charge's location under certain conditions; when the electrode of interest is set at unit potential, all other electrodes have zero potential and there are no other charge sources [50]. In addition to these conditions, it is necessary to solve the Laplacian equation for the detector geometry to calculate the weighting potential as a function of position.  If the weighting potential and the actual electric fields inside the detector are identified, the Shockley-Ramo theorem can be used to describe the pulse shape.  Determining the actual electric fields is important because it determines the drift velocity of charge carriers inside the detector [50]. Using the electric field ($E$) and the electric potential ($\varphi$) relationship is a common approach for calculating the electric field:

$$\overrightarrow{E} = -\bigtriangledown \varphi \tag{3.14}$$

The electric potential can be obtained by solving Poisson's equation as given:

$$\bigtriangledown^2 = \varphi = -\frac{\rho}{\varepsilon} \tag{3.15}$$

where $\rho$ is the intrinsic space charge density and $\varepsilon$ is the dielectric constant of the detector material.

**Preamplification**

The induced charge produced following a gamma-ray interaction is relatively small and must be magnified, so charge-sensitive preamplifiers are used to integrate the induced current into a larger charge pulse while maintaining the noise at the lowest level possible. The charge-sensitive preamplifier consists of the capacitor $C_i$ that collects the charges, which are then integrated and discharged by the feedback loop of a capacitor $C_f$ and resistor $R_f$, as shown in Figure 3.9. The total integrated charge is proportional to the output voltage. The produced pulse rise time depends on the charge collection and decay times determined by the time-constant equal to $R_f$ $C_f$ [44].
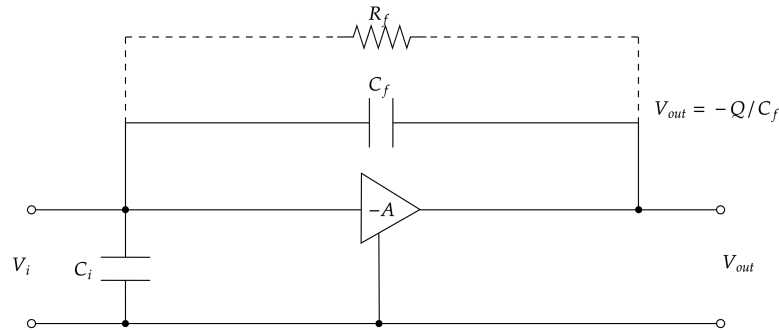


**Figure 3.9:** Schematic diagram of charge-sensitive preamplifiers circuit [44]

## 3.2.2   Energy resolution

It is essential to achieve a high-quality image from the Compton camera system for proton beam range verification. In order to achieve a high-quality image, the detector should have excellent energy resolution to precisely determine the energy deposited in each detector and accurate position information to define the scattering angle and the cone axis. Energy resolution is one of the essential performance metrics that can quantitatively measure the ability of a detector system to measure the deposited energy. The energy distribution of the incident radiation forms a Gaussian spectral peak and the Full Width at Half Maximum (FWHM) of this peak is used to define the energy resolution. Three factors contribute to the overall energy resolution ($\Delta$E) and can be calculated by:

$$(\Delta E) = \sqrt{(\Delta E_E)^2 + (\Delta E_X)^2 + (\Delta E_S)^2} \qquad (3.16)$$

where $(\Delta E_E)$ is the electronic noise contribution to the overall energy resolution, $(\Delta E_X)$ is the signal losses due to incomplete charge collection and leakage current

and ($\Delta E_S$) represents the statistical fluctuation of the number of charge carriers ($N_{pair}$) created following a radiation interaction in the detector which given by:

$$\Delta E_S = 2.35\sqrt{\frac{F}{N_{pair}}} \tag{3.17}$$

where F is the Fano factor [44]. The Fano factor is related to the variation in the experimentally-observed statistical fluctuation and pure Poisson statistics prediction of the charge carrier pairs [47].
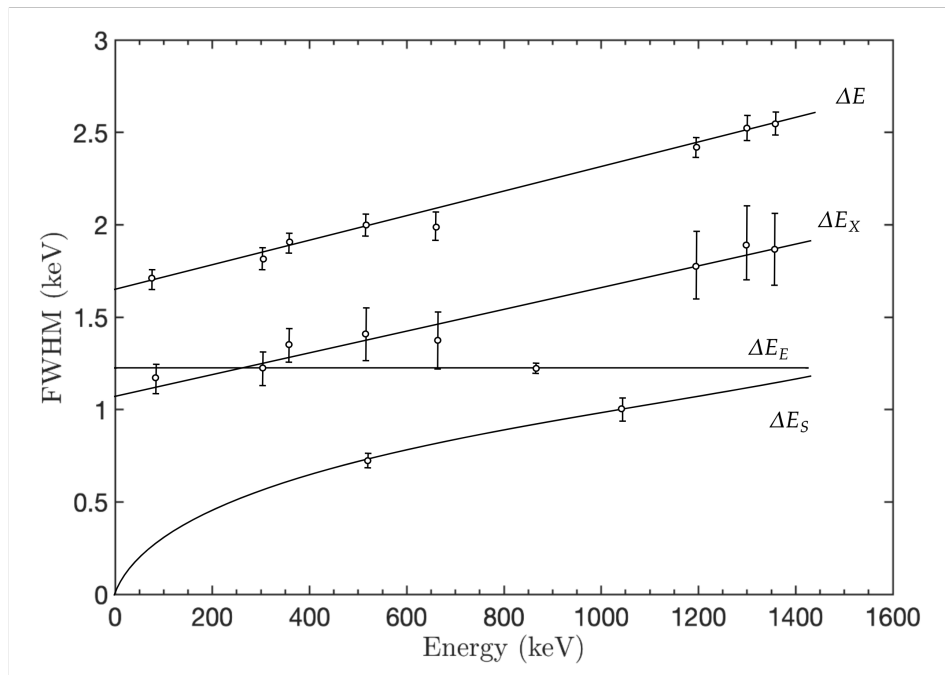


**Figure 3.10:** The contribution of three energy resolution factors to the overall energy resolution ($\Delta E$) for 86 $cm^3$ HPGe detector. Reproduced from [44]

The three factors contribute to the overall energy resolution ($\Delta E$) are respond differently to the energy. $\Delta E_E$ is constant as a function of the energy, $\Delta E_X$ has a linear response to the energy and $\Delta E_S$ is a non-linear response to increasing the energy as shown in Figure 3.10 [44]. In proton radiotherapy, the $\Delta E$ is therefore expected to degrade for the higher energy prompt $\gamma$. In Compton imaging, this is mitigated somewhat by splitting the total incident $\gamma$ into smaller fractional deposits in each detector.

# Chapter 4

# Operation principles of the Gri+ system

The Gri+ system consists of three detectors with cooling systems, a digital data acquisition system and a PC, all mounted in a cart to allow transportation to measurement sites. A photograph of the system is shown in Figure 4.1. Each part of the Gri+ system plays a specific role in achieving gamma-ray imaging; this chapter thus outlines the specifications for the detectors and electronics systems, as well as the software and methods used to achieve data sorting.
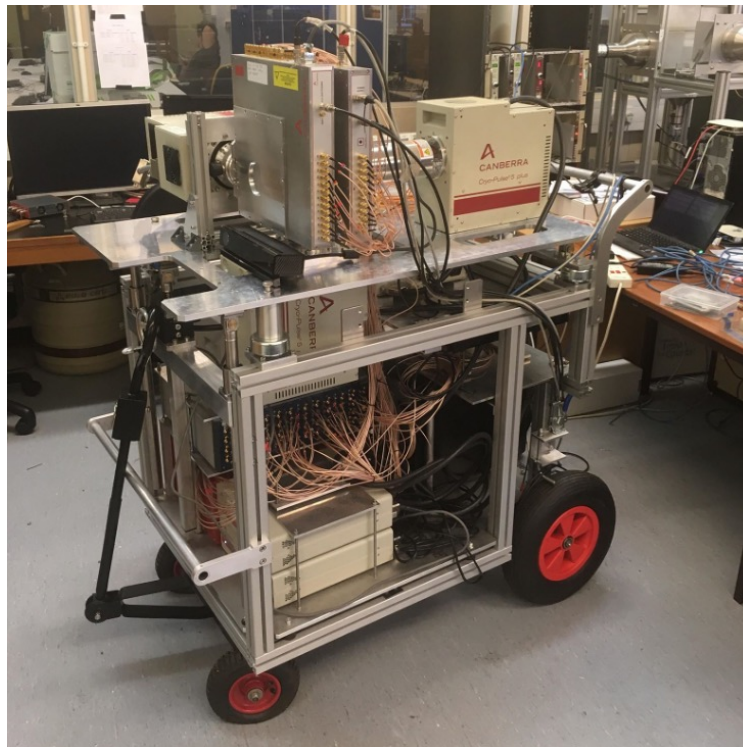


**Figure 4.1:** Photograph of the Gri+ system. The detectors can be seen on the top face of the cart with the electronics are housed beneath them.

## 4.1   Gri+ components

### 4.1.1   Detectors

Gri+ is a three-tier semiconductor Compton camera that consists of two position-sensitive planar detectors and a single coaxial detector, all developed by Mirion Technologies.  All three detectors are cooled by Cryo-Pulse 5 (CP5) electrical coolers, and the tiers are named after the role they play in the Compton camera system. The first tier of the Gri+ serves as a scatterer detector, with its material and design being selected to maximise Compton scattering for gamma-rays in the expected energy range. The second tier is an absorber, so the design and the material have been selected to maximise the probability of photoelectric absorption of incident gamma rays. The third tier then serves as an additional absorber to improve efficiency for imaging high energy gamma rays that do not deposit all their energy across the first two detectors.

**Scatterer detector**

The first tier is a planar detector made of Lithium-drifted Silicon (Si(Li)). The detector crystal has a cylindrical shape of 8 mm thickness and 71 mm diameter, offering an active area of $3500\,mm^2$. The crystal is surrounded by a guard ring of 5 mm thickness, and the whole structure is housed in the centre of an aluminium cryostat, as shown in Figure 4.2. The crystal operates at a positive bias of 430 V, which is well above the depletion voltage of +150 V. Both sides of the detector are segmented into 13 orthogonal strips that have 5 mm pitch and are separated by a distance of 0.5 mm, which results in a sensitive position resolution of 5.5 x 5.5 x 8 $mm^3$ This can be further improved by the later addition of pulse shape analysis techniques. The front section has 13 horizontal p-type contacts coupled to AC charge-sensitive preamplifiers, while the rear has 13 vertical n-type contacts coupled to DC charge-sensitive preamplifiers. All preamplifiers are set in a cold Field Effect Transistor (FET) configuration. Each strip has a different length depending on its location on the detector surface, however. A detailed report on the charge collection properties of the detector can be found in [51].
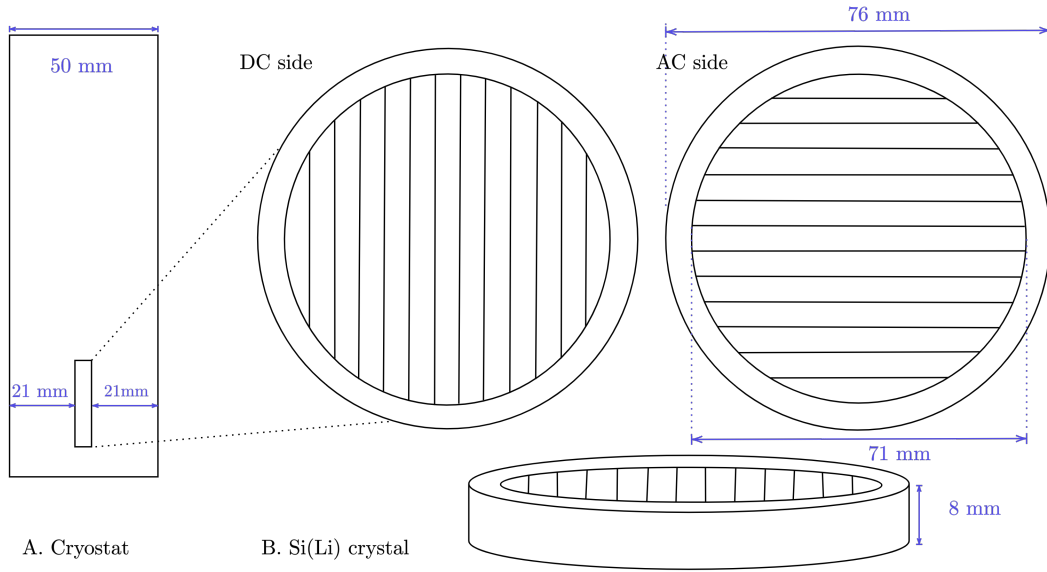
**Figure 4.2:** Schematic illustrations of (A) the side view of the cryostat housing the Si(Li) detector and (B) the dimensions and segmentation scheme of the Si(Li) detector.

The detector has been refurbished several times since the published performance in [51] Therefore, prior to using the detector for imaging purposes in this thesis, an initial measurement set was acquired to demonstrate detector performance and to verify the results against the manufacturer's specification sheet. Each strip was measured individually for energy resolution and noise level. The energy resolution measurement was undertaken using a spectroscopy amplifier (Canberra Model 2026) with shaping time of 4 $\mu s$, connected to a Multi Channel Analyser (ORTEC Model ASPEC-927). MAESTRO software was then used to determine the energy resolution based on calculating the FWHM. This was achieved by performing a Gaussian fit over the full peak of energy of interest. Since the detector is selected for its scattering properties rather than absorption, there is a low probability of observing high energy photopeaks. Therefore, the energy resolution has been measured using the 59.5 keV gamma-rays emitted from $^{241}$Am point sources. Figure 4.3 shows the measured and reported manufacturer's energy resolution for all strips. The initial measurement agreed with the manufacturer measurement apart from AC 11, which was not working, so it will be excluded from the average of the energy resolution. The average energy resolution at 59.5 keV was found to be 1.15 ± 0.06 keV for the AC side and 0.88 ± 0.05 keV for the DC side, consistent with the manufacturer's energy resolution. In addition, the scatterer detector energy resolution has been evaluated using the digital data acquisition system (see Section 4.1.2). Using two point-like sources $^{241}$Am and $^{57}$Co, with analysis undertaken of the 59 keV and 122 keV gamma-rays, respectively.

The AC side average energy resolution is 1.39 ± 0.1 keV and 1.49 ± 0.1 keV for 59 keV and 122 keV, respectively. The DC side average energy resolution is 1.12 ± 0.1 keV and 1.22 ± 0.1 keV for 59 keV and 122 keV, respectively. The scatter detector achieved an energy resolution less than 2 keV, which is excellent energy resolution to generate high-quality images in Compton camera configuration. The energy resolution degraded in the AC side relative to the DC side due to the load resistor present in an AC coupled preamplifier circuit [50].

It is essential to quantify the noise level in each strip to distinguish between signals produced from gamma-ray interactions and electrical noise in the system. To this end, the noise level was measured separately for all detector strips by calculating the value of peak-to-peak noise in each case. The average values of this peak-to-peak noise were 11.43 ±1.19 mV and 10.4 ± 1.04 mV for the AC and DC sides, respectively.
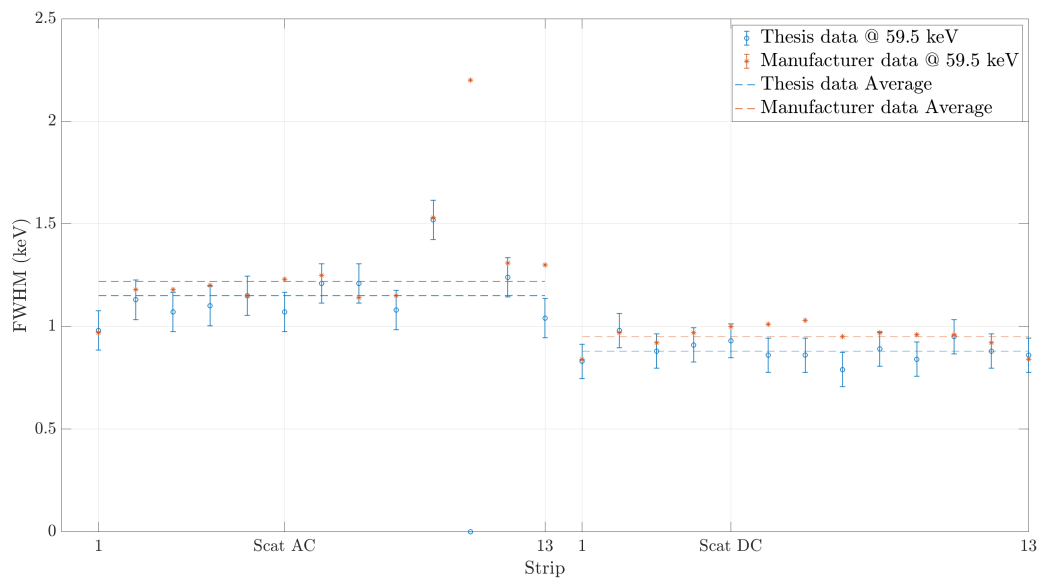


**Figure 4.3:** AC and DC side energy resolution measured for the scatterer detector in this thesis and by the manufacturer.

## First Absorber

The second tier is a planar detector made of high-purity germanium (HPGe). The detector crystal is a cuboid of 60 mm length and width, with a thickness of 20 mm, giving an active area of $3600\,\text{mm}^2$. The crystal is surrounded by a guard ring of 7.5 mm and housed in the centre of an aluminium cryostat, as shown in Figure 4.4. The crystal operates at a negative bias of 1,800 V which is above the depletion voltage of -1,300 V. Both sides of the detector are segmented into 12 orthogonal strips with 5 mm pitch. The strips on the AC and DC sides have separation gaps of

0.3 mm and 0.25 mm, respectively, which result in a position sensitive resolution of $5\,\text{mm}^3 \times 5\,\text{mm}^3 \times 20\,\text{mm}^3$ [52]. This can be improved, however, by the use of pulse shape analysis techniques which will be described in Section 4.2.5. The front side has 12 horizontal p-type contacts coupled to the AC charge-sensitive preamplifiers and the rear has 12 vertical n-type contacts coupled to the DC charge-sensitive preamplifiers. All preamplifiers are arranged in a cold Field Effect Transistor (FET) configuration, to minimise noise contributions.
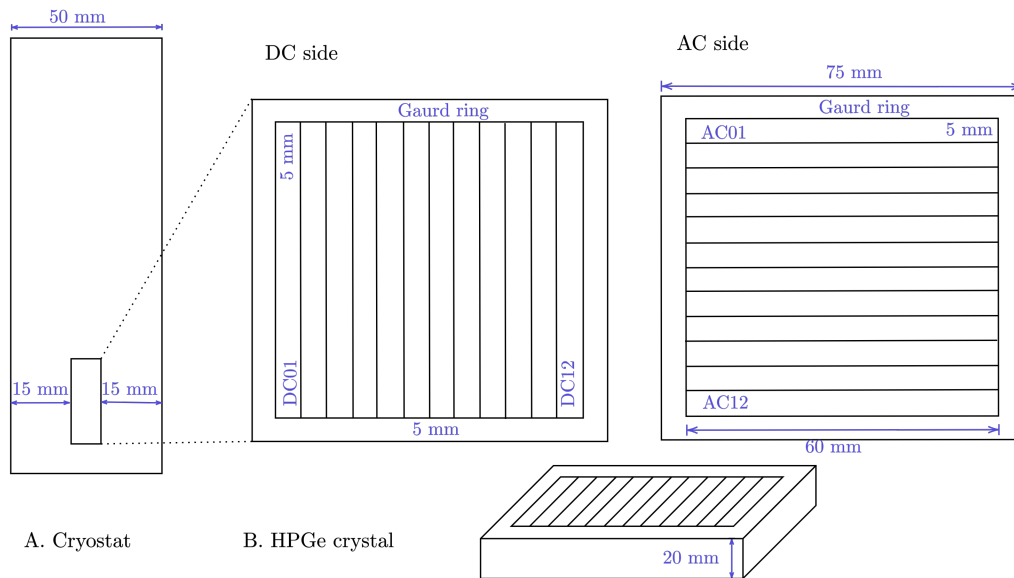


**Figure 4.4:** Schematic diagram of the first absorber detector (A) the side view of the cryostat housing the HPGe detector and (B) the dimensions and segmentation scheme of the HPGe detector.

Initial measurements were conducted to demonstrate detector performance, with the energy resolution and noise level measured separately for each strip. The same electronics set up of spectroscopy amplifier and multi-channel analyser was used for these measurements as for the scatter detector. To measure energy resolution, data were acquired using two point-like sources $^{57}$Co and $^{60}$Co, with analysis undertaken of the 122 keV and 1332 keV gamma-rays.
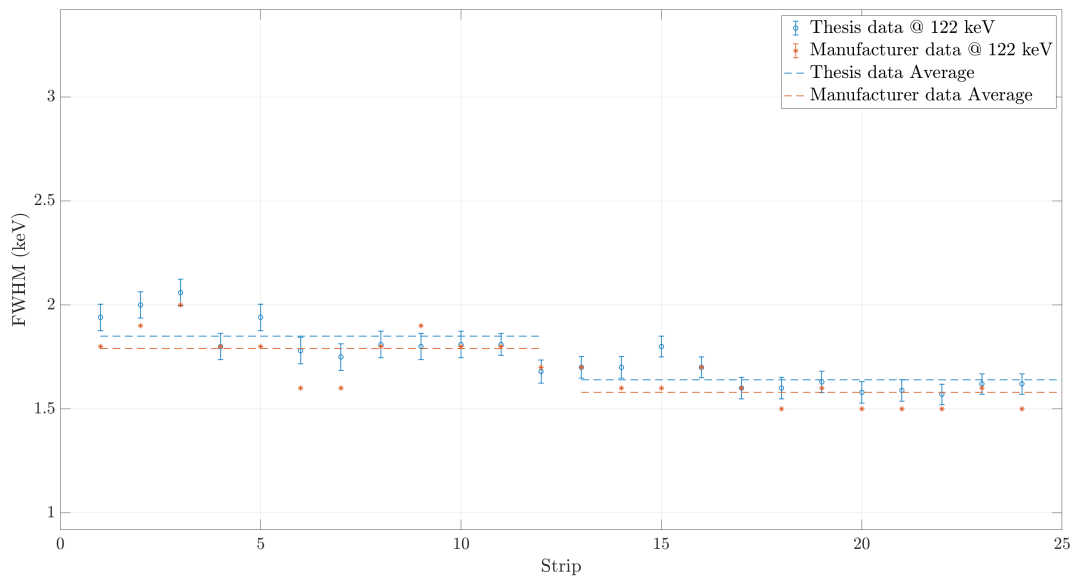
**(a)** The first absorber detector energy resolution at Low energy
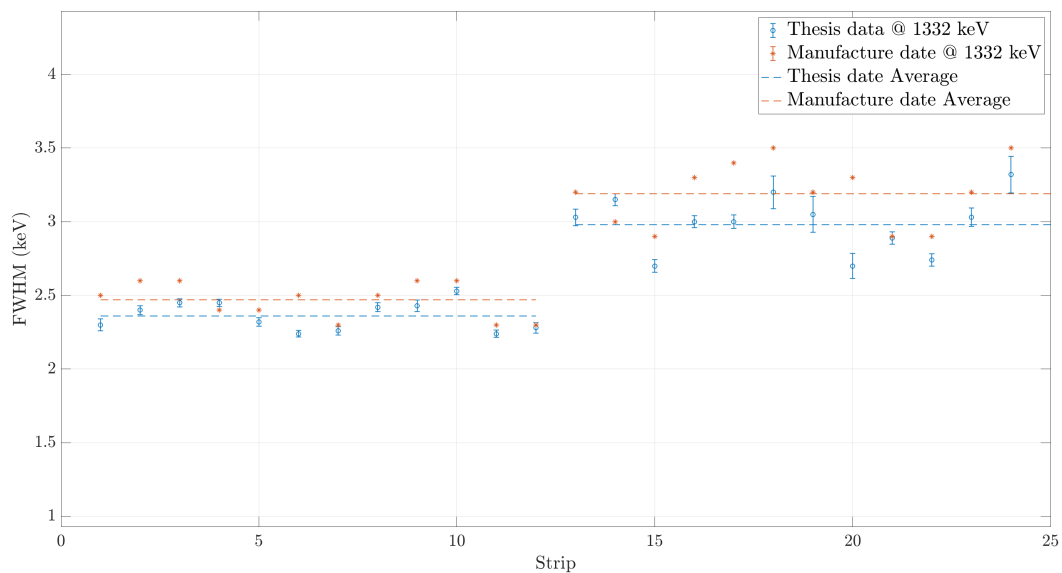


**(b)** The first absorber detector energy resolution at High energy.

**Figure 4.5:** AC and DC side energy resolution for the first absorber detector at (a) Low energy; (b) High energy.

The average energy resolution using 122 keV gamma ray energy was found to be 1.85 ±0.08 keV for the AC side and 1.6 ±0.07 keV for the DC, whilst at 1332 keV was 2.4 ±0.09 keV on the AC side and 2.9 ± 0.1 keV on the DC side. The measured energy resolution was consistent with the manufacturer's specifications, as shown in Figure 4.5.

The noise level was measured separately for all detector strips by calculating the value of peak-to-peak noise in each case. The average values of this peak-to-

peak noise were $10.24 \pm 1.08$ mV and $10.17 \pm 1.05$ mV for the AC and DC sides, respectively. This detector has previously been characterised in more detail by Rintoul et al [53].

In addition, the first absorber detector energy resolution been evaluated using the digital data acquisition system (see Section 4.1.2). Using same two point-like sources, with analysis undertaken of the 122 keV and 1.3 MeV gamma-rays. The AC side average energy resolution is $2.3 \pm 0.1$ keV and $2.8 \pm 0.04$ keV for 122 keV and 1.3 MeV, respectively. The DC average energy resolution is $1.92 \pm 0.1$ keV and $3 \pm 0.1$ keV for 122 keV and 1.3 MeV, respectively. The first absorber energy resolution shows superior energy resolution for the DC side at low energy. However, at high energy, the energy resolution degraded. In contrast, the energy resolution for the AC side degraded at low energy and showed superior energy resolution at high energy.
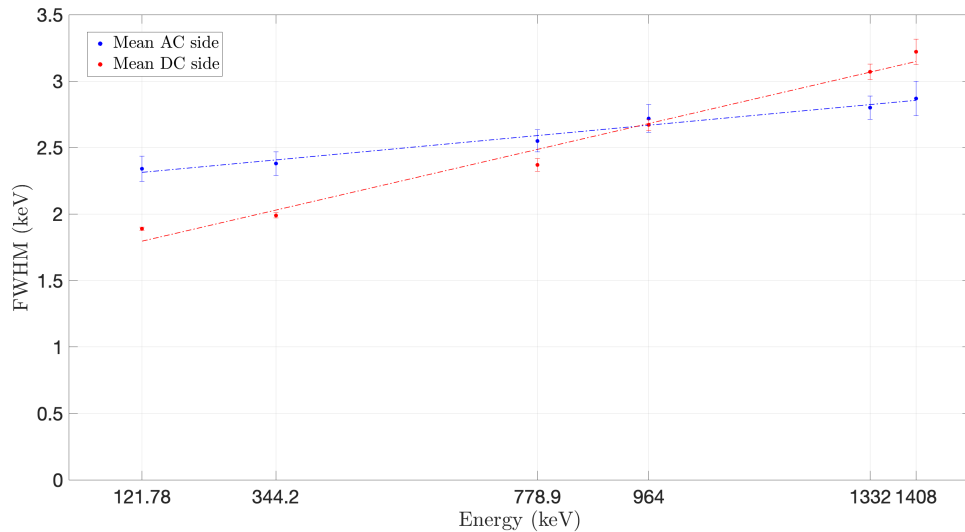


**Figure 4.6:** AC and DC side average energy resolution as function of energy for the first absorber detector.

The first absorber energy resolution over a range of energy from 121 keV to 1.4 MeV shows a linear energy resolution response for the AC and DC side, as shown in Figure 4.6. The AC and DC side energy resolution discrepancy is due to the DC side energy resolution being dominant by factors that contribute to the overall energy resolution. The main factors that contribute to the overall energy resolution are $\Delta E_S$, $\Delta E_X$ and $\Delta E_S$ which were respond differently to the energy. The electronic noise ($\Delta E_S$) is constant as a function of the energy. However, the signal losses due to incomplete charge collection ($\Delta E_X$) has a linear response to the energy. The statistical fluctuation of the number of charge carriers ($\Delta E_S$) is a non-linear response to increasing the energy as depicted in Figure 3.10 in

previous chapter. The AC have a higher electronic noise level but is subject to less degradation over the energy. However, at the high energy, the DC side energy resolution being dominant by $\Delta E_X$ and $\Delta E_S$. This discrepancy in the energy resolution for the AC and DC side as a function of energy suggest considering using the AC side energy rather the DC side energy for gamma-ray that deposit over than 900 keV of its energy in the first absorber. This will be further investigated in Chapter 5 where the Gri+ system is evaluated for higher energy.

**Second Absorber**

The third tier detector is a standard electrode coaxial germanium (SEGe) detector with a thickness of 50 mm and a diameter of 66.5 mm. This is a p-type detector with no position sensitivity, with an n-type contact on the outer surface and a p-type contact on the inner electrode, coupled to a charge-sensitive preamplifier in a cold FET configuration. The crystal operates at a positive bias of 3,000 V, which is above the depletion voltage of +2,500 V. This large volume of crystal is most suitable for the role as second absorber in the Compton camera as higher energy gamma rays may not be fully absorbed in the first two detectors. Having a third tier in the system thus increases system efficiency, especially for high energy gamma rays, such as prompt gamma emissions during proton therapy (up to 6.2 MeV). Position resolution is not required for the third detector as its only purpose to select events that are then tracked in the first two detectors. The methodology used to measure detector energy resolution was the same as for the two strip detectors. The energy resolution at 122 keV and 1332 keV were found to be 0.68 keV and 1.74 keV, respectively.

## 4.1.2 Data acquisition system

The Gri+ system uses various electronic components to supply the power required for the detectors to operate and for the digital acquisition system that is used to process and store the preamplifier signals.

**Power Supply**

Three components supply the Gri+ system with essential power. These are a compact High Voltage (HV) power supply (DT55xxE CAEN), a custom-built Low Voltage (LV) supply unit with 12 V and 24 V rail power, and an uninterruptible power supply (Riello Sentinel PRO 700VA UPS), with the latter being able to keep the system running for a few hours should the other sources fail. All of these are mounted on the custom-designed cart.

**Digital acquisition hardware**

The digital data acquisition system used in Gri+ allows storage and analysis of the preamplifier signals output by the detectors. The user can thus conduct both online and offline advanced interpretation of the energy and other interesting signal parameters. All preamplifier signals from the detectors are fed into a gain and offset (GO) box, which amplifies the signals by a fixed gain factor to maintain the full dynamic range of the CAEN cards (2.25 V), then applies an offset to the signal voltage to adjust the baseline position. For this thesis, the gain factor been used for the scatterer detector was 5, and for the first absorber detector was two and with no gain factor for the second absorber detector. The amplified signals are then passed to the CAEN digitiser modules. The final system output is recorded to disk by the computer as shown in Figure 4.7. The system has eight CAEN modules cards placed in an eight-slot VME64 mini crate (CAEN VME8008B). Six of these are digitiser cards (CAEN V1724), each with eight 14-bit channel inputs and a sampling frequency of 100 MHz; these are used to sample the analogue signals output from the GO box using a flash Analog-to-Digital Converter, with the results stored in local memory [54]. All of the cards are loaded with firmware developed by CAEN known as Digital Pulse Processing for Pulse Height Analysis (DPP-PHA) [55]. Due to the limited 48 input channel of the digitiser cards, three strips must be excluded, however. Within the scatterer detector, AC 1, AC 13, and DC 1 are the edge strips with the smallest volume and these are thus selected for exclusion to minimise loss of detection efficiency. However, the AC 13 strip has been used because the AC 11 strip is not working. One general-purpose VME board (CAEN V1495) is used to set and synchronise the global clock and to specify the triggering logics, such as the coincidence triggering logic [56]. The final card is the VME to PCI bridge (CAEN V2718), which connects the digitisers to the computer through an optical link.
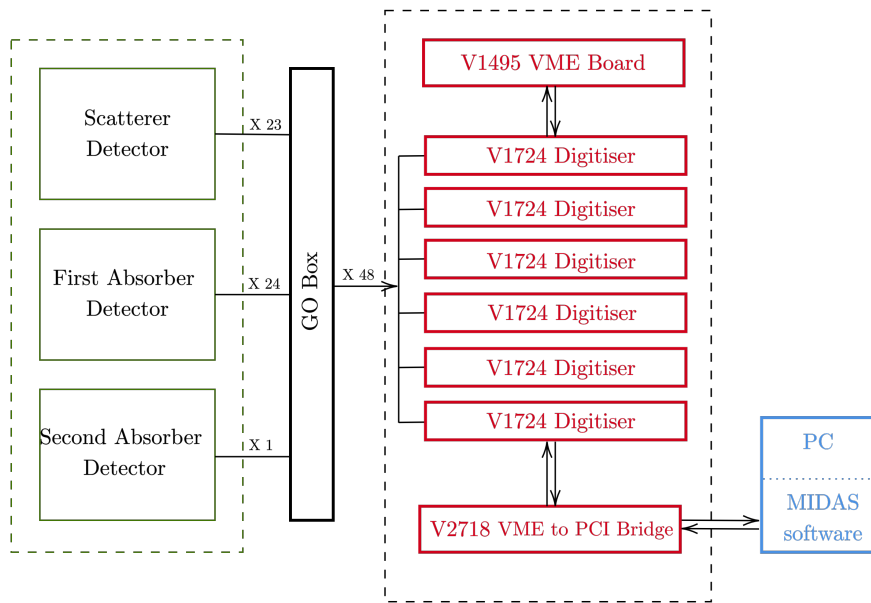
**Figure 4.7:** Digital system overview.

**Digital acquisition software**

The Gri+ system uses Multi Instance Data Acquisition System (MIDAS) software [57] to control the DPP-PHA firmware. MIDAS software provides a web interface that gives the user the ability to modify the setting of the CAEN V1495 VME board and CAEN V1724 digitiser cards, as well allowing the triggering and cessation of the data acquisition process. The signal received must meet the requirements of the trigger logic in the CAEN V1495 before being passed to the digitiser cards for processing. Within the MIDAS software, the V1495 VME board parameters can be adjusted to support various specific trigger logics. One of the main parameters is the trigger mode, and the user can select either single mode or coincidence mode, depending on the purpose of the experiment. Generally, single mode is used for energy calibration and optimising system algorithms, while coincidence mode is used when the Gri+ system acts as a Compton camera. In the single mode, the system reads all channels when only one signal from any detector passes the trigger threshold; this trigger mode is thus usually used when operating a single detector. In coincidence mode, the signal must pass the trigger threshold in both the scatterer detector and the first absorber detector within a specific time, which is defined by the user setting a time coincidence window. As the threshold has been passed in the front two detectors, the data is thus categorised as a two-tier event, although if the signal also passes the trigger threshold for the second absorber within the coincidence window, it is then categorised as a

three-tier event.

Another CAEN V1495 parameter that must be set is the output mode, which determines the number of channels read out after the specific trigger logic is met. The output mode offers three options: Output as Input Masked, Output as All Masked, and Output Nearest Neighbour. In the Output as Input Masked mode, only channels that successfully triggered the logic will be read out; in Output as All Masked mode, all channels will be read out after a successful triggered; while in Output Nearest Neighbour mode, the system reads out only the channel with the successful trigger and its two neighbouring channels.

Any signal that meets the trigger criteria will pass to the CAEN V1724 digitiser cards. These digitiser cards are loaded with DPP-PHA firmware that uses an online trapezoidal filter within the FADC unit to calculate the energies deposited in the detector. The trapezoidal filter is based on the moving window deconvolution (MWD) method [58], and it is thus labelled MWD in this work. The MWD is applied on a preamplifier signal with a short risetime and a long decay time, and this process has three stages (Figure 4.8):

1. The preamplifier signal is converted into a step function signal with the same signal height by removing exponential decay.

2. A square signal is obtained by differentiating the signal achieved in the first step.

3. A trapezoidal shape signal is achieved by implementing a moving average window on the step signal from the previous step, which smooths the signal and removes noise.

The trapezoidal signal height was used in this work to determine the energy deposited in the detector. Several MWD parameters must be optimised to achieve optimum performance in the system, including trapezoid rise time and trapezoid flat top. Once the signal has been digitised and the deposited energy calculated by the MWD, the output data from the signal samples, timestamp, channel number and energy is produced.
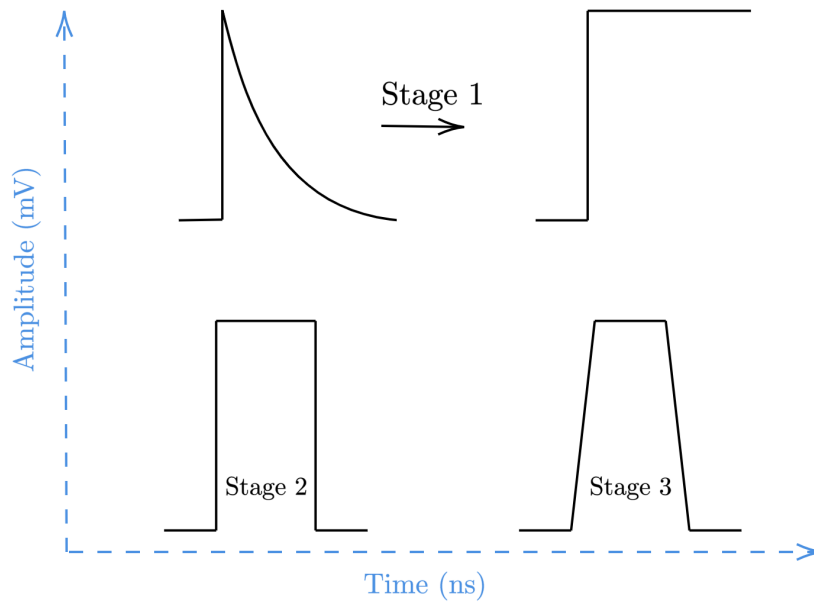
**Figure 4.8:** The main stages of MWD algorithm.

## 4.2   Data sorting process

The data obtained from the digital acquisition system can be sorted online or offline using sorting software. However, before any experiment, it is necessary to calibrate the system to optimum use of all algorithms.

### 4.2.1   Sorting software

MTsort [59], the sorting software used to process the data, was developed at the University of Liverpool. The MTsort programming language supports C-algorithms and develops a specific sorting language to sort the data before applying more advanced algorithms such as baseline difference (BLD) methods and PSA algorithms (see section 4.2.5). MTsort can also be used to visualise the different types of spectra in one dimension and two dimensions. The main spectra of interest are the individual spectra for each strip, the addback spectra for each side of the AC and DC scatterer and absorber detectors, and the Compton addback spectra, which is the total energy deposited from the scatterer and absorbers' detectors in coincidence mode.

   Three types of signals are possible in the Gri+ system: real, transient-induced charge, and noise as shown in Figure 4.9. The charge collection on a contact following gamma-ray interaction represents the real signal; however, the charge collection on the adjacent contact will have a transient-induced charge signal, also

known as an image charge.  The third type of signal is noise, arising from the various electronic components.
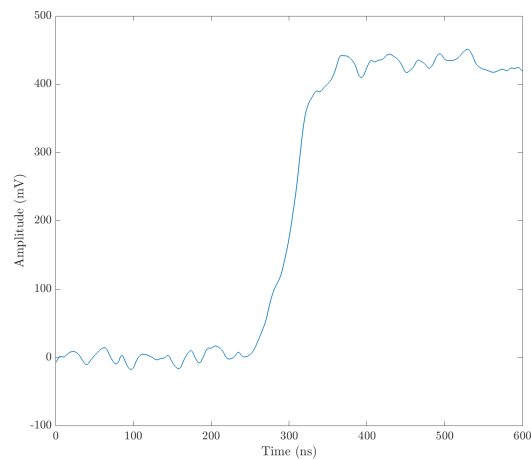


**(a)** Real signals
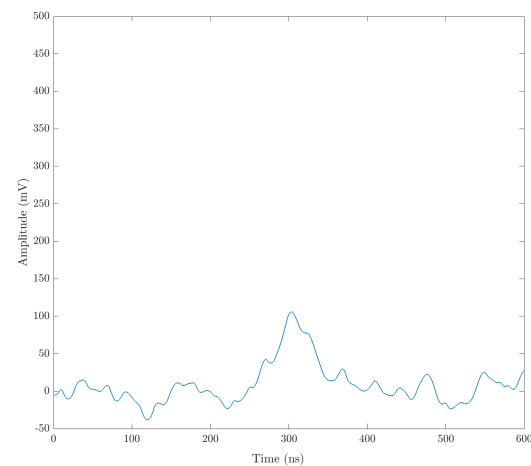


**(b)** Transient-induced charge signals
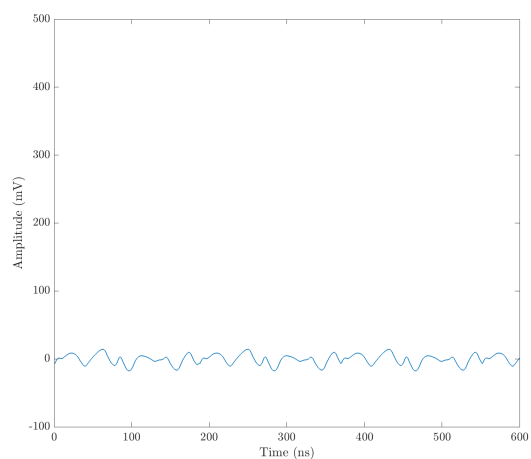


**(c)** Noise signals

**Figure 4.9:**  Three types of signals are possible in the Gri+ system:  real, transient-induced charge, and noise.

The sorting software applies further analyses to the digitiser signal using the baseline difference (BLD) method, which can distinguish between a real signal and a transient-induced charge or noise, as well as being able to determine the event fold classification (see Section 4.2.3). The BLD method works by comparing the standard deviation ($\sigma$) of the signal noise over the samples before interaction occurs with the average amplitude of the signal over the last 30 samples as depicted in Figure 4.10. If the difference is greater than $3\sigma$ the signal is considered to be a real signal. Where a signal is considered a real signal based on the BLD method, the calculated energy from the MWD can be used for imaging, as the energy calculated by MWD is more accurate than that calculated by BLD. After the data processing is completed, MTsort produces a text file containing the event interaction position for the scatterer and the first absorber and the deposited energy within all three detectors. This text file is then used in the image reconstruction code to produce the relevant images.
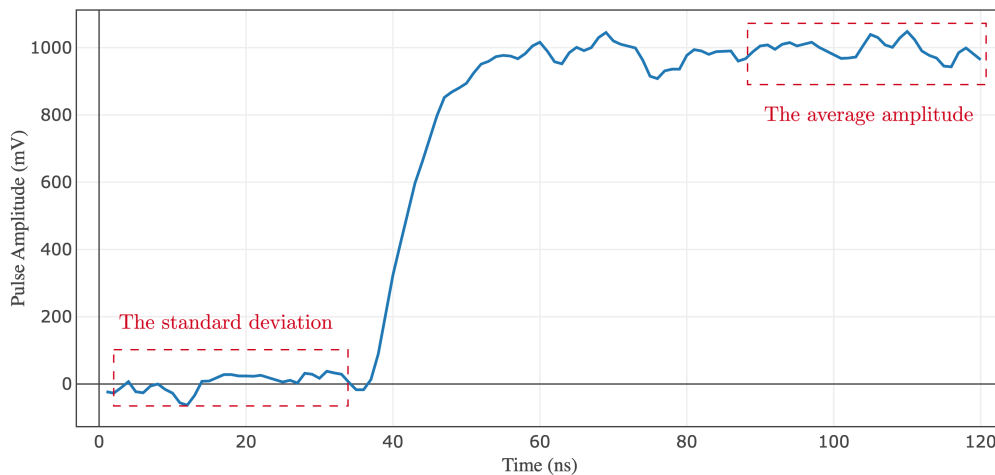


**Figure 4.10:** Preamplifier signal showing averages used in BLD methods.

## 4.2.2  Energy Calibration

All 48 channels of the Gri+ system need to be calibrated individually before the system can be used to assess experimental data due to the segmented design of the scatterer and first absorber, as well as the need to add the energy from all three detectors together in coincidence mode, which necessitates individual calibration to develop accurately calibrated Compton addback spectra. Energy calibration is also required when applying energy gates during the sorting process. The calibration coefficients ($a$, $b$, and $c$) can be calculated using the quadratic equation ($E = ax^2 + bx + c$), where $x$ is the channel number of the peak centroids for a gamma ray energy $E$. This quadratic is produced by plotting the channel

number of the peak centroids and the associated gamma ray energy and applying quadratic fitting for three or more energies. The focus of this thesis is to image the prompt gamma ray during proton therapy, which can be up to 10 MeV. The energy of the prompt gamma ray is split between the three detectors so it is expected that the detectors may record up to a few MeV in the absorber detectors, whilst the energy recorded in the scatter detector is typically much lower. A 1.8 MeV gamma ray from a $^{88}$Y point-like source is included in the energy calibration for both absorber detectors, as this is the highest gamma ray energy source available in the lab.

### 4.2.3   Detector Fold

Gamma rays can deposit their energy across the detector system in a large variety of sequences, including both single and multiple interaction events. The gamma-ray energy, atomic number of the detector material, and thickness can all affect the interaction mechanisms of gamma rays within the detectors. The event will be categorised depending on the fold distribution for scatterer, first absorber and the entire Gri+ system when operated in coincidence mode to have Compton image and will be as the following for Scatter detector:

- Fold 1

    - $F_S[1,1]$: a single real event registered on the AC and DC sides of the detector.

- Fold 2

    - $F_S[1,2]$: a single real event registered on the AC side and two real events registered on the DC side.

    - $F_S[2,1]$: two real events registered on the AC side and a single real event registered on the DC side.

    - $F_S[2,2]$: two real events registered on the AC and DC sides of the detector.

- Fold 3

    - $F_S[1,3]$: a single real event registered on the AC side and three real events registered on the DC side.

    - $F_S[3,1]$: three real events are registered on the AC side and a single real event is registered on the DC side.

- $F_S[3,2]$: three real events are registered on the AC side, and two real events are registered on the DC side.

- $F_S[2,3]$: two real events registered on the AC side and three real events registered on the DC side.

- $F_S[3,3]$: three real events registered on the AC and DC sides of the detector.

The first absorber detector event categorisation is similar to scatterer detector event categories as $F_A[1,1]$, $F_A[1,2]$, $F_A[2,1]$ and $F_A[2,2]$ as shown in Figure 4.11. In the following discussion regards the fold distribution for each detector , the event category called Fold1 will represent by $F_S[1,1]$ for scatterer detector or $F_A[1,1]$ for first absorber detector, however, Fold 2 will represent by $F_S[1,2]$, $F_S[2,1]$ and $F_S[2,2]$ for scatterer detector or $F_A[1,1]$, $F_A[1,2]$, $F_A[2,1]$ and $F_A[2,2]$ for first absorber detector. Fold 3 will represent by $F_S[1,3]$, $F_S[3,1]$, $F_S[3,2]$, $F_S[2,3]$ and $F_S[3,3]$ for scatterer detector or $F_A[1,3]$, $F_A[3,1]$, $F_A[3,2]$, $F_A[2,3]$ and $F_A[3,3]$ for first absorber detector. Any other fold distribution combination does not mention before will be called Higher fold.

The Gri+ system event categorisation represents the number of real events registered on each detector, and such events can be categorised into three-tier or two-tier events depending on whether the second absorber detector registers the real event or not, as determined using the method described in section 4.2.1. For the Gri+ system fold, the event will be categorised as Fold 1 when both detectors are categorised as Fold 1. However, if one of the detectors have Fold 1 event and the other has a Fold 2 event, or both of them has Fold 2 event, the event will be categorised as Fold 2. For an event categorised as Fold 3, if any detectors have Fold 3 or each detector has Fold 3, then the event will be categorised as Fold 3. The "Higher fold" category represents all other events that pass the trigger threshold, which might be fold-3 or various Fold-1 and Fold-2 events otherwise excluded due to multiple interactions within a strip.
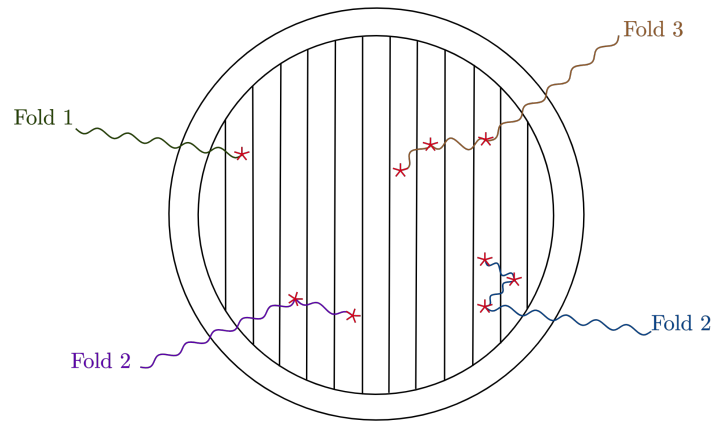
**Figure 4.11:** Fold 1 indicates a single interaction on each side of the detector, and Folds 2 and 3 indicate multiple interaction events. Red stars indicate the strip that detects a particular interaction.

Low energy gamma rays are more likely to undergo photoelectric absorption, which is where the gamma ray deposit all their energy in the detector, creating a Fold 1 event; this contrasts with high energy gamma rays, which can undergo Compton scattering that may result in any number of strips that register real signal on each side the detector. In proton beam therapy, the prompt gamma of 4.4 MeV ($^{12}$C), and 6.1 MeV ($^{16}$O) are the most prominent gamma lines. The dominant interaction mechanism of these energies is Compton scattering.

The planar detectors are made from different materials and of different thicknesses so as to maximise Compton imaging events. The gamma ray interaction properties depend on the gamma ray energy, the atomic number of the detector material, and detector thickness and therefore the fold classification requires separate investigation for individual planar detectors in addition to investigative the Gri+ system while operated in coincidence mode. Three experiments were conducted to explore fold classification for gamma-rays in the energy range 59.5 keV to 1.4 MeV using $^{241}$Am and $^{152}$Eu point-like sources. Individual experiments were conducted for each planar detector with the digital data acquisition system in singles mode, while a third experiment examined the Gri+ system fold where the system operated in coincidence mode.

**Scatterer detector fold**

In the scatterer detector, the 59.5 keV,121.8 keV, 244 keV and 344.2 keV were examined. It was difficult to explore energy higher than those because the higher energy gamma ray will not deposit full energy in the scatterer detector therefore only the full photopeak of the low energy has been observed in scatterer detector. An energy gate of 2 keV was applied on the energy. The Fold categorisation as

a function of gamma-ray energy for scatterer detector is shown in Figure 4.12.
For all four energies earlier mentioned, most of the event experience photoelectric
absorption and classified as Fold 1. However, over the range of the energy, only 9
% to 11 % of the event was Fold 2 in the scatterer detector. A very small fraction
of the events were categoriesed as Fold 3 and no event was categoriesed as Higher
fold.
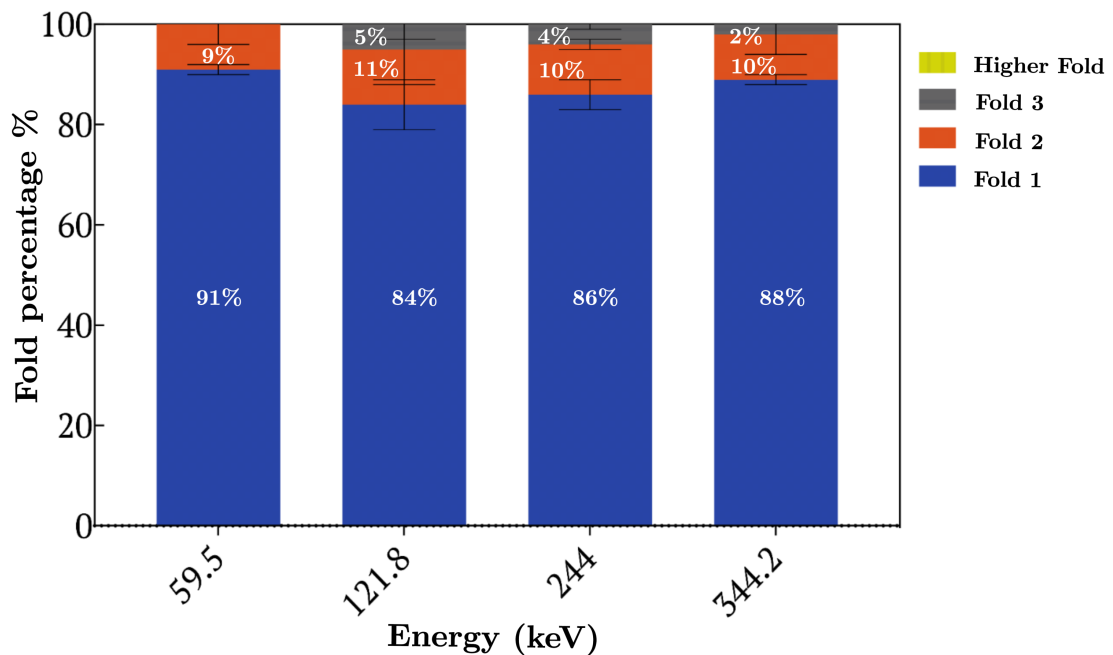


**Figure 4.12:** Fold categorisation as a function of gamma-ray energy for the scatterer
detector.

**First absorber detector fold**

Figure 4.13 shows the distribution of fold determined for the absorber detector as
a function of gamma-ray energy. A dependence of the fold on energy is evident.
As gamma-ray energy increases, the number of Fold 1 events decreases, while the
number of Fold 2 as well as Fold 3 events increases. For the 121 keV gamma-ray,
87 % of the events were classified as Fold 1 events, while 10 % of the events were
classified as Fold 2 events. However, only 11 % of the events were classified as Fold
1 event compared to 48 % and 38 % of the events were classified as Fold 2 and
Fold 3 events, respectively, for the 1.4 MeV gamma-ray. Only 3 % was classified
as Higher fold. The fold distribution demonstrates the importance of using Fold
2 events in the production of gamma-ray images in high energy applications such
as for proton beam verification where high statistics improves image quality.
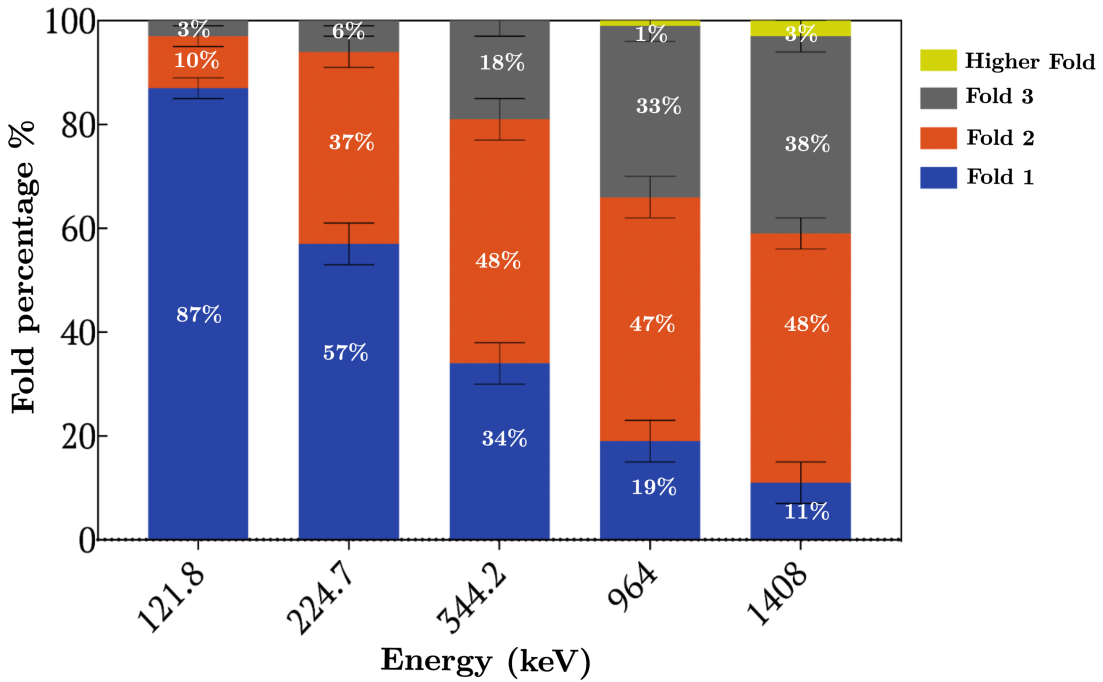
**Figure 4.13:** Fold categorisation as a function of gamma-ray energy for the first absorber detector.

**Gri+ system fold**

The distribution of event folds for the Gri+ system operated in coincidence mode as a function of gamma ray energy is shown in Figure 4.14. It can be seen that the fraction of Fold 1 events continually decreases alongside increases in the energy of the gamma rays, in contrast to the Fold 2 events, which increased with the increase in gamma ray energy up to 344 keV, at which point they tended to stabilise. It is because the Compton scatter probability is dominant at gamma-ray energy above 200 keV in the first absorber detector. So the incoming gamma-ray scatters multiple times and deposits some of its energy when scattering up until the rest of this gamma-ray energy becomes lower than 200 keV, where the probability of the photoelectric absorption is dominant and then fully absorbed. It can be seen in Figure 4.14 that Fold 3 events increased with the gamma energy increase. It also noticed that the percentage of Fold 3 events doubled between gamma energy of 224 keV and 344 keV because the gamma-ray has enough energy to continue scattering. For the 121 keV gamma-ray, 86% of the events were classified as Fold 1 events and only 14% of the events were classified as Fold 2 events. However, about 20% of the events were classified as Fold 1 events and about 35% of the events were classified as Fold-2 events for the 1.4 MeV gamma-ray. So the fold level tends to increase with an increase in the gamma energy, in agreement with the individual detector fold study.
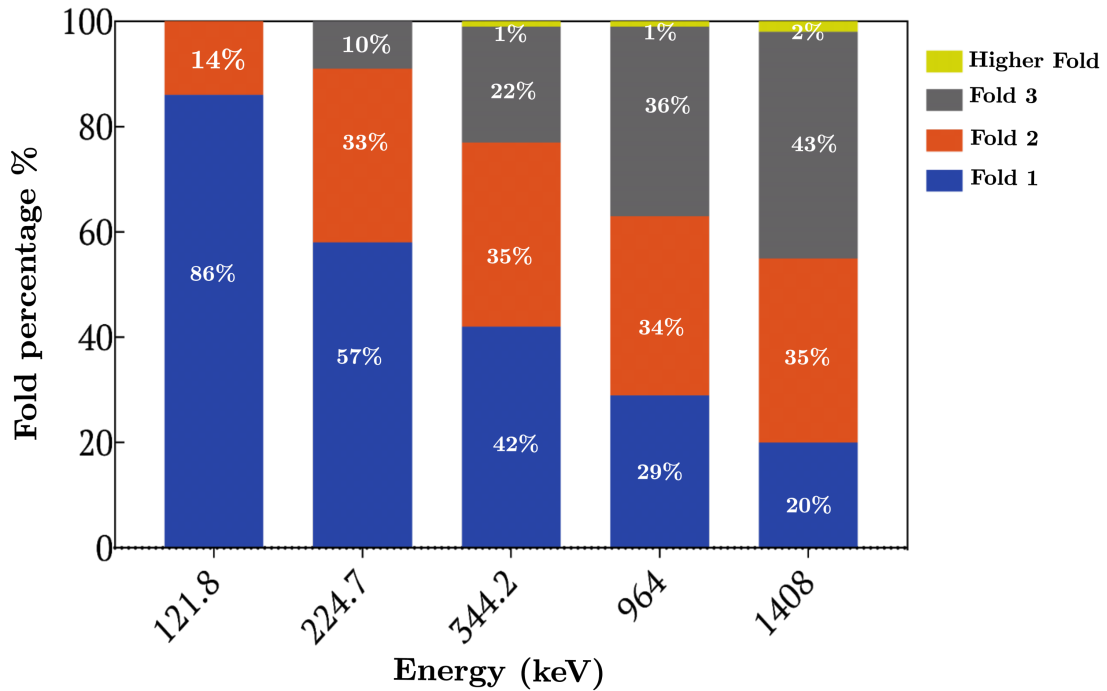
**Figure 4.14:** Fold categorisation as a function of gamma-ray energy for the Gri+ system for both 2-tier and 3-tier.

Using a second absorber detector in Gri+ system been explored. The purpose of using the second absorber is highlighted as shown in Figure 4.15. For the 121 keV gamma-ray, all events were categorised as two-tier events, which means that interactions only occurred within the two planar detectors at low energy. However, at 1.4 MeV, about 35% of the events were categorised as three-tier events, as these interactions occurred within all three detectors. In medical applications, using two planar detectors for Fold-1 events offers the optimum solution for low energy (121 keV) gamma rays; however, for high energy gamma rays (1.4 MeV), using all three detector and incorporate Fold-2 events increases Gri+ system efficiency from 14% (Fold 1, 2-tier) of events to 55% (Fold 1 and Fold 2, 2 and 3-tier). The Gri+ system imaging resolution is examined further in Chapter 5, and this includes an investigation of the effect of including Fold-2 events on the imaging resolution.
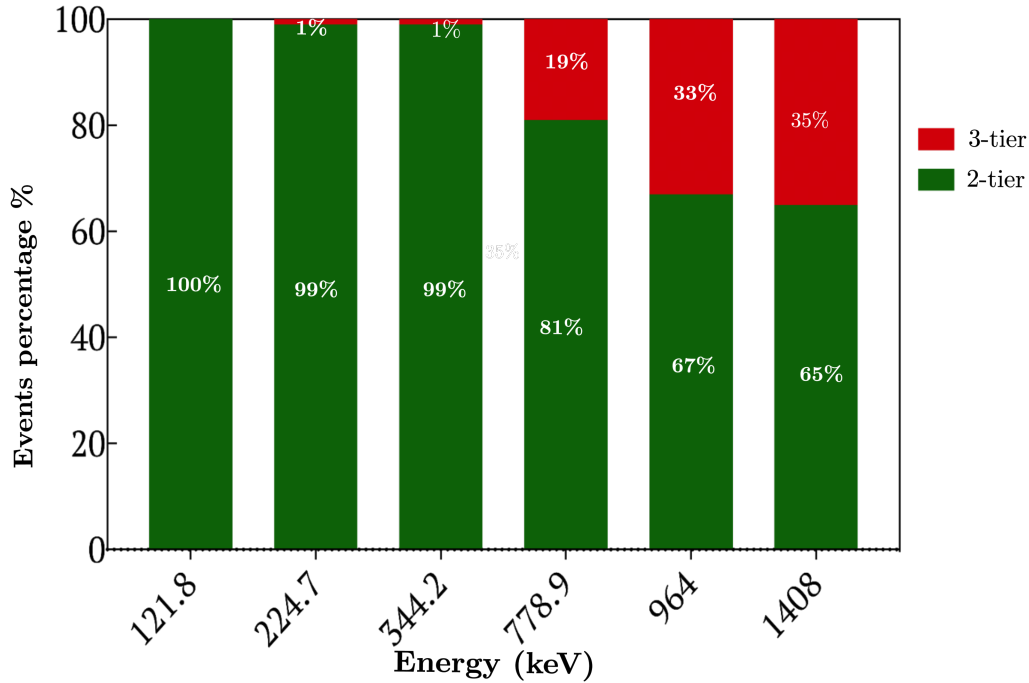
**Figure 4.15:** The event categories of three-tier and two-tier events for the Gri+ system including Fold-1, Fold-2 and Fold-3 events.

## 4.2.4 Crosstalk Correction

The crosstalk phenomenon is caused by unwanted electronic couplings between neighbouring strip contacts within the detector. In the Gri+ system, both the scatterer and first absorber are double side strip detectors, and proportional crosstalk is observed as a proportional shift in the baselines of those channels neighbouring a "hit" strip [60]. Unfortunately, the MWD algorithm incorrectly calculates the energy deposited from a transient signal in a neighbouring strip caused by this phenomenon. These transient signals have a shifted baseline, however, and in the addback energy spectra, the energy deposited in individual strips each side of the detector can be added altogether with these transient signals, resulting in peak broadening or peak splitting. This shows that the crosstalk effect is increased with both fold and energy increases which makes crosstalk correction is essential for high energy and Fold-2 events, as such peak broadening and subsequent peak splitting will be magnified, especially for the gamma ray energy range used in this thesis. Figure 4.16 shows the uncorrected and corrected addback energy spectra of Fold-1 and Fold-2 events for low and high energy gamma rays.
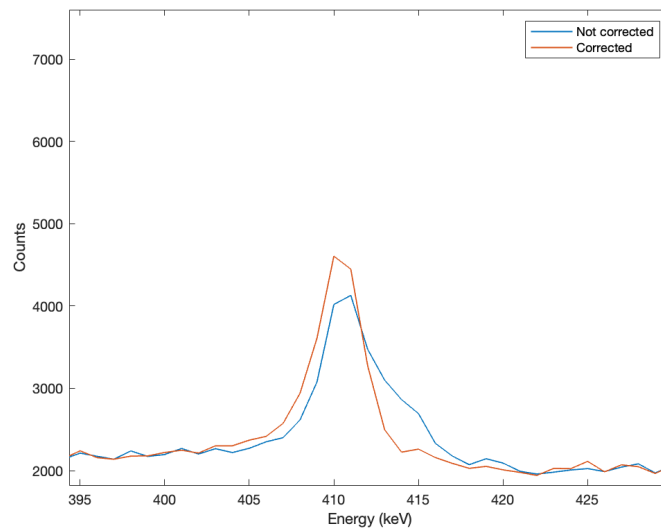
**(a)** Low energy, showing a broad peak
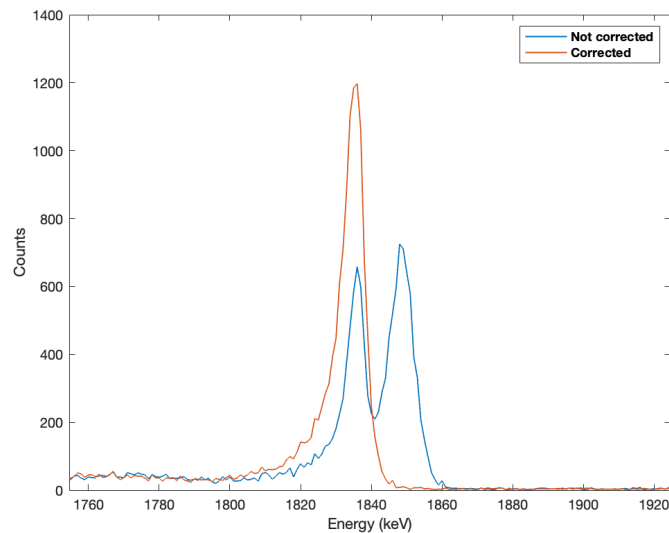


**(b)** High energy, showing a split peak.

**Figure 4.16:** The addback energy spectra of the first absorber including Fold-1 and Fold-2 events (a) Low energy, showing a broad peak; (b) High energy, showing a split peak.

Crosstalk can be corrected by applying a linear correction factor to the shifted energy. This factor can best be identified by plotting the value of shifting (keV) against the energy given in the literature for the specific type of gamma rays and applying a linear fit, as shown in 4.17. The slope $m$ and the intercept $c$ from the linear fit will applied to the shifted energy using this equation:

$$E_{corrected} = E\,(1 + m) - c \tag{4.1}$$

The crosstalk correction can be applied on both the AC and DC sides of both detectors; however, only higher fold events in adjacent strips will be corrected, as only these events show this shifted energy. The MTsort software can implement such corrections while sorting the data.
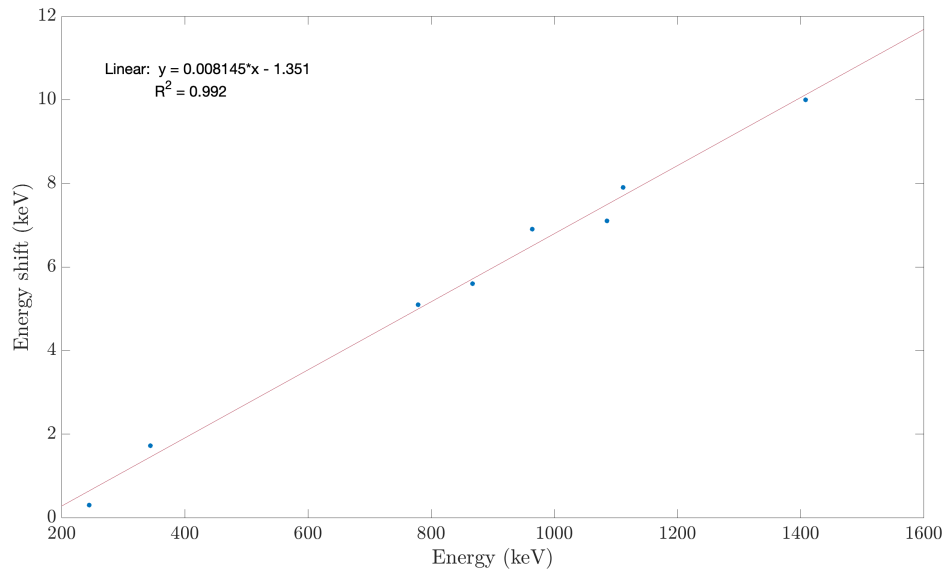


**Figure 4.17:** Plot of the value of shifting (keV) against the gamma ray energy from the literature with a linear fit applied to produce the correction factor.

## 4.2.5   Pulse Shape Analysis

Previous studies of the Gri+ detectors have shown that a Pulse Shape Analysis (PSA) algorithm can be used to improve the determination of gamma interaction position within the detectors [53]. The front two detectors of the Gri+ system are segmented into voxels by orthogonal strip contacts. These voxels each represent 5.5 x 5.5 x 8 $mm^3$ in the scatter detector and 5 x 5 x 20 $mm^3$ in the first absorber detector. Based on the assumption that gamma ray interactions occur at the central (x, y, z) coordinates of voxels, a high degree of interaction position uncertainty leads to significant errors in the cone axis reconstruction in the image. Online analysis (Parametric PSA) [61] and offline analysis (Database PSA) [62] methods should thus be utilised to reduce this interaction position uncertainty and subsequently improve the reconstructed image. The parametric PSA technique can be only used with Fold 1 events, while Database PSA can be used for Fold 1 and Fold 2 events.

The parametric PSA technique can be implemented in two ways. XY-PSA improves the lateral interaction position by using information extracted from the transient signals on neighbouring strips, while Z-PSA improves the depth accuracy

of the interaction position by using the risetime of the preamplifier signals. Z-PSA can thus be applied in three different types based on utilising the signal risetime: Z-PSA1 (T30 v T90 Gates), Z-PSA2 (Risetime Correlation) and Z-PSA3 (Chi-Squared Minimisation). These three techniques have previously been investigated to determine which offers the most significant improvement in image resolution [61], while database PSA methods use a simulated signal database to perform PSA analysis by comparing simulated and experimental signals [62]. In this thesis, parametric PSA3 was used for online analysis, and a database PSA was used for offline analysis.

**Parametric PSA**

**XY-PSA**   Transient signals in neighbouring strips are used to estimate the lateral interaction position of a gamma ray more accurately based on comparing the size of the transient signals to the lateral interaction position. The relationship between transient signal size and distance of interaction from neighbouring strips can then be used to improve the lateral interaction position across the width of the strip. When the interaction occurs close to a contact, a larger transient signal will be recorded on the neighbouring strip closest to the interaction, and a smaller transient signal will be recorded on the opposite neighbouring strip, as illustrated schematically in Figure 4.18.
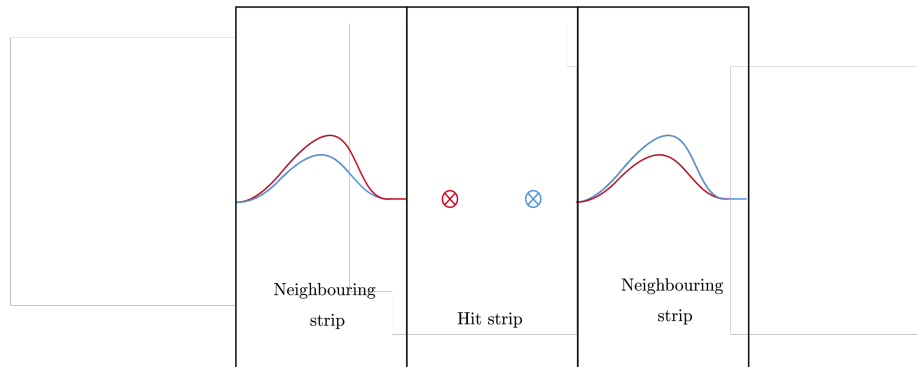


**Figure 4.18:** An example of the relationship between the lateral interaction position and the size of transient signals.

The asymmetry value of the transient signal can be calculated using the equation [63]:

$$A = \frac{Q_L - Q_R}{Q_L + Q_R} \tag{4.2}$$

where $A$ is the asymmetry value and $Q_L$ and $Q_R$ represent the areas to the

left and right of the transient signal. The value will be a function of gamma-ray interaction position and will be between 1 and -1. If A is close to 0, the interaction occurs in the centre of the strip, whilst -1 and 1 represent interactions at the boundary between the hit and neighbouring strips. These values were scaled to be 1,000 and 3,000 for use in MTsort as shown in Figure 4.19. The asymmetry value distribution thus divided the strip into five segmented areas, which improved the lateral positioning from 5.5 mm to 1.1 mm and from 5 mm to 1 mm for the scatterer and absorber, respectively.
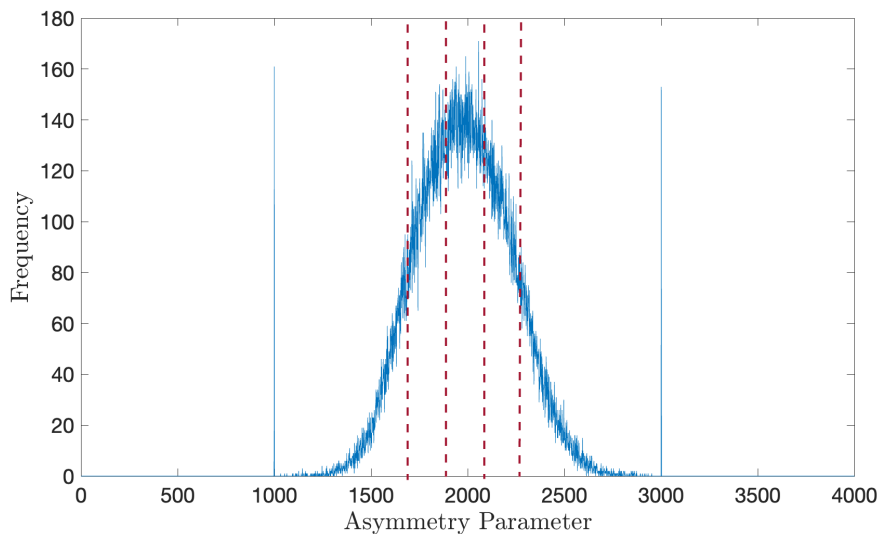


**Figure 4.19:** Asymmetry value distribution for DC6 for the first absorber; the red dashed lines show the five segmented areas of the strip.

In the work of this thesis, Asymmetry value calibration was conducted for every strip in the scatterer and the first absorber, as each strip has a different asymmetry value; this was achieved in a similar manner to energy calibration, where each strip similarly has a different variation in preamplifier gain. However, the edge strip in both detectors cannot be calibrated because they do not have two neighbouring strips. Once the asymmetry values were assessed, the MTsort code was updated to reflect these.

**Z-PSA** The risetime from a real signal can be used to reduce interaction position uncertainty throughout the detector's depth. Both detector types in this case have an electric field so that it can be assumed that the velocity of the charge carriers is saturated. Thus, the time required to collect the charge completely must depend on the carriers' travelled distance. This time information can be parameterised across the detector thickness to produce characterised values, and by comparing a specific interaction risetime to the relevant characterised values, the depth of the

interaction can thus be calculated. The scatterer detector thickness is 8 mm, and the first absorber thickness is 20 mm. Before Z-PSA methods were applied, the position of interaction was set in the centre of the detector thickness, at Z-depths of 4 mm and 10 mm for scatterer and first absorber, respectively. The significant uncertainty of the 10 mm depth thus led to a focus on the development in the first absorber. The risetime of preamplifier signals can be quantified as the 10%, 30%, 50%, and 90% values of the time taken to completely collect the charge, which are known as t10, t30, t50 and t90, respectively. For this work, the electronic noise in the initial and final 10% of the signal required exclusion of 10% of the signal; the t10 was thus subtracted from all other risetimes to achieve the more accurate T30, T50 and T90 values. Figure 4.20 shows an example of the signal, including the parameterised risetime value.
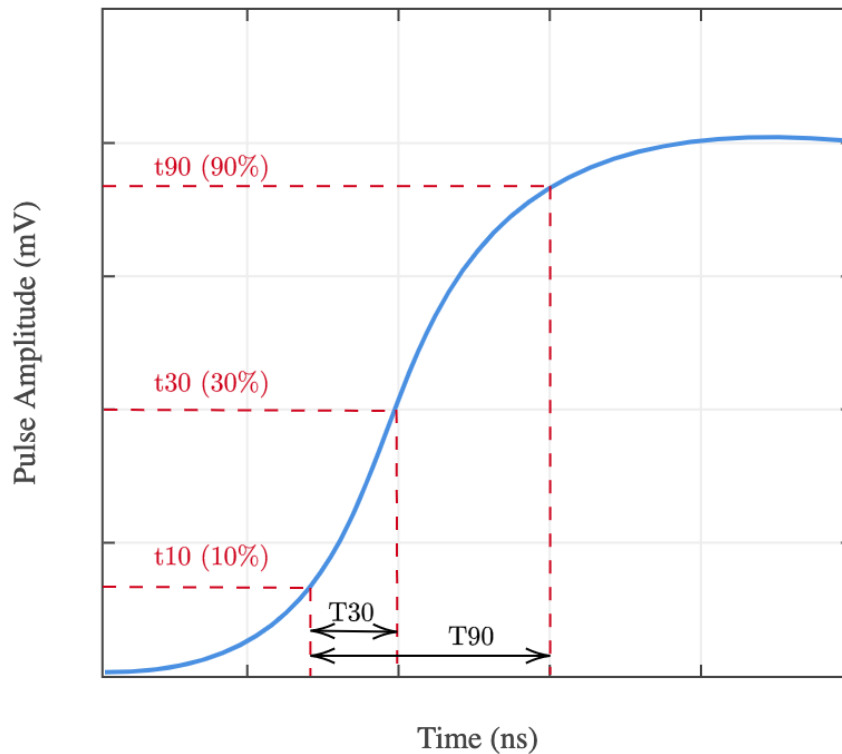


**Figure 4.20:** The 10%, 30%, and 90% risetime values of an example signal and the respective T90 and T30 values.

Z-PSA methods require prior knowledge of the risetime value as a function of z-depth, which can be achieved experimentally, as explained in [53], or by simulating the electric field through the detector [52]. In this thesis, the Z-PSA3 method was used for online analysis, as this method uses the average risetimes for a known signal position in order to determine an unknown signal position. The best match between the signals' risetimes is then chosen using a chi-squared minimisation

method. For this thesis, values for the actual signal risetime at each millimetre
were achieved by scanning the z-depth for the first absorber in a similar method-
ology used by [53]. Figure 4.21 show the average signal through each millimetre
of detector depth; theoretically, therefore, using the Z-PSA3 method reduces the
uncertainty in the position of interaction from 10 mm to 1 mm throughout the
detector depth.
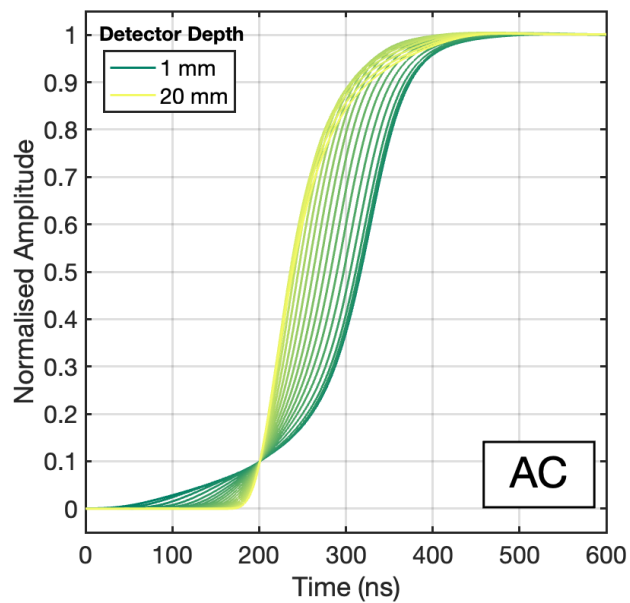


**(a)** The AC sides of the first absorber detector
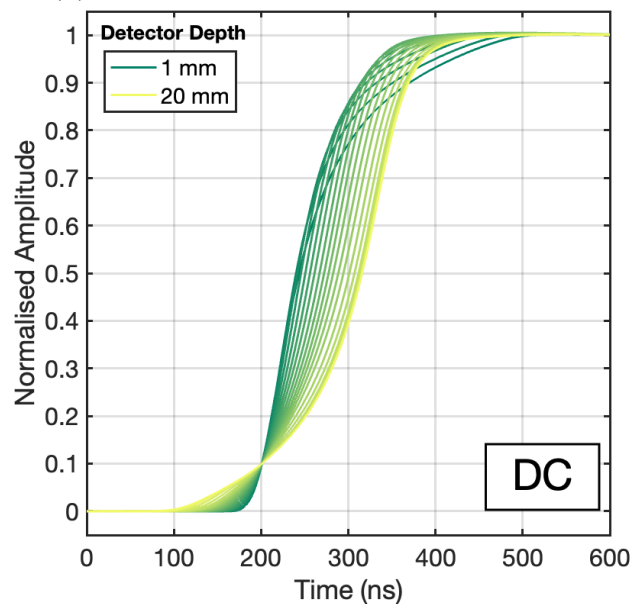


**(b)** The DC sides of the first absorber detector.

**Figure 4.21:** Average signal through 1 to 20 millimetres of detector depth for the AC
and the DC sides of the first absorber detector.

# Chapter 5

# Experimental study of Gri+ for imaging high-energy gamma rays

It is essential to examine the Gri+ system in a setting that approximates the Clatterbridge cancer centre environment. This chapter therefore examines the Gri+ system response to high-energy gamma rays. In addition to exploring the event fold distribution, this study assesses the usefulness of the Compton imaging resolution at high gamma-ray energy and in relation to more complex event sequences than reported in previous studies. This renders it possible to select the most appropriate setting for the Gri+ system in the context of proton therapy. To achieve these objectives, the Gri+ system is examined using the highest gamma-ray energies available in the laboratory and a reasonably long half-life of 106 days, which is the 1.8 MeV $\gamma$-ray emitted from $^{88}$Y. This is a suitable source since it the closest energy available to the prompt gamma ray energy that would be observed in the Clatterbridge cancer centre environment. In this chapter, the energy deposited within the scatterer and the first absorber are explored. This is followed by an evaluation of the individual and entire system fold distribution, after which the Compton image resolution for different fold levels is discussed. Finally, this chapter explores the Gri+ system setup and the most suitable setting for high energy gamma ray is proposed.

## 5.1   Analysis of gamma-ray energy spectra

The Gri+ system was operated in a similar setup that will be used in the proton therapy. Analyses of the energy spectra will reveal valuable information about the system's response to a high energy gamma ray. This information can be used to understand the range of the energy measured, which depends on the incident $\gamma$ energy and range of allowed scattering angles by the system geometry and the

detector's performance for spectroscopy (i.e. energy resolution). The spectroscopy information will contribute to the Compton imaging resolution because energy is used to determine the scattering angle and therefore the cone apex angle. In addition, using a calculated method to optimize the geometrical setup and system parameters and then validated with the experimental result will introduce a technique to predict the system response for measuring higher-energy $\gamma$-rays, including the 4.4 MeV and 6.1 MeV $\gamma$-rays, during proton therapy. To this end, an $^{88}$Y point source at 25 cm standoff was used. An energy gate on the total energy deposited in the system of 1.836 MeV was applied. There was no fold gate applied and the Gri+ system was operated in a coincidence mode.
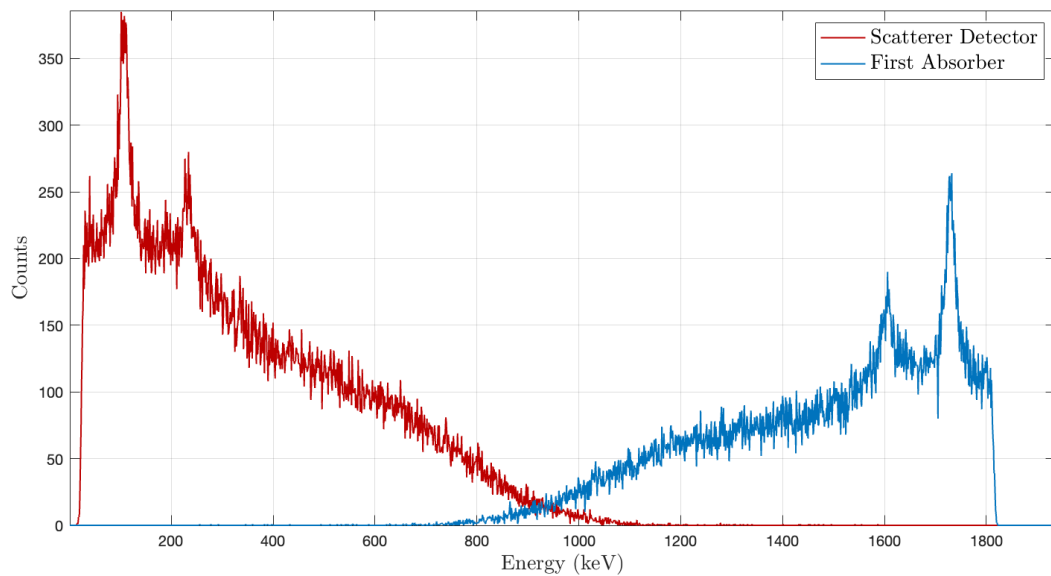


**Figure 5.1:** The DC addback energy spectra for the scatterer and the first absorber detectors with gate on the total energy of 1.8 MeV deposited in the system. There was no fold gate applied and the Gri+ system was operated in a coincidence mode.

Figure 5.1 shows the DC addback energy spectra for the scatterer and the first absorber detectors with a gate on the total energy of 1.8 MeV deposited in the system. Since no fold gate is applied, the $\gamma$-rays can interact multiple times with a minimum of once in each detector. The figure shows the energies added back across the DC strips in each detector, demonstrating total energy deposition by each $\gamma$ in each detector. The scatterer detector addback energy spectrum (red) reveals that the deposited energy range reached approximately 1.18 MeV. The minimum energy deposited for the first absorber detector (blue) was about 670 keV and the maximum energy deposited was around 1.82 MeV.

The energy deposited in the first absorber detector is dependent on the Compton scattering angle for the 1.8 MeV gamma-ray. Figure 5.1 reveals that the

probability that the 1.8 MeV gamma-ray deposited the rest of its energy in the first absorber detector between 670 keV to 1.2 MeV is low relative to 1.2 MeV to 1.8 MeV. The probability increases from 1.2 MeV to approximately 1.5 MeV, after which it plateaus, with the exception of two close peaks. The corresponding Compton scattering angles for the range 670 keV to 1.82 MeV have been calculated using equation 2.1 assuming a single scattering and added to the addback energy spectrum of the first absorber detector, as illustrated in Figure 5.2.
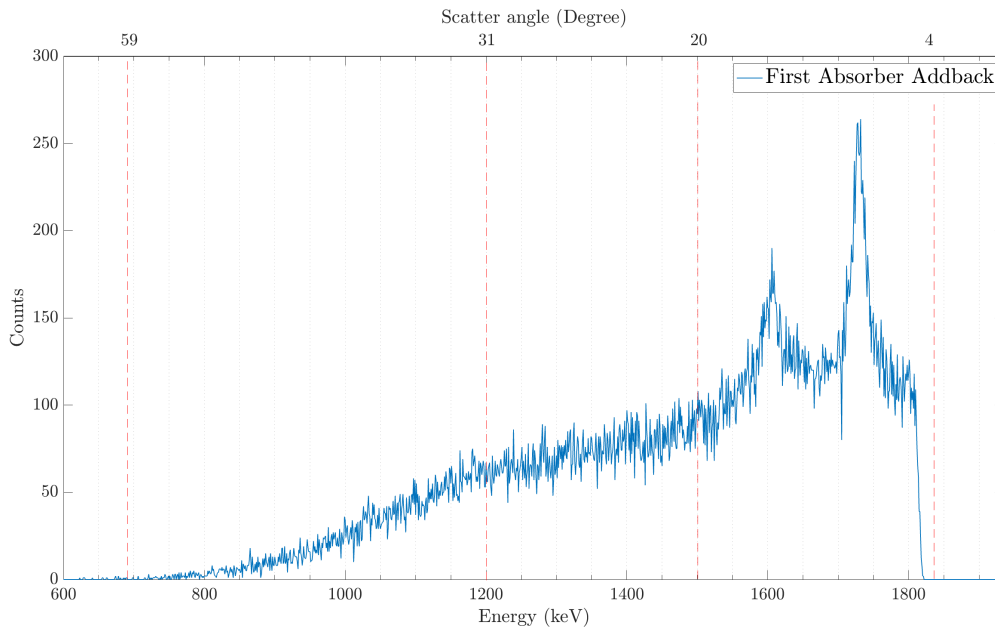


**Figure 5.2:** The deposited energy as a function of the Compton scattering angle for the first absorber of the gamma ray of 1.836 MeV and the corresponding calculated Compton scattering angles assuming a single scattering event. The red dash lines show the energy range used in Table 5.1

**Table 5.1:** The energy range deposited in the first absorber detector and the corresponding Compton scattering angles for 1.8 MeV gamma-rays. The number of events and percentage of total events is also shown.

| Deposited energy | Scattering angle | Number of events | % of total events |
|---|---|---|---|
| 670 keV to 1200 keV | 59° to 31° | 11413 | 15% |
| 1200 keV to 1500 keV | 31° to 21° | 22101 | 30% |
| 1500 keV to 1820 keV | 20° to 4° | 40319 | 55% |

The percentage of events observed within a range of the three energy windows and the corresponding Compton scattering angles is presented in Table 5.1. About 55% of the 1.8 MeV $\gamma$-rays experience a narrow scattering angle of 4° to 20° resulting in an energy deposition of 1.5 to 1.82 MeV. The angular scattering

distribution of 1.8 MeV gamma rays is calculated using the Klein-Nishina formula. This reveals that the 1.8 MeV gamma ray is much more inclined to exhibit a forward scatter angle than is the case with a lower energy $\gamma$-ray, such as 121 keV, as shown in Figure 5.3.
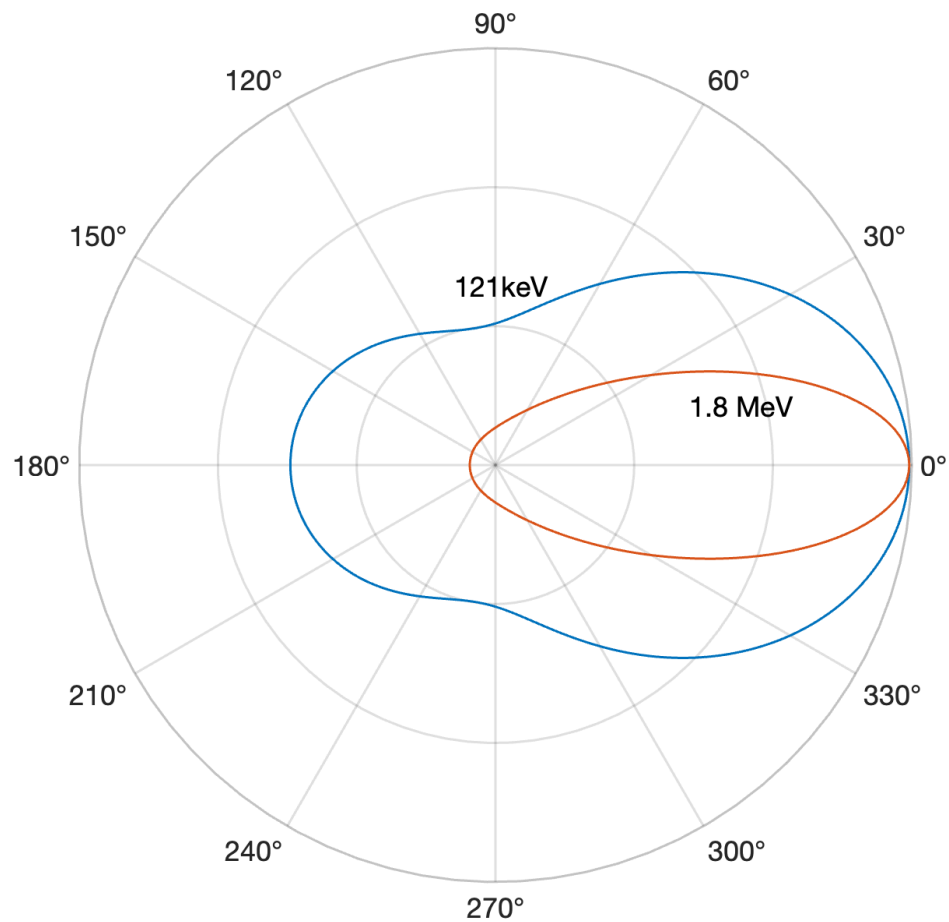


**Figure 5.3:** The angular distribution of the scattered gamma rays of 121 keV and 1.8 MeV using the Klein-Nishina formula for Z=32.
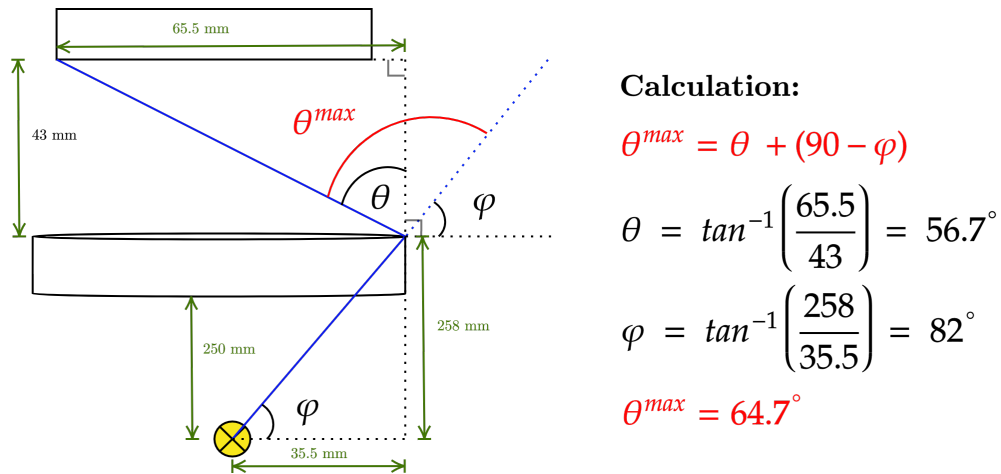
**Figure 5.4:** Schematic diagram of the geometry limit calculation. This calculation is for the gamma ray source that was placed 25 cm from the scatterer detector centrally in x and y, wherein the detectors were separated by 7 mm. The maximum possible scattering angle is 64.7°. The diagram is not drawn to scale.

The system geometry imposes a limit on the maximum possible scatter angle from an incident $\gamma$ at a known position. This limit was calculated for gamma rays of 1.836 MeV that are emitted isotropically from a source placed 25 cm from the scatterer detector centrally in x and y whilst the detectors were separated by 7 mm, as shown in Figure 5.4. The maximum possible scattering angle is calculated as 64.7° for single scattering events, which approximately agrees with the maximum scattering angle observed of 59°, as shown in Figure 5.2. Therefore, the maximum energy that can be deposited in the scatterer detector of the 1.8 MeV $\gamma$-ray is calculated as 1.23 MeV. The minimum energy deposited in the scatterer should be 4 keV because a low energy threshold has been used. Conversely, in the first absorber detector, the minimum and maximum possible energy can be deposited are calculated as 600 keV and 1.833 MeV, respectively. The calculated energy which can be deposited as a function of the Compton scattering angle for the scatterer detector and the first absorber for the gamma ray of 1.836 MeV is shown in Figure 5.5.
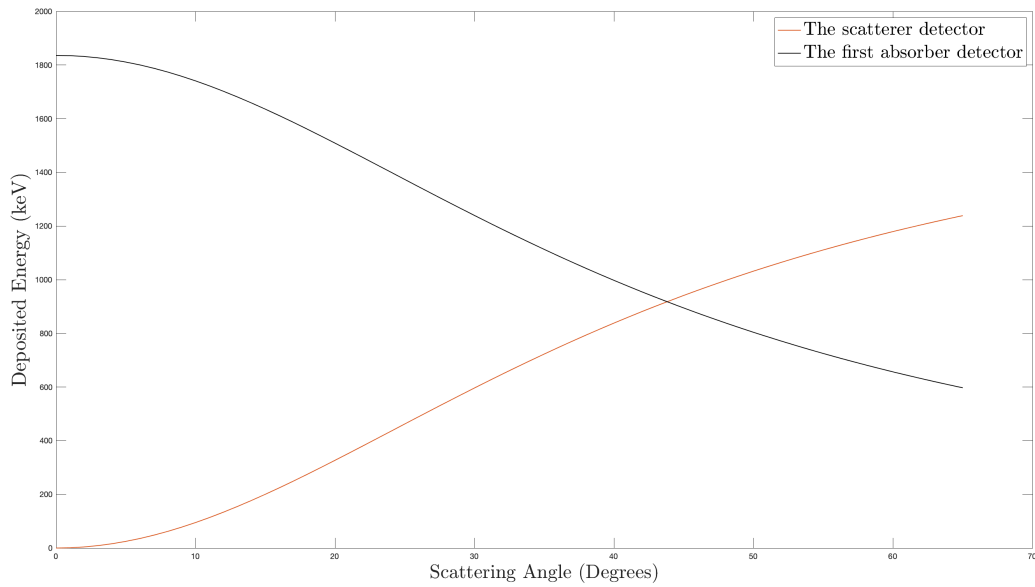
**Figure 5.5:** The calculated energy deposited as a function of Compton scattering angle for the scatterer detector and the first absorber for gamma ray of 1.836 MeV and the maximum possible scattering angle of 64.7°.

The measured deposited energy ranges were 4 keV - 1.18 MeV and 670 keV - 1.82 MeV for the scatterer and first absorber detectors, respectively. The calculated deposited energy ranges were 4 keV - 1.23 MeV and 600 keV - 1.833 MeV for the scatterer and first absorber detectors, respectively. The deposited energy ranges are within the geometry limit that was estimated using early calculations for the maximum possible deposited energy of 1.836 MeV. However, relatively small difference between the measured and calculated energy deposited in both detectors might be a result of the uncertainty introduced to the experiment from the measurement of the detector separation and the detector source distance in addition to the offset between the scatterer and the first absorber detectors.

Using this technique to optimize the geometrical setup (detectors separation) for measuring higher-energy $\gamma$-rays. It will also allow to optimize experimental parameters such as the D-DAQ setup and the dynamic range of the digitizer cards, which will discuss in Section 5.4. This technique is employed to predict the energy that is deposited in the scatterer and the first absorber detectors for the higher gamma energy, including the 4.4 MeV and 6.1 MeV $\gamma$-rays, during proton therapy, as shown in Figure 5.6.
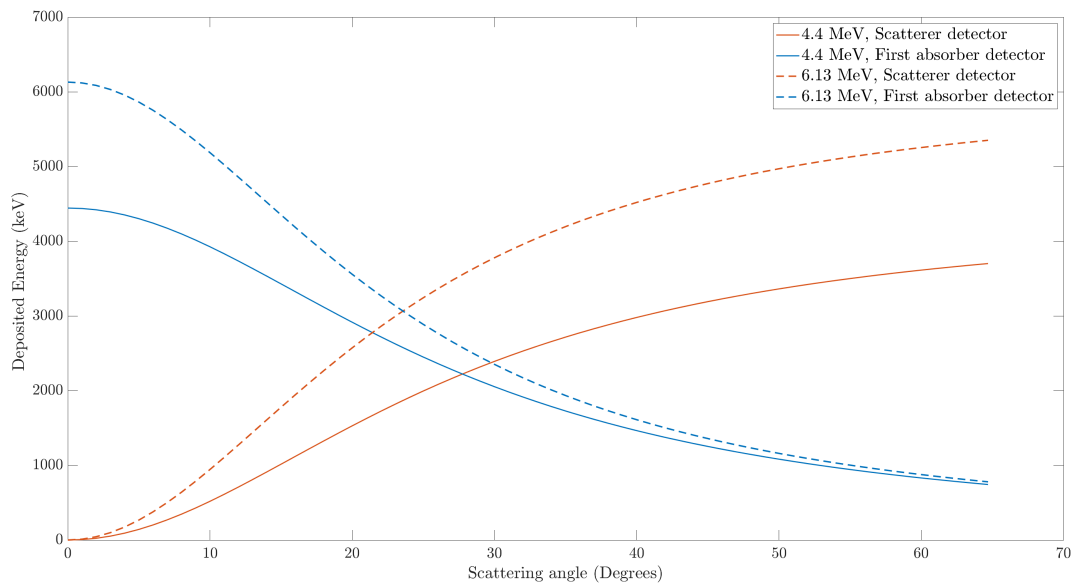
**Figure 5.6:** The calculated energy deposited as a function of Compton scattering angle for the scatterer detector and the first absorber for gamma ray of 4.4 MeV (line) and 6.13 MeV (dashed line). The maximum possible scattering angle is 64.7°.

For the 4.4 MeV $\gamma$-ray emitted 25 cm away from the scatterer detector, the possible energy range that can be deposited in the scatterer and the first absorber will be 4 keV - 3.7 MeV and 743 keV - 4.4 MeV, respectively. For the 6.13 MeV $\gamma$-ray originating 25 cm away from the scatterer detector, the possible energy range can be deposited in the scatterer and the first absorber will be 4 keV - 5.3 MeV and 780 keV - 6.1 MeV, respectively. These represent very challenging detection conditions. However, narrow scattering angle will be more probable, so that most energies in scetterer detector expected to be less 1 MeV. The remaining energy is expected to be split across the two absorber detectors.

## 5.2  An investigation of fold

Gamma rays can deposit their energy across the detector system in a variety of sequences, including both single and multiple scattering events. The gamma-ray energy, atomic number of the detector material, and thickness of the detector can all influence the interaction mechanisms of the gamma rays within the detectors. An exploration of the fold distribution for the individual detectors associated with the Gri+ system using the highest gamma-ray energy available can reveal valuable information related to the system setup in the proton beam therapy. Imaging high-energy $\gamma$-rays is challenging because the number of high fold events increases, which introduces complexity and uncertainty. Specifically, it is not possible to definitely order the interaction sequence correctly for image reconstruction,

assumptions based on underlying physics principles are used.

For low $\gamma$ energy, the fold distribution was investigated previously in Chapter 4 Section 4.2.3. Most of the events were Fold 1 within the scatterer and the first absorber detectors alongside the Gri+ system. For high $\gamma$ energy, approximately 86 % of the events were Fold 1 in the scatterer detector at $\gamma$ energy of 1.8 MeV, as shown in Figure 5.7. The scatterer detector was examined while the system operated in coincidence mode. This is achieved by applying an energy gate of 1.8 MeV to the total energy deposited in the system.
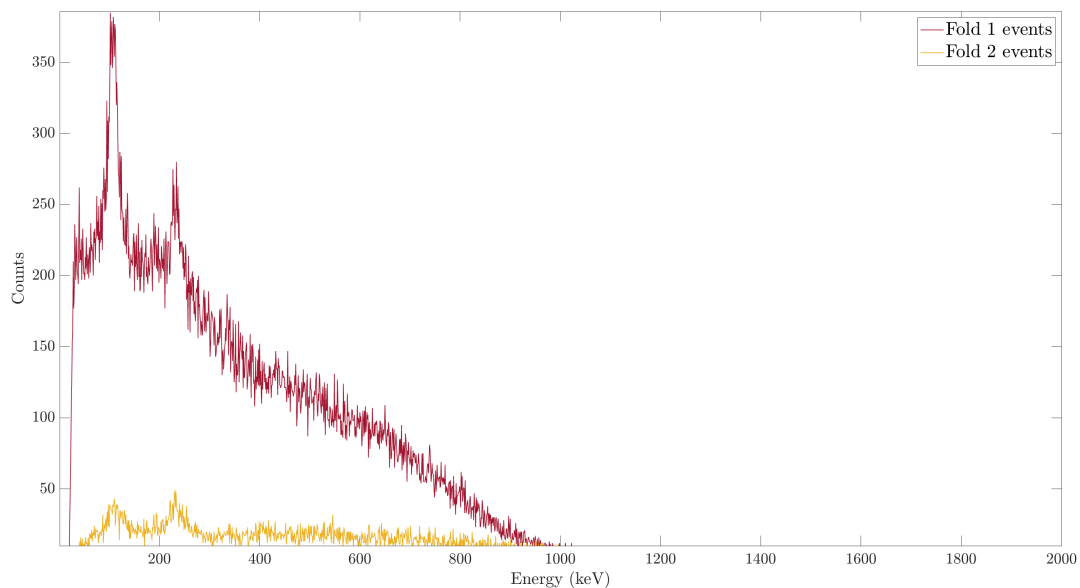


**Figure 5.7:** The DC addback energy spectra for the scatterer with an energy gate on the total energy of 1.8 MeV deposited in the system. Fold 1 and Fold 2 gates were applied and the Gri+ system was operated in a coincidence mode.

Using Fold 2 events from the scatterer detector in the imaging would introduce a large error in the reconstructed image. The Compton image is created by determining the cone apex angle and cone axis. In the case of the Fold 2 event in the scatterer detector, the user must decide the order of these two interactions and the precise vector between them. A large offset between the actual source position and the projection of the Compton cone would result from the error in the decision of the two interactions' order. However, in the first absorber, the error resulting from the order of the two interactions would be a much smaller deviation [61]. Hence, all further analysis for the fold distribution and the Compton imaging resolution will only use the Fold 1 event in the scatterer detector.

This section explores the fold distribution for 1.8 MeV gamma-rays for the first absorber detector alongside the Gri+ system, which will indicate if high fold events should be included in the final imaging code at high $\gamma$ energies or if the

uncertainties introduced by using high fold absorber events degrade the image too much. To this end, an $^{88}$Y point source with a 25 cm standoff was used. An energy gate on the 1.8 MeV gamma-ray was applied. The fold distribution at $\gamma$ energy of 121 keV was investigated previously in Chapter 4 Section 4.2.3 and shown here for comparison. In the first absorber fold distribution, the system was operating in single mode, while the system was operating in coincidence mode for analysis of the Gri+ system fold distribution.

## 5.2.1 First Absorber
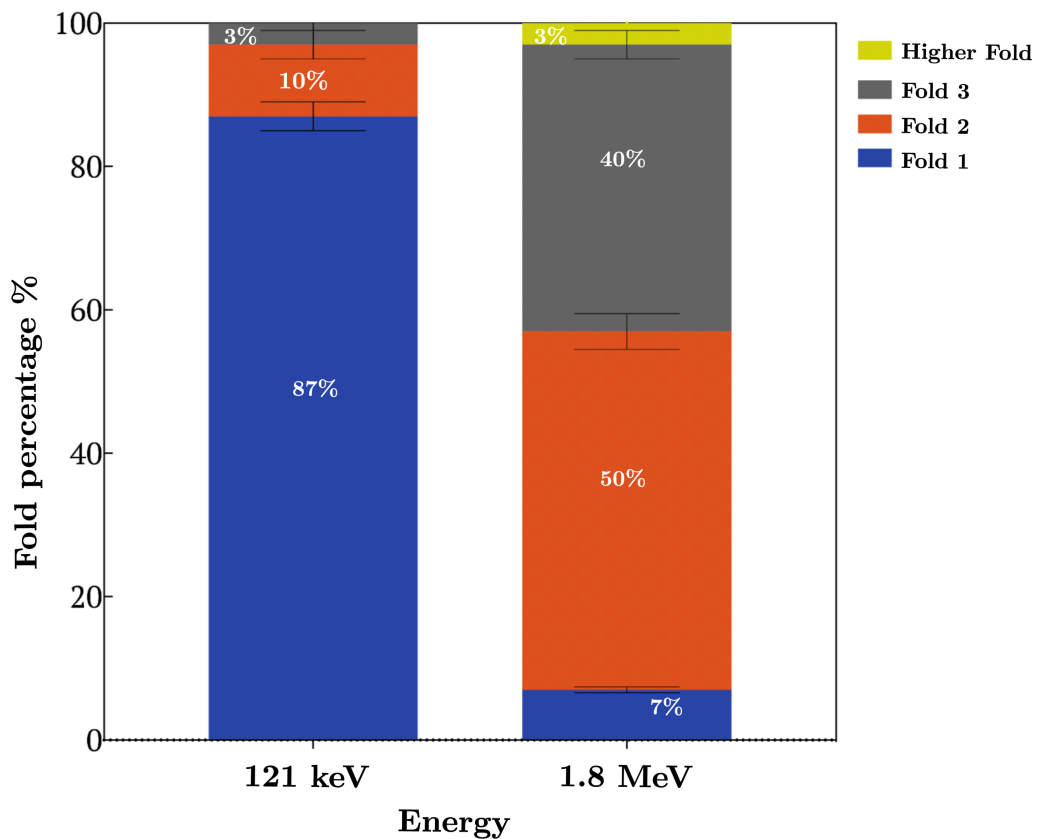


**Figure 5.8:** The fold distribution of the first absorber detector for the gamma ray energy of 121 keV and 1.8 MeV, wherein the system is operated in a single mode.

The first absorber detector fold distribution has a variety of event classifications, as shown in Figure 5.8. Approximately 87 % of the events were Fold 1 at a low gamma energy of 121 keV. However, 7 % of the events were Fold 1 at 1.8 MeV. Only about 10 % of the events were classified as Fold 2 at a gamma energy of 121 keV in comparison to approximately 50 % of the events classified as Fold 2 events at a gamma energy of 1.8 MeV. The Fold 3 events of 3 % and 40 % were categorised at gamma energies of 121 keV and 1.8 MeV, respectively. These results indicate that

significant amounts of the events were categorised as Fold 2 and Fold 3 events at 1.8 MeV (90%) compared to the fold distribution at 121 keV (13%). These results confirm early evaluations in this thesis (see Chapter 4 Section 4.2.3) for the range of gamma energy up to 1.4 MeV, wherein the fold level was concluded when the first absorber revealed dependence on the energy of the incoming gamma ray.

### 5.2.2 Gri+ system

The current fold investigation has revealed that approximately 86 % of the events were Fold 1 events in respect of the scatterer detector for $\gamma$ energy of 1.8 MeV. In addition, using Fold 2 events from the scatterer detector in the imaging would introduce a large error in the reconstructed image. Therefore, the system fold distribution analysis will only use the Fold 1 event in the scatterer detector. Both 2-tier and 3-tier event type were used with the fold analysis for the segmented absorber detector.
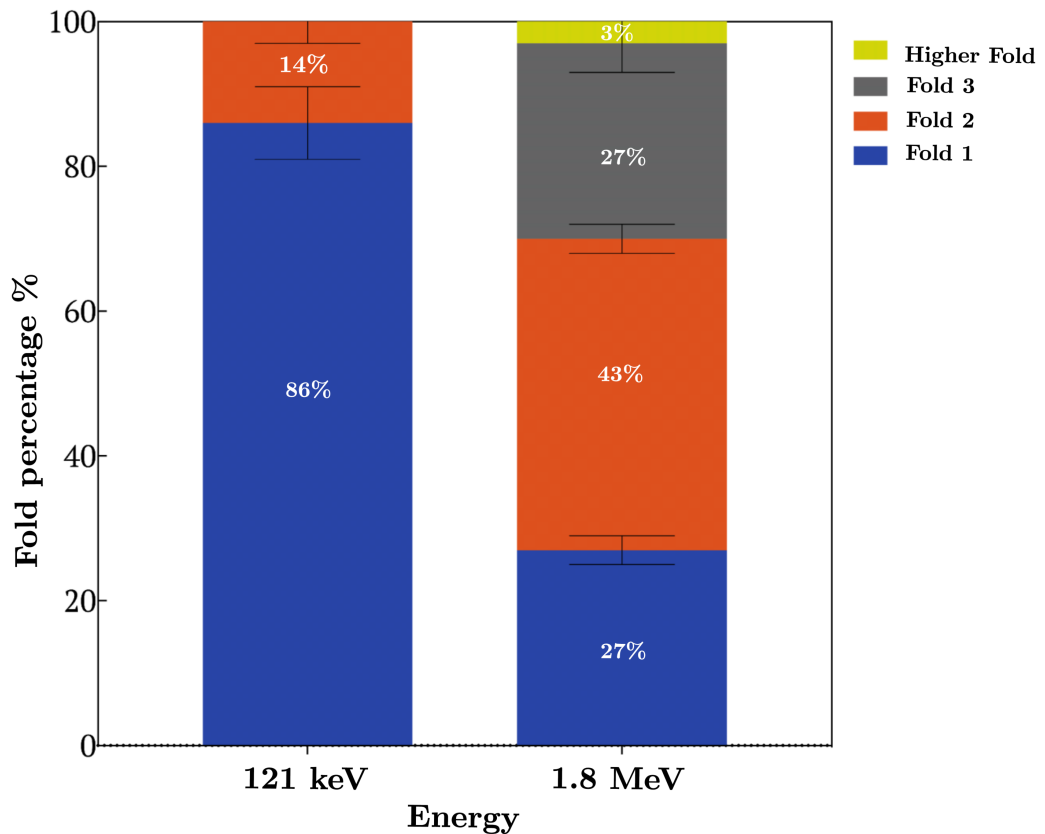


**Figure 5.9:** The fold distribution of the Gri+ system for the gamma ray energy of 121 keV and 1.8 MeV. The Gri+ system was operated in the coincidence mode and only the event categorized as Fold 1 in the scatterer detector was employed.

Figure 5.9 shows the fold distribution of the Gri+ system for gamma ray energy of 121 keV and 1.8 MeV. The Fold 1 events decrease in accordance with the increase

in the gamma-ray energy from 86 % to 27 % at gamma energy of 121 keV and 1.8 MeV, respectively. However, the Fold 2 events increase with increases in the gamma-ray energy from 14 % to 43 % at the gamma energy of 121 keV and 1.8 MeV, respectively. In addition, the Fold 3 and Higher Fold were only present at the higher gamma energy of 1.8 MeV as 27 % and 3 %, respectively. This result confirm the expectation that the fold level increases with increases in the incoming gamma-ray energy. This is because it is more likely that low energy gamma rays experience a Compton scattering in the scatterer detector and then photoelectric absorption in the first absorber detector, which are categorised as Fold 1 events, whilst, high energy gamma rays are more likely to experience multiple Compton scattering in the first absorber. Table 5.2 provides a detailed Fold 1 and Fold 2 distribution for the Gri+ system at 1.8 MeV. Only Fold 1 and Fold 2 events of the first absorber detector are used in the imaging evaluation in next section.

**Table 5.2:** The breakdown of the events folds for the Gri+ system at 1.8 MeV. The Gri+ system was operated in coincidence mode. The fold breakdown column represents the first absorber detector folds because only events categorized as Fold 1 in scatterer detector were used.

| Fold categories | Absorber Fold (AC, DC) | Number of events | % of events | Fold percentage |
|:---:|:---:|:---:|:---:|:---:|
| **Fold 1** | Fold [1,1] | 31517 | 27% | 27% |
| **Fold 2** | Fold [1,2] | 10372 | 9% | 43% |
| | Fold [2,1] | 12617 | 11% | |
| | Fold [2,2] | 27865 | 24% | |
| **Fold 3** | | 32474 | 27% | |
| **Higher Fold** | | 3634 | 3% | |
| **Total** | | 118479 | 100% | |

## 5.3 Gri+ Image resolution

The largest proportion of events (43%) were classified as Fold 2 events at 1.8 MeV, with the fold level tending to increase with the energy of the gamma-ray increasing. The energy of prompt gamma-rays emitted during proton therapy are 4.4 MeV and 6.13 MeV, therefore, the events detected in Gri+ during proton therapy are expected to be dominated by Fold 2 and Fold 3. To evaluate the impact of utilising these high fold events in imaging prompt $\gamma$'s, it is essential to evaluate the Gri+ image resolution using the highest gamma-ray energy available in the lab and therefore the highest fold event-level possible. It is hypothesised that using higher fold events introduce additional position uncertainties that could degrade the image but improve statistics, giving a compromise.

The image resolution comparison analyses used two pulse shape analysis al-

gorithms to sort the data and two image reconstruction codes used where it was appropriate. This comparison is to study the image resolution across different Fold categories. The two pulse shape analysis algorithms used for sorting were the Parametric PSA, for online analysis, and the Database PSA, for offline analysis. These algorithms were thus used to improve the determination of gamma interaction position within the detectors and therefore have different position uncertainties contributing to the overall image quality (see Chapter 4, Section 4.2.5).

Two different image reconstruction codes are available for Compton imaging at the University of Liverpool (UoL), an analytical and an iterative code (Maximum Likelihood Expectation Maximisation, MLEM). The analytical reconstruction code uses back-projected cones in the scatterer detector, which are then projected outwards onto slices across the x-y plane. Each cone's geometry is calculated prior to conic sampling that discretises them according to the number of points per angular degree. In contrast, the iterative code (MLEM) projects cones into an imaging volume and increments each intersecting array element. The first stage of this results in a similar image to that produced by analytical code, while further iterations calculate each cone's weight by forward-projecting it through the image volume. A probability matrix is then determined by back projecting the weighted cones through an empty imaging volume. Both codes have been evaluated previously by [61] with respect to processing time and image quality for both point and extended sources. The MLEM code can achieve better image quality but with long processing times. The analytical code has shorter processing times. However, the image quality of the analytical code is only comparable to the first iteration of the MLEM code. It is likely that the analytic code is used for real time imaging and iterative code for post processing of the data.

The imaging resolution was thus evaluated as a function of the increase in Fold level. As noted, only Fold 1 events in the scatterer detector were used in the final work. It is the first absorber detector folds that determine the Gri+ system fold categories in this discussion. The image resolution of Fold 1 and Fold 2 types, which are Fold [2,1 and 1,2] and Fold [2,2] events, were evaluated by imaging them separately and together.

Table 5.3 outlines the numbers of each imageable events across the relevant Fold categories as relative percentages of total imageable events. The total number of imageable events was 82371, with 38 % of these events classified as Fold 1 types, leaving 62 % of imageable events as Fold 2 types. This can be further broken down into to 28 % Fold [2,1 and 1,2] and 34 % Fold [2,2] types.

An analytical reconstruction code was used to evaluate the image resolution across different fold categories and to compare image resolution between the ap-

**Table 5.3:** The breakdown of the imageable events folds for the Gri+ system at 1.8 MeV. The Gri+ system was operated in coincidence mode for these tests. The fold breakdown column represents the first absorber detector folds only, as only the event categorised as Fold 1 in the scatterer detector was used in each case.

| Fold categories | Absorber Fold (AC, DC) | Number of events | Fold percentage | |
|---|---|---|---|---|
| Fold 1 | Fold [1,1] | 31517 | 38% | |
| | Fold [1,2] | 10372 | 13% | |
| Fold2 | Fold [2,1] | 12617 | 15% | 62% |
| | Fold [2,2] | 27865 | 34% | |
| All imageable Fold | | 82371 | 100% | |

plications of Parametric PSA and Database PSA algorithms. The same number of events (22984) were used for each fold category to remove any differences that arise due to statistical uncertainties. The data was sorted online using the Parametric PSA algorithm within MTsort, while the database PSA algorithm was applied offline using MATLAB.

Image resolution was quantified as the FWHM of the reconstructed image as calculated by distribution fitting over the pixel with the maximum number of Compton overlaps in both the x and y-axes, as measured in mm, in addition to the x and y-axis angular resolutions.

## 5.3.1 Online analysis

The best image resolution achieved using the Parametric PSA algorithm was 26.2 $\pm$ 0.2 mm for Fold 1. Folds [2,1 and 1,2] image resolution was 48.8 $\pm$ 1.1 mm which is a huge degradation in image resolution of 22.6 mm. A further degradation of Fold [2,2] image resolution to be 51 $\pm$ 1.9 mm. Fold 2 [all types] image resolution brought the overall Fold 2 image resolution to 50.6 $\pm$ 1.3 mm which degrade the image resolution by 93 % compared to the Fold 1 image resolution.

The image resolution was 37.7 $\pm$ 1.2 mm for all Fold events, which is a degradation of the image resolution by by 44 % as compared to the Fold 1 image resolution. The large degradation in the image resolution seen for Fold 2 is mainly due to the large uncertainty introduced with regard to position resolution. This uncertainty arises from the predefined X-Y and Z positions for Fold 2 event in the first absorber, at 2.5 mm and 10 mm, respectively, and from the way that the Parametric PSA algorithm decides the event order for Fold 2 events. However, the image resolution degradation is reduced when all Fold events are imaged due to including the uncertainties of the Fold 1 and Fold 2 events. In this comparison, the same number of events were used in each fold category, and they were equal

contributions to all Folds type. It might be because the equal contribution of different folds categories to the all Folds type results in image resolution value in the midway of the value of Fold 1 and Fold 2.

Table 5.4 shows the details of FWHM and angular resolution achieved when using the analytical reconstruction code with online analysis to process events from the different Fold categories. The Fold 1, Folds [2,1 and 1,2], Folds [2,2], and all Folds images using the online analysis are shown in Figure 5.10, and corresponding slice fits are shown in Figure 5.11.

**Table 5.4:** The imageable event breakdown of the folds for the Gri+ system at 1.8 MeV. The Gri+ system was operated in coincidence mode. The fold breakdown column represents the first absorber detector folds only, as only events categorised as Fold 1 in the scatterer detector were used. The analytical reconstruction code was used with online analysis and applied with respect to all different Fold categories.

| Fold type | (mm) | | (Degrees) | |
| --- | --- | --- | --- | --- |
| | x FWHM | y FWHM | x FWHM | y FWHM |
| F1 | $26.2 \pm 02$ | $26 \pm 0.2$ | $6 \pm 0.1$ | $6 \pm 0.1$ |
| F[1,2]&[2,1] | $48.8 \pm 1.1$ | $59.3 \pm 1.4$ | $11.1 \pm 0.3$ | $13.5 \pm 0.3$ |
| F[2,2] | $51 \pm 1.9$ | $62.2 \pm 2.4$ | $11.7 \pm 0.4$ | $14.2 \pm 0.5$ |
| F2 | $50.6 \pm 1.3$ | $61.7 \pm 1.1$ | $11.6 \pm 0.5$ | $14.1 \pm 0.6$ |
| All Fold | $37.7 \pm 1.2$ | $40.7 \pm 2.3$ | $8.6 \pm 0.3$ | $9.3 \pm 0.5$ |

**(a)** Image of Fold 1 events.

**(b)** Image of Fold [1,2]&[2,1] events.

**(c)** Image of Fold [2,2] events.

**(d)** Image of all Fold events.
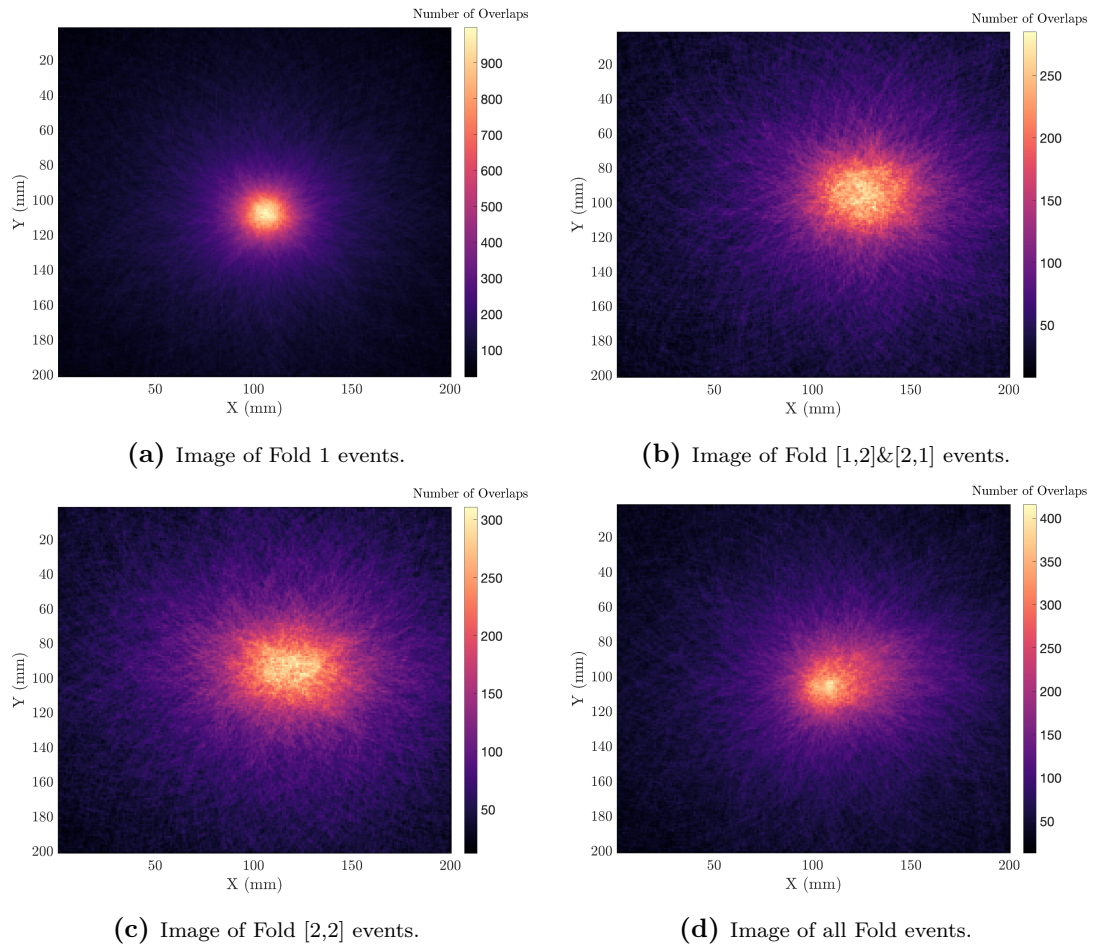
**Figure 5.10:** Images of **(a)** Fold 1, **(b)** Fold [1,2]&[2,1], **(c)** Fold [2,2], and **(d)** all Fold using online analysis. The image was reconstructed using analytical code. Note the scale is different for each, as it is normalised to the maximum count in the image.

**(a)** Slice fit for Fold 1 image.



**(b)** Slice fit for Fold [1,2]&[2,1] image.



**(c)** Slice fit for Fold [2,2] image.



**(d)** Slice fit for all Fold image.
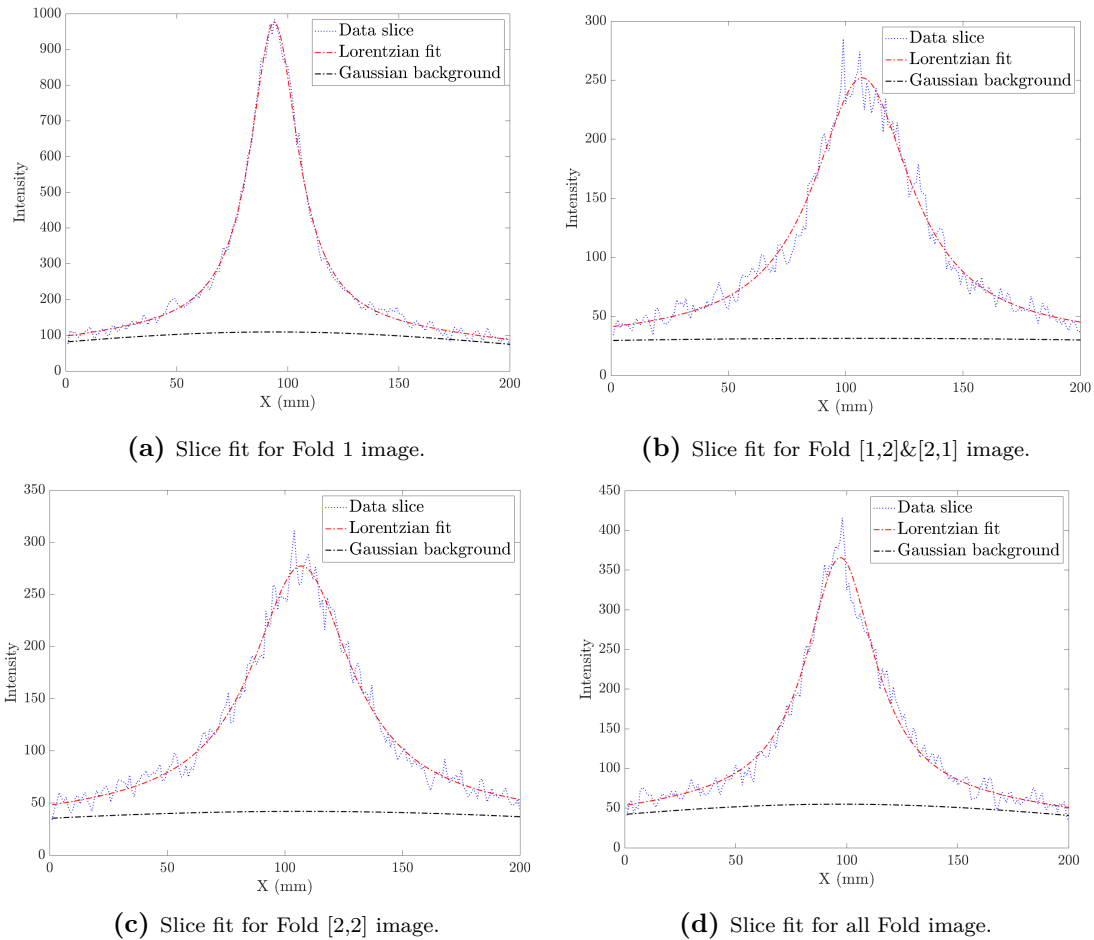
**Figure 5.11:** The corresponding slice fit for the reconstructed images of **(a)** Fold 1, **(b)** Fold [1,2]&[2,1], **(c)** Fold [2,2], and **(d)** all Fold using online analysis. The image was reconstructed using analytical code.

## 5.3.2 Offline analysis

The same events as used in Table 5.3 were reassessed using Database PSA algorithms. In this case, 24.2 ± 0.2 mm was the best image resolution, for Fold 1. Folds [2,1 and 1,2] image resolution was 28.9 ± 0.4 mm which is degradation in image resolution of 4.7 mm (19%). A further degradation for Fold [2,2] image resolution to be 29.5 ± 0.5 mm. Fold 2 [all types] image resolution brought the overall Fold 2 image resolution to 29.4 ± 0.7 mm which is degradation of the image resolution by 22 % compared to the Fold 1 image resolution. The image resolution was 26.5 ± 0.4 mm for all Fold events which is degradation of the image resolution by 10 % as compared to the Fold 1 image resolution. The degradation in the image resolution for Fold 2 is due to the uncertainty introduced with respect to the position resolution when the algorithm decides the event interaction order for Fold 2. Further detail of FWHM and angular resolution using the analytical

reconstruction code with database PSA as applied to different Fold categories is shown in Table 5.5. The Fold 1, Folds [2,1 and 1,2], Folds [2,2], and all Folds images using the offline analysis are shown in Figure 5.12, and corresponding slice fits are shown in Figure 5.13.

**Table 5.5:** The imageable event breakdown of the folds for the Gri+ system at 1.8 MeV. The Gri+ system was operated in coincidence mode. The fold breakdown column represents the first absorber detector folds only, as only events categorised as Fold 1 in the scatterer detector were used. The analytical reconstruction code used with offline analysis was thus applied to all different Fold categories.

| Fold type | (mm) | | (Degrees) | |
|:---:|:---:|:---:|:---:|:---:|
| | x FWHM | y FWHM | x FWHM | y FWHM |
| F1 | 24.2+0.2 | 25.8 ± 0.2 | 5.5 ± 0.1 | 5.9 ± 0.1 |
| F[1,2]&[2,1] | 28.9 ± 0.4 | 28.6 ± 0.4 | 6.6 ± 0.1 | 6.5 ± 0.1 |
| F[2,2] | 29.5 ± 0.5 | 29.3 ± 0.6 | 6.8 ± 0.1 | 6.8 ± 0.1 |
| F2 | 29.4 ± 0.7 | 29 ± 0.6 | 6.7 ± 0.2 | 6.7 ± 0.1 |
| All Fold | 26.5 ± 0.4 | 26.4 ± 0.5 | 6.1 ± 0.1 | 6 ± 0.1 |

**(a)** Image of Fold 1 events.



**(b)** Image of Fold [1,2]&[2,1] events.



**(c)** Image of Fold [2,2] events.



**(d)** Image of all Folds events.
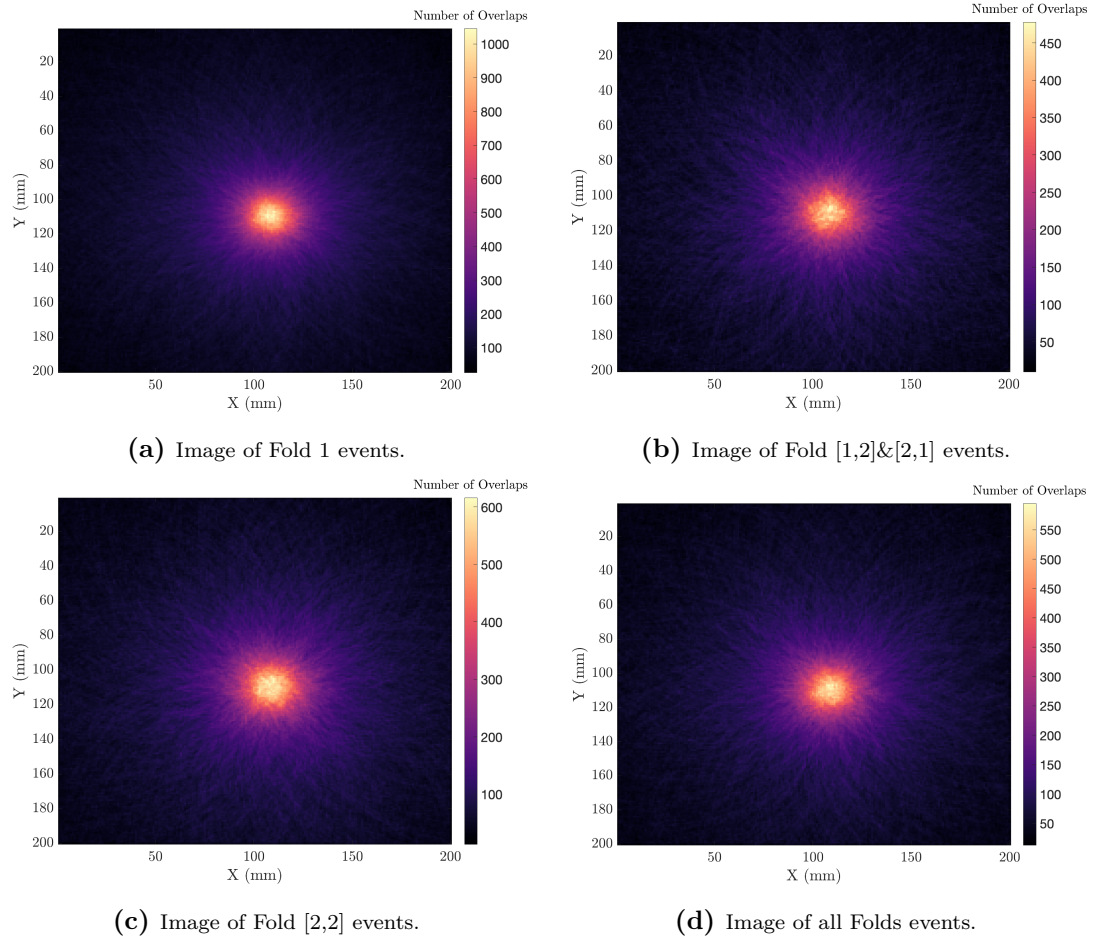
**Figure 5.12:** Images of **(a)** Fold 1, **(b)** Fold [1,2]&[2,1], **(c)** Fold [2,2], and **(d)** all Fold using offline analysis. The image was reconstructed using analytical code. Note the scale is different for each, as it is normalised to the maximum count in the image.
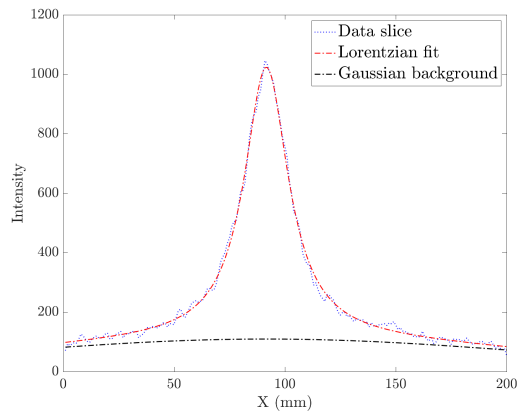
**(a)** Slice fit for Fold 1 image.
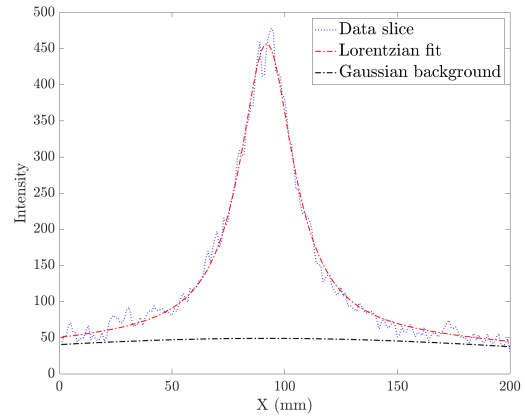


**(b)** Slice fit for Fold [1,2]&[2,1] image.
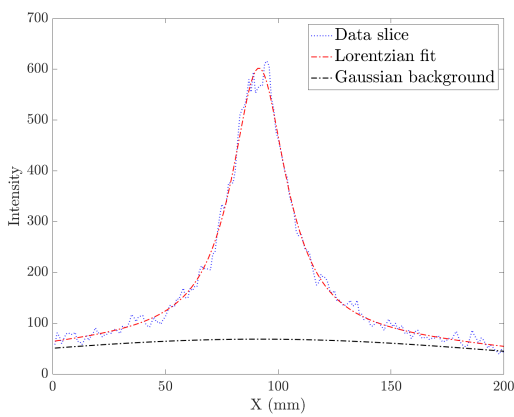


**(c)** Slice fit for Fold [2,2] image.
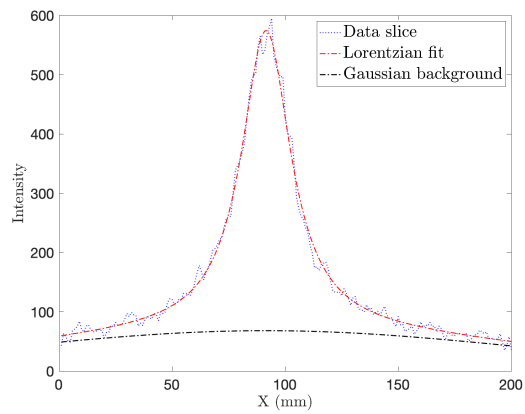


**(d)** Slice fit for all Folds image.

**Figure 5.13:** The corresponding slice fit for the reconstructed images of **(a)** Fold 1, **(b)** Fold [1,2]&[2,1], **(c)** Fold [2,2], and **(d)** all Fold using offline analysis. The image was reconstructed using analytical code.

### 5.3.3 Online analysis vs offline analysis
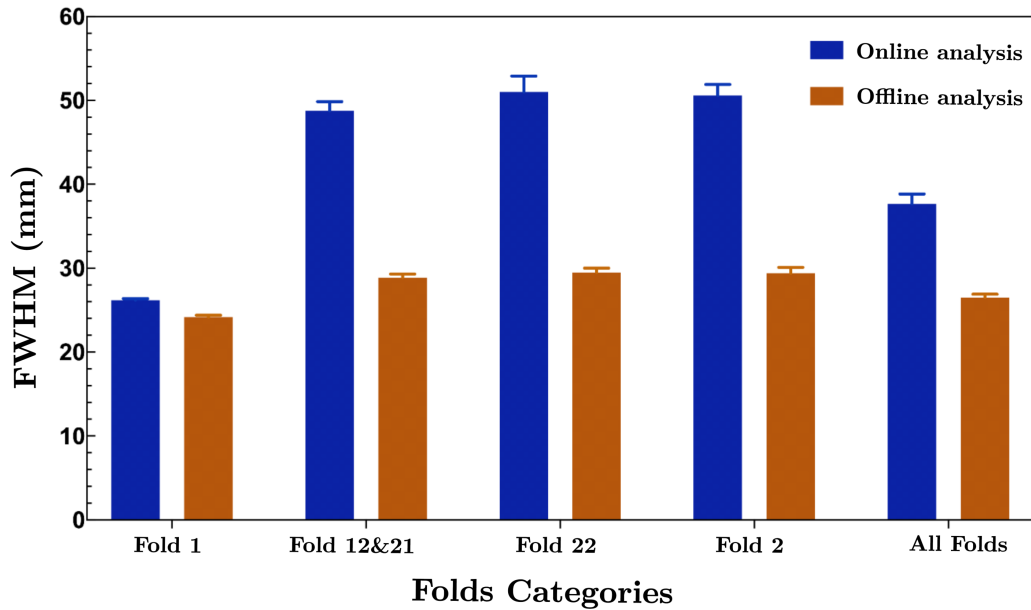


**Figure 5.14:** Image resolution comparison between online and offline analysis across various Fold categories using the analytical reconstruction code.

Figure 5.14 shows the change in image resolution, as FWHM in mm, for both online and offline analysis as the Fold level increases. Both algorithms show degradation in image resolution as a function of fold level, though offline analysis demonstrates superior image resolution across all Fold categories. A small degradation in image resolution occurred between online and offline analysis, at around 2 mm for Fold 1 events as shown in Figure 5.15. However, more significant degradation in the image resolution, by 21.2 mm and 11.2 mm, occurred for Fold 2 and all Fold events, respectively, as shown in Figure 5.16.

**(a)** Image of Fold 1 events using online analysis.



**(b)** Slice fit for Fold 1 image using online analysis



**(c)** Image of Fold 1 events using offline analysis.



**(d)** Slice fit for Fold 1 image using offline analysis.
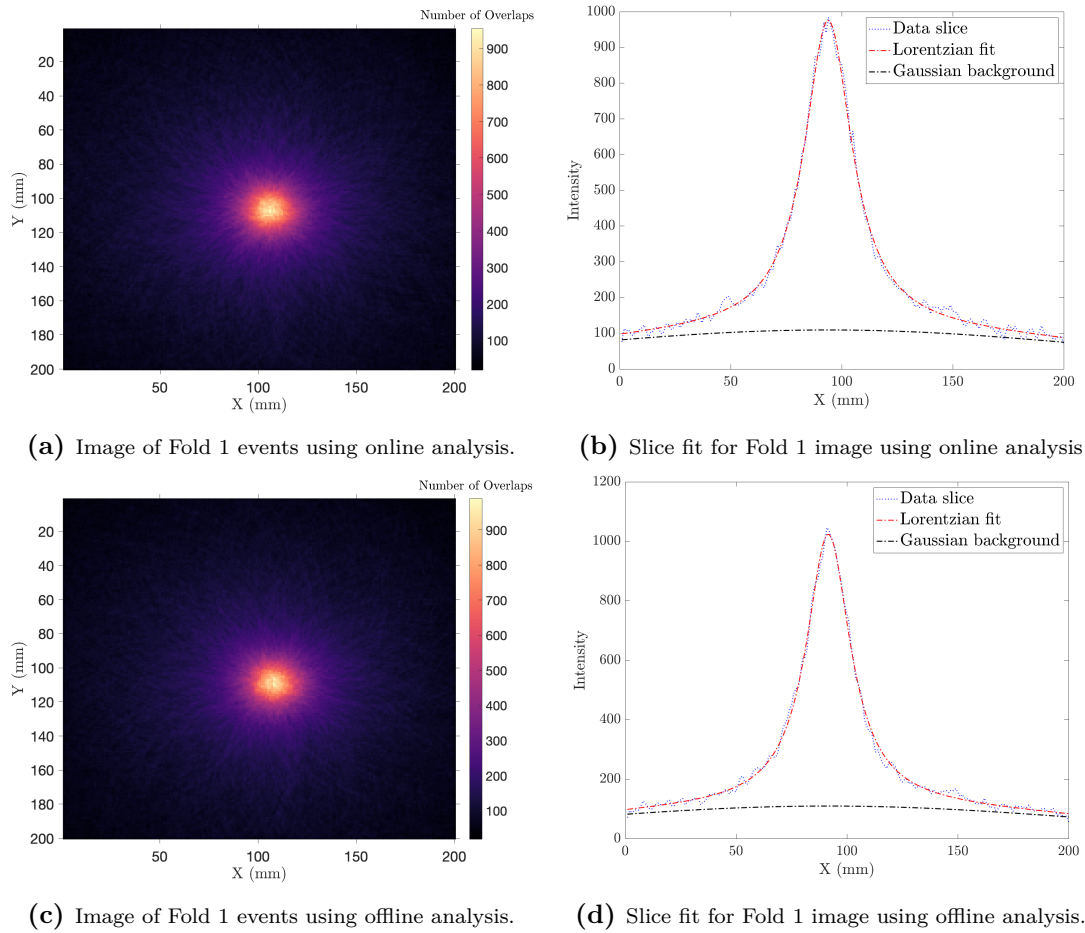
**Figure 5.15:** Images of Fold 1 events for (a) online analysis, (b) the corresponding slice fit, (c) offline analysis, and (d) the corresponding slice fit using analytical reconstruction code.

**(a)** Image of Fold 2 [all types] events using online analysis.



**(b)** Slice fit for Fold 2 [all types] image using online analysis



**(c)** Image of Fold 2 [all types] events using offline analysis.



**(d)** Slice fit for Fold 2 [all types] image using offline analysis.
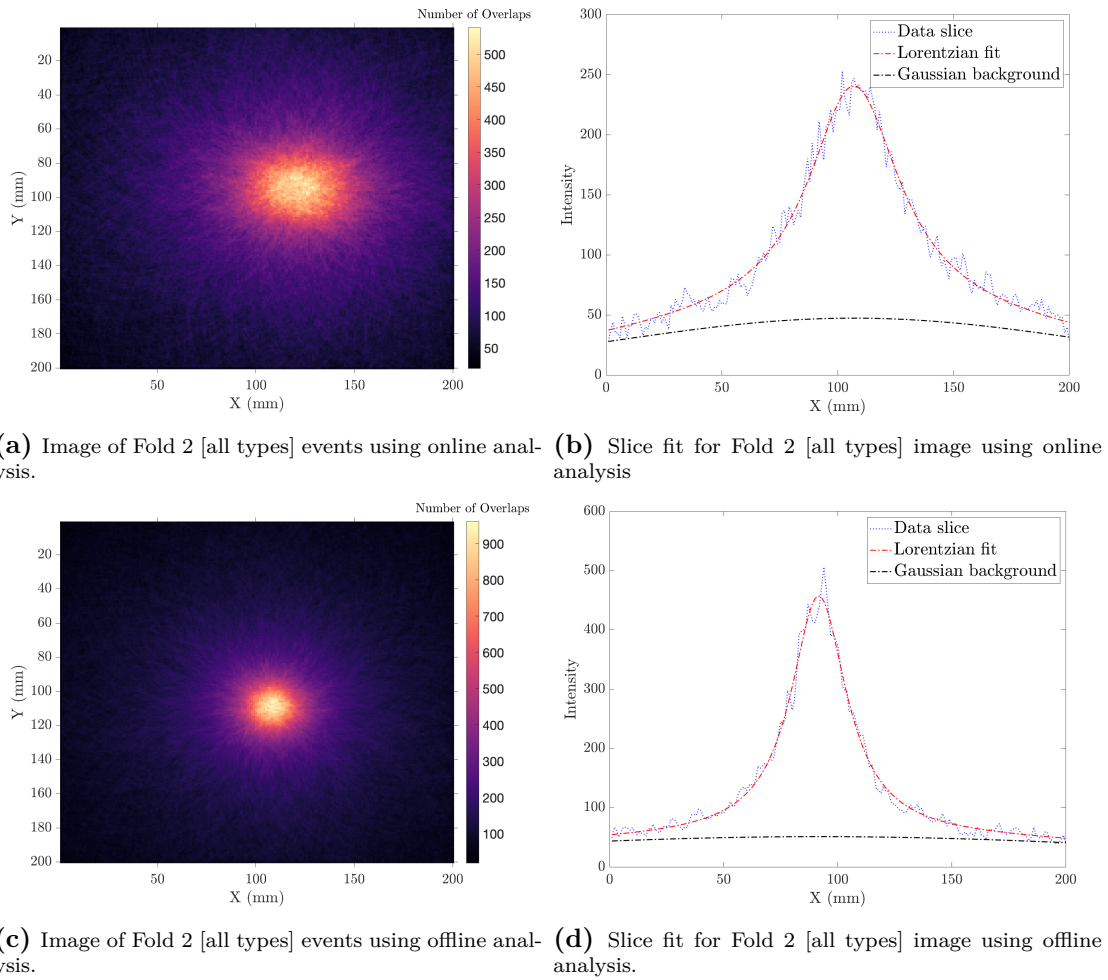
**Figure 5.16:** Images of Fold 2 [all types] events for (a) online analysis, (b) the corresponding slice fit, (c) offline analysis, and (d) the corresponding slice fit using analytical reconstruction code.

These results suggest that imaging Fold 2 events will degrade the system image resolution by 11.5 mm and 2.3 mm using online and offline analysis, respectively. However, it does significantly increase the Gri+ system imaging efficiency from 27% to 70% of all events registers in the system at 1.8 MeV gamma energy. The superior image resolution offered by offline analysis over the online analysis for different Fold categories may be advantageous. However, using offline analysis does increase computational costs as well as extending the time required to perform this analysis, as online analysis can be performed at the same time data is recorded and sorted. A recent detailed assessment by [52] evaluated the time and computational costs for the offline analysis, identifying processing times for 1,000 Fold 1, Fold [2,1 and 1,2], and Fold [2,2] events as 95, 490, and 690 seconds, respectively. Computational costs and time limitations are thus potential limitations to implementing the offline analysis in clinical situations unless acceleration methods

are employed such as GPU.

## 5.3.4   The optimum image resolution

To determine the best possible image resolution from the system, data were acquired for an $^{88}$Y point source with a 25 cm standoff and the 1.8 MeV $\gamma$-ray imaged with the iterative code (MLEM). The user can define the number of iterations for the code such that the first stage results in a similar image to that expected in the analytical code. However, further iterations calculate each cone's weight by forward-projecting it through the image volume which result in better image quality. Figure 5.17 shows the images of 1.8 MeV emitted from an $^{88}$Y point source at 25 cm standoff using the iterative code with 5, 10, 15, and 20 iterations using online analysis for a Fold 1 event data set.



**(a)** Iterations number = 5.

**(b)** Iterations number = 10.

**(c)** Iterations number = 15.

**(d)** Iterations number = 20.
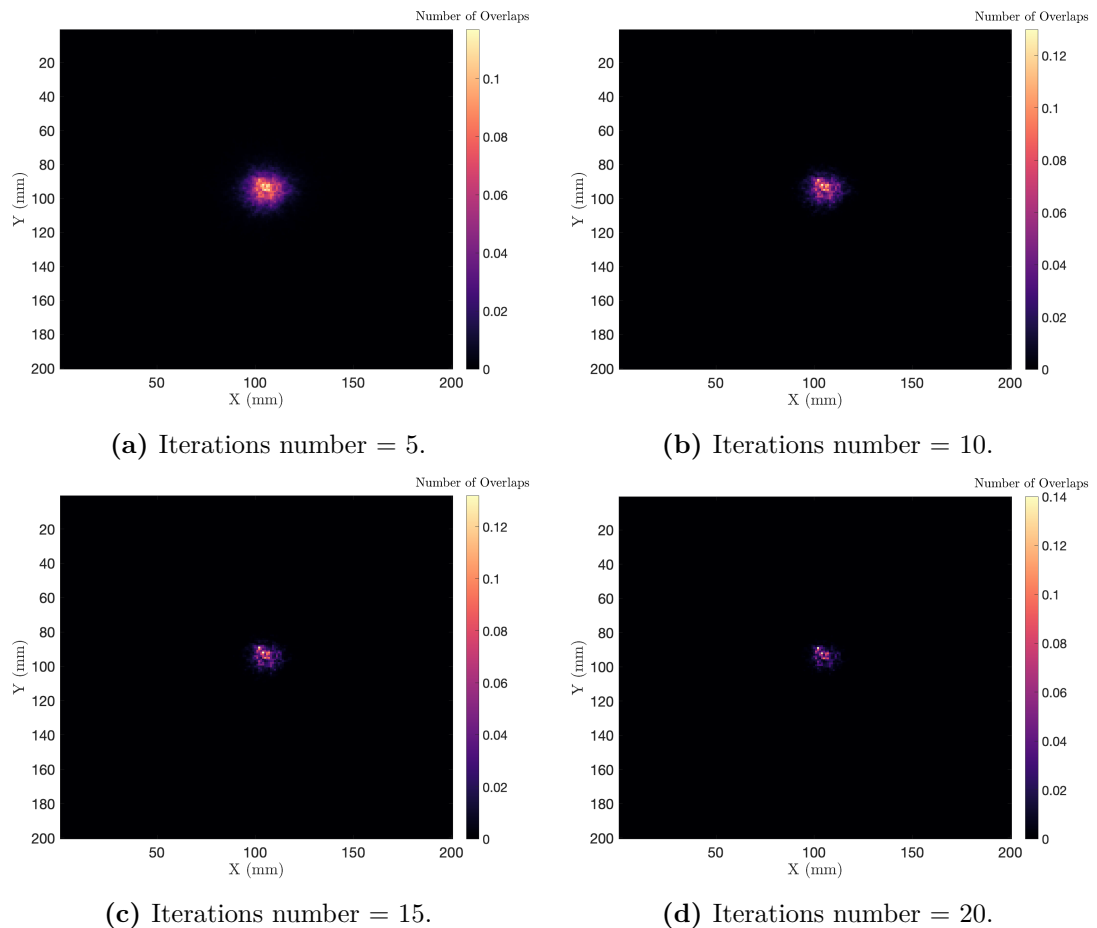
**Figure 5.17:** Reconstructed images of 1.8 MeV from an $^{88}$Y point source at 25 cm standoff using MLEM reconstruction code with (a) 5, (b) 10, (c) 15, and (d) 20 iterations using online analysis for Fold 1 events.

To determine the best number of iterations to use in imaging, the FWHM over the range of iterations can be calculated. The FWHM of the reconstructed image

is calculated by distribution fitting over the slice with the maximum number of Compton overlaps. Due to the change in the slice shape as function of iteration number, different fitting functions were used over the range of iterations to achive the optimum fit: from 0 (first stage image) to 2 iterations, the fitting function was a Lorentzian peak on a Gaussian background, while from 3 to 20 iterations, the fitting function was a Gaussian peak due to the the background count were decrease as the number of iterations increase.
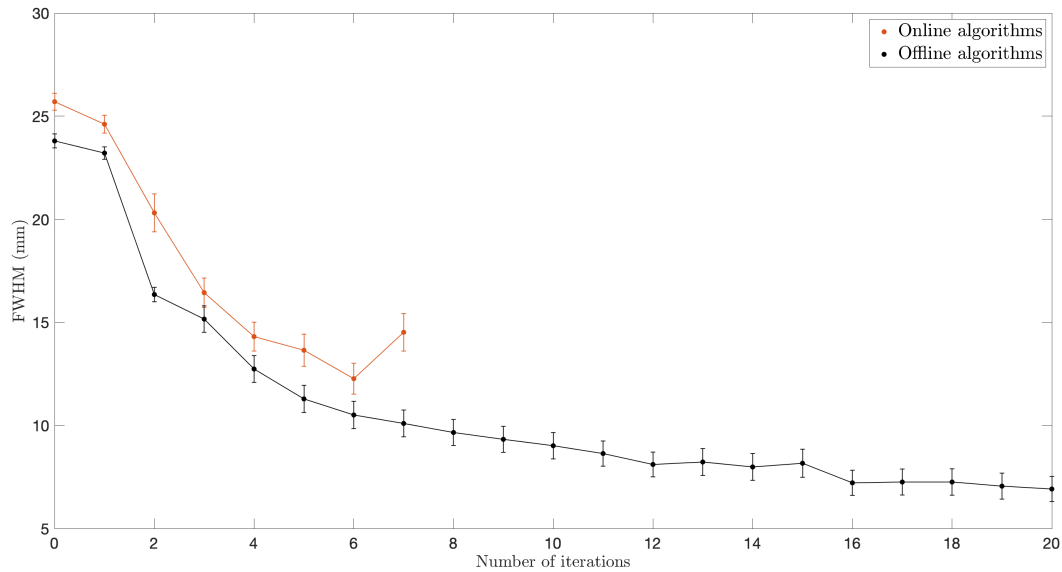


**Figure 5.18:** The FWHM over range of iterations for the online and offline analysis for Fold 1 events.

Figure 5.18 shows the FWHM as a function of the number of iterations in the MLEM code for the online and offline PSA analysis. For the online analysis, its demonstrates an improvement in FWHM as the number of iterations increases up to $6^{th}$ iteration. While at the $7^{th}$ iteration, the peak shape is split which indicating an over-iteration as shown in Figure 5.19. However, for offline analysis, a continuous improvement in FWHM as the number of iterations increases up to $16^{th}$ iteration after which it plateaus. Thus, for comparison reason, the $5^{th}$ iteration was selected for the online and the offline analysis. However, the $16^{th}$ iteration with the offline analysis will be used later to report the best achievable image resolution.
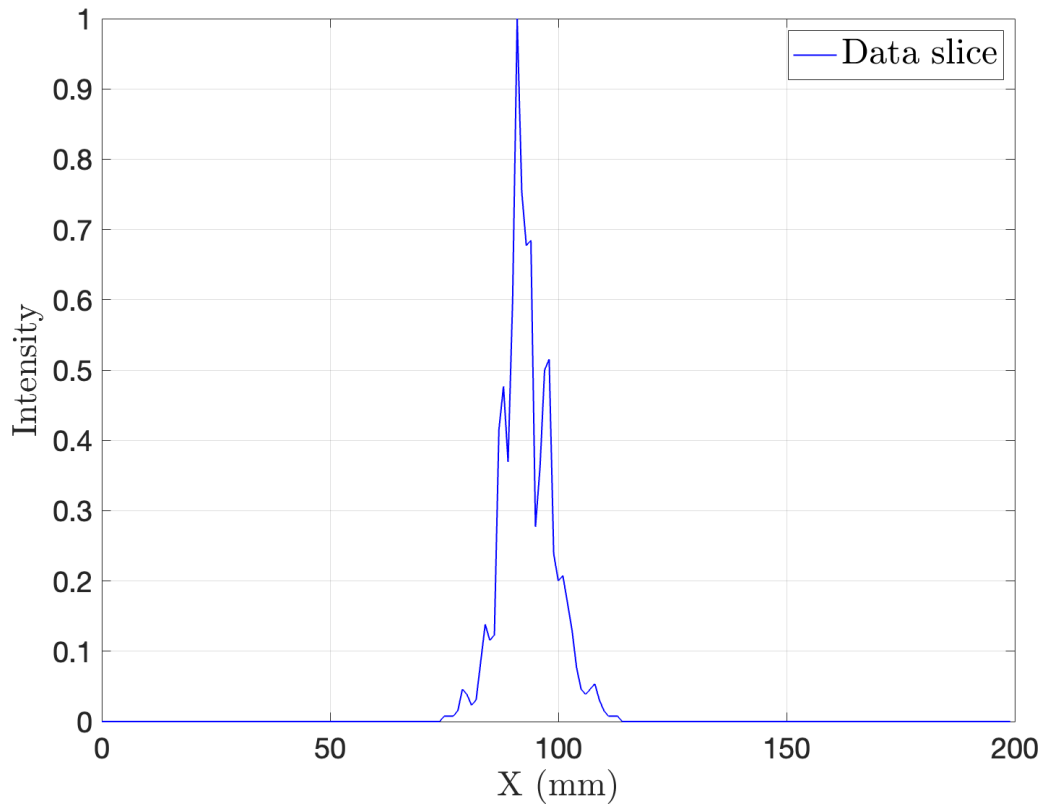
**Figure 5.19:** Slices from a reconstructed image using MLEM code and online analysis was applied. This show the split peak when used the $7^{th}$ iteration image.

The exact number of events and iterations were used to evaluate the system image resolution across different fold combinations for both online and offline analysis. The system image resolution using online and offline analysis for Fold 1 and all Folds events were reported in Table 5.6. For the offline analysis, the FWHM of $11.3 \pm 0.7$ mm and $15.9 \pm 0.7$ mm were achieved for Fold 1 and all Folds events, respectively. However, for the online analysis the FWHM of $13.6 \pm 0.8$ mm and $20.2 \pm 1$ mm were achieved for Fold 1 and all Folds events, respectively. This result shows the superior image resolution using offline algorithms across different Fold combinations.

**Table 5.6:** The Gri+ system image resolution using online and offline analysis for Fold 1 and all Fold events using MLEM reconstruction code. The $5^{th}$ iterations were used for the online and offline analysis.

|  | Online algorithm | Offline algorithm |
|---|---|---|
| **Fold 1** | $13.6 \pm 0.8$ | $11.3 \pm 0.7$ |
| **All Fold** | $20.2 \pm 1$ | $15.9 \pm 0.7$ |

It can also be seen that the Fold 1 images for online and offline analysis are

almost similar, with a slight difference in the number of overlaps, as shown in Figure 5.20. However, all Folds images demonstrates shape differences when using online analysis, as the image from the offline analysis perfectly represents the point source shape, as shown in Figure 5.21. The corresponding slice fit for previous reconstructed images are shown in Figure 5.22. It might be because including the Fold 2 events in the image introduces a large level of uncertainty in the position resolution, which has a further impact when using online analysis as discussed in Section 5.3.1.
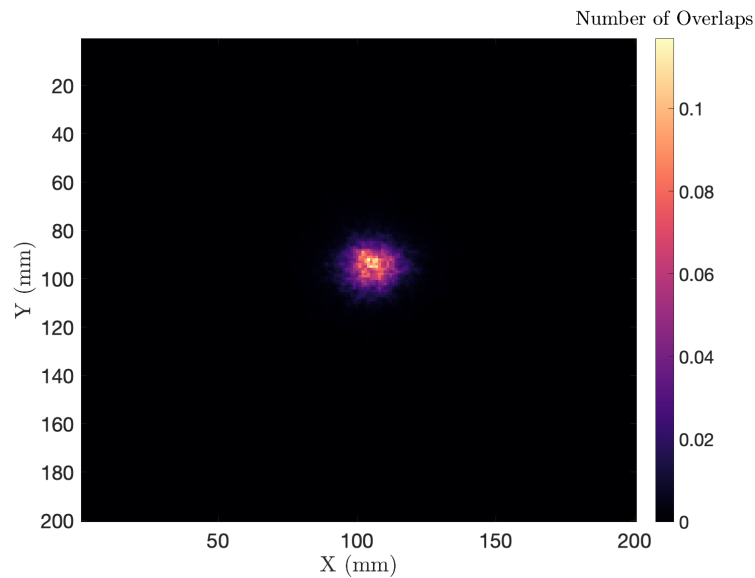


**(a)** Image of Fold 1 events using online algorithms.
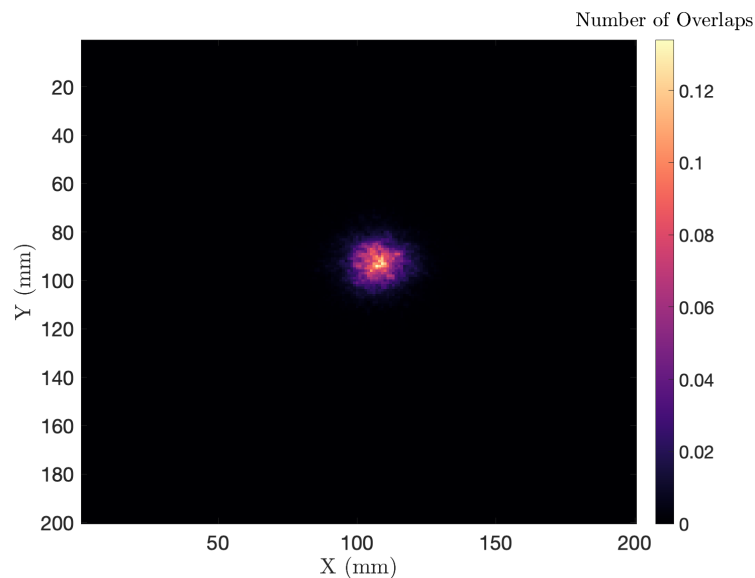


**(b)** Image of Fold 1 events using offline algorithms.

**Figure 5.20:** Images of Fold 1 events using (a) online and (b) and offline algorithms. MLEM reconstruction code was used with the $5^{th}$ iterations.
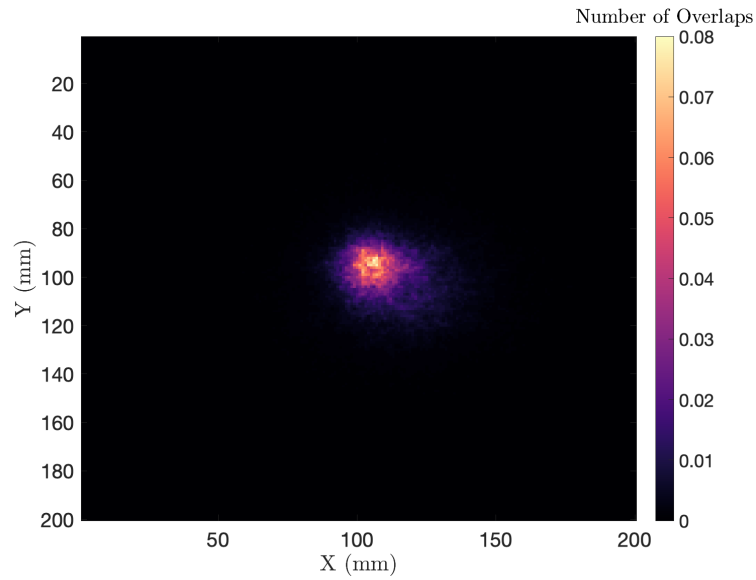
**(a)** Images of all Folds events using online algorithms.
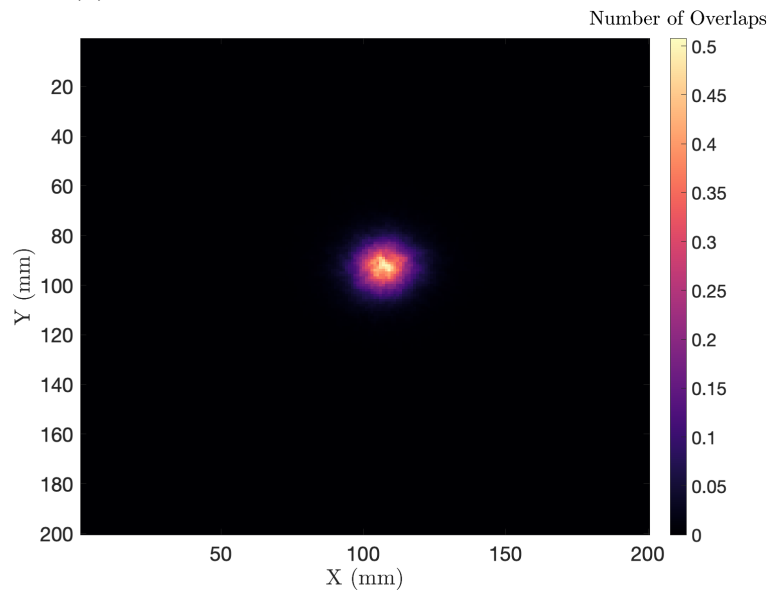


**(b)** Images of all Folds events using offline algorithms.

**Figure 5.21:** Images of all Folds events using (a) online and (b) and offline algorithms. MLEM reconstruction code was used with the $5^{th}$ iterations.

**(a)** Fold 1 events using online analysis.



**(b)** Fold 1 events using offline analysis.



**(c)** All Fold events using online analysis.



**(d)** All Fold events using offline analysis.
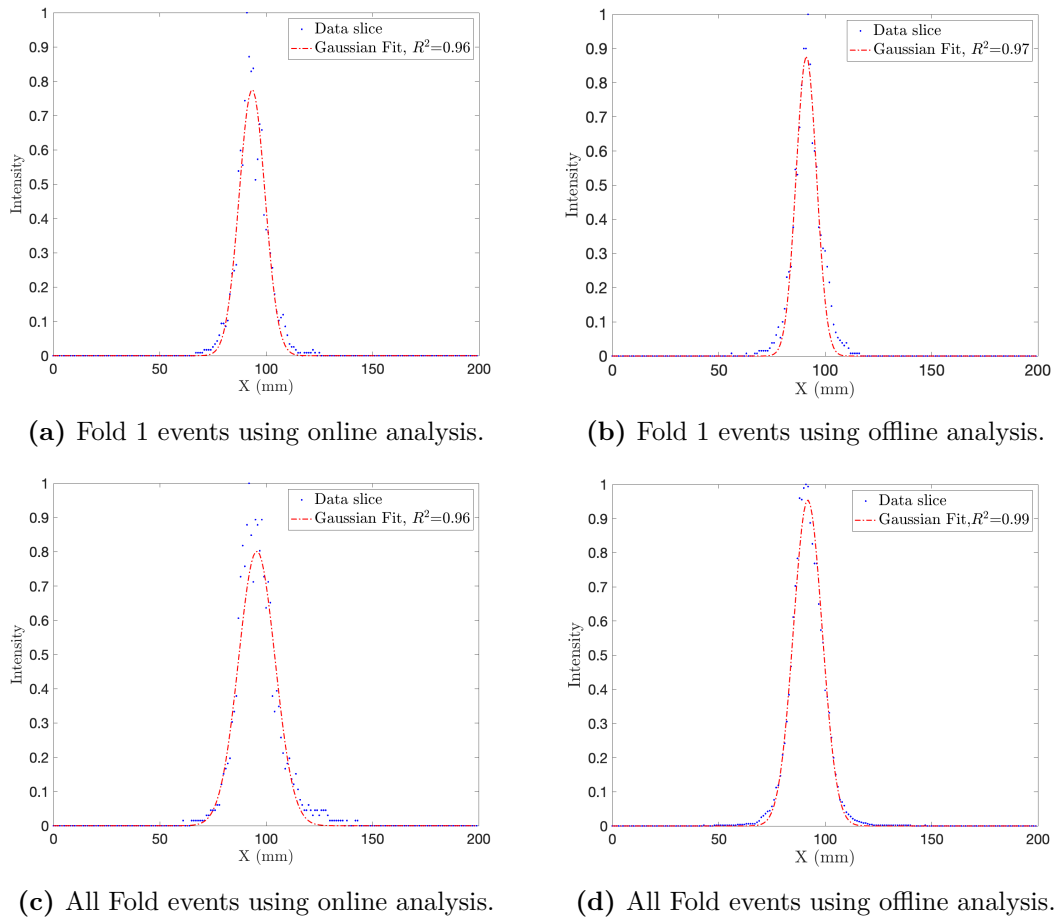
**Figure 5.22:** The corresponding slice fit for the reconstructed images of (a) Fold 1 events using online analysis, (b) Fold 1 events using offline analysis, (c) All Fold events using online analysis, and (d) All Fold events using offline analysis.

The best achievable image resolution was when the $16^{th}$ iteration was used with offline analysis. The FWHM was calculated to be $7.2 \pm 0.6$ mm and $10.5 \pm 0.8$ mm for Fold 1 and all Folds events, respectively. An improvement of factor 2 is reported when using offline analysis in comparison to the online analysis, as shown in Table 5.7. The Fold 1 and all Folds images for the $16^{th}$ iterations of the offline analysis are shown in Figure 5.23, and corresponding slice fits are shown in Figure 5.24.

**Table 5.7:** The Gri+ system image resolution using online and offline algorithms for Fold 1 and all Fold events using MLEM reconstruction code. The best possible iteration was used which are the $5^{th}$ and $16^{th}$ iterations were used for the online and offline analysis, respectively.

|  | Online algorithm | Offline algorithm |
|---|---|---|
| **Fold 1** | $13.6 \pm 0.8$ | $7.2 \pm 0.6$ |
| **All Fold** | $20.2 \pm 1$ | $10.5 \pm 0.8$ |
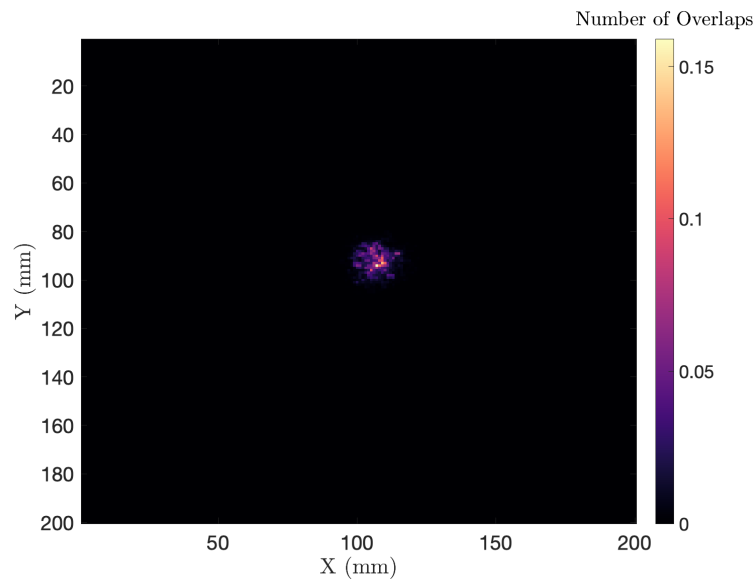


**(a)** Image of Fold 1 events using offline algorithms.
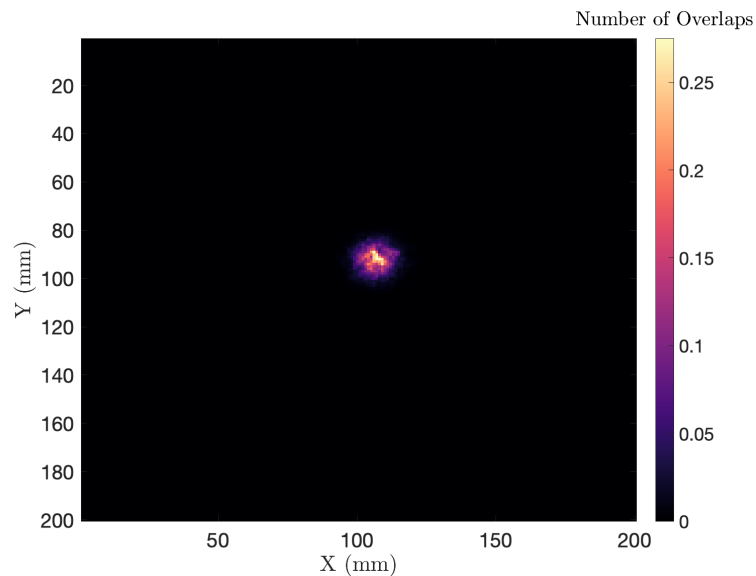


**(b)** Image of all Fold events using offline algorithms.

**Figure 5.23:** Images of (a) Fold 1 events, and (b) all Folds events using offline algorithms. MLEM reconstruction code was used with the $16^{th}$ iterations.
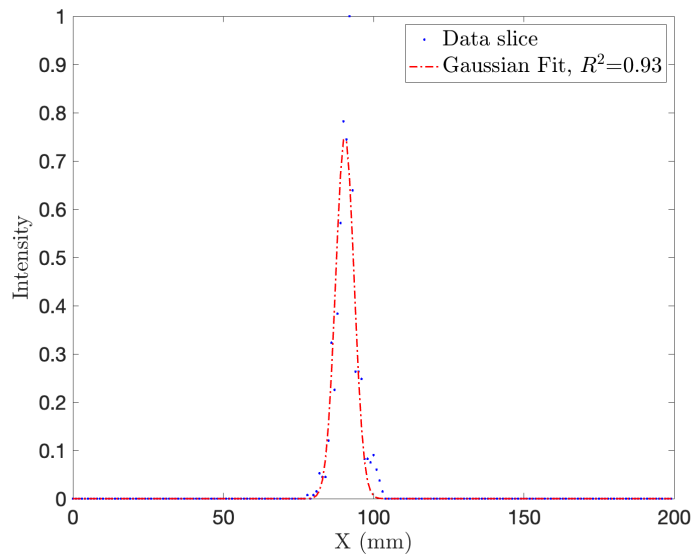
**(a)** Slice fit for the reconstructed images of Fold 1 events using offline algorithms.
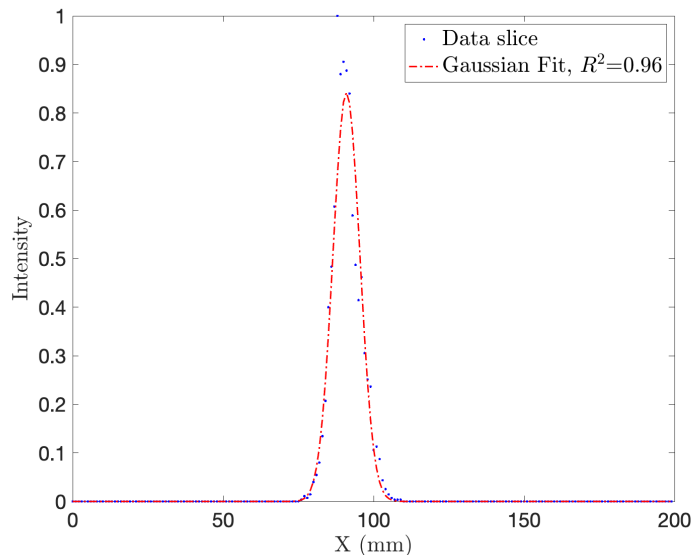


**(b)** Slice fit for the reconstructed images of all Fold events using offline algorithms.

**Figure 5.24:** The corresponding slice fit for the reconstructed images of (a) Fold 1 events, and (b) all Fold events using offline analysis. MLEM reconstruction code was used with the $16^{th}$ iterations.

## 5.4 Recommendations for operational parameters

The current Gri+ system setup was previously investigated using the highest gamma-ray energy available. Based on those investigations, different setup recommendations for using the Gri+ system in the proton beam therapy verification will be reported in this section.

## 5.4.1 The dynamic range

The current setup for digital acquisition system uses the GO box. The GO box amplifies signals by a fixed gain factor 5X for scatterer and 2X for the first absorber. This to maintain the full dynamic range of the CAEN cards (2.25 V), after which it applies an offset to the signal voltage in order to adjust the baseline position (see Chapter 4 Section 4.1.2).

The gamma energy response to the full dynamic range of the digitizer CAEN cards voltage is unknown for the current setting. Hence, it is essential to evaluate the suitability of the use of the current setting in imaging the prompt gamma-ray during the Proton therapy for gamma energy of 4.4 MeV and 6.1 MeV.

To this end, $^{241}$Am,$^{57}$Co, and $^{137}$Cs point sources and an oscilloscope (Agilent model MSO7104A) have been used to measure the collected voltage for three different gamma rays for each detector. Subsequently, the three gamma ray energy and the voltage collected in the detector were plotted and a linear fit applied. The slope and the intercept from the linear fit equation are employed to calculate the value of the gamma energy response to 2.25 V deposited in the detectors. This procedure is repeated for each detector without using the GO box so that no gain factor is employed. As the highest interested prompt gamma ray in the proton therapy is 6.13 MeV, both the scatterer and the first absorber detector must be able to process these high energy gamma rays within the dynamic range of the CAEN cards.
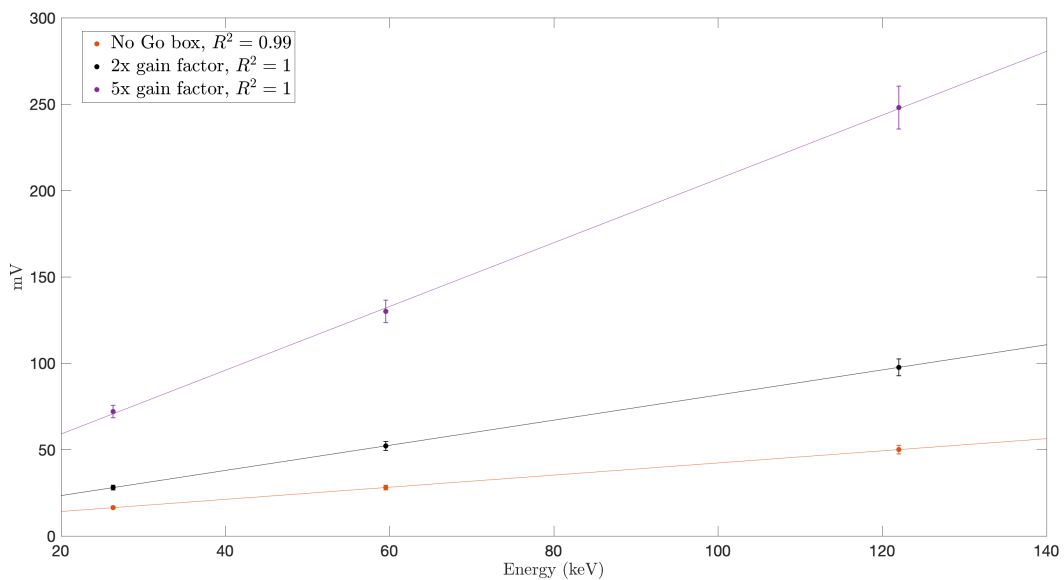


**Figure 5.25:** The collected voltage response to 26 keV, 59 keV, and 122 keV gammas for the scatterer detector. Three linear fits for 5X and 2X gain factors and without using GO box (without gain).
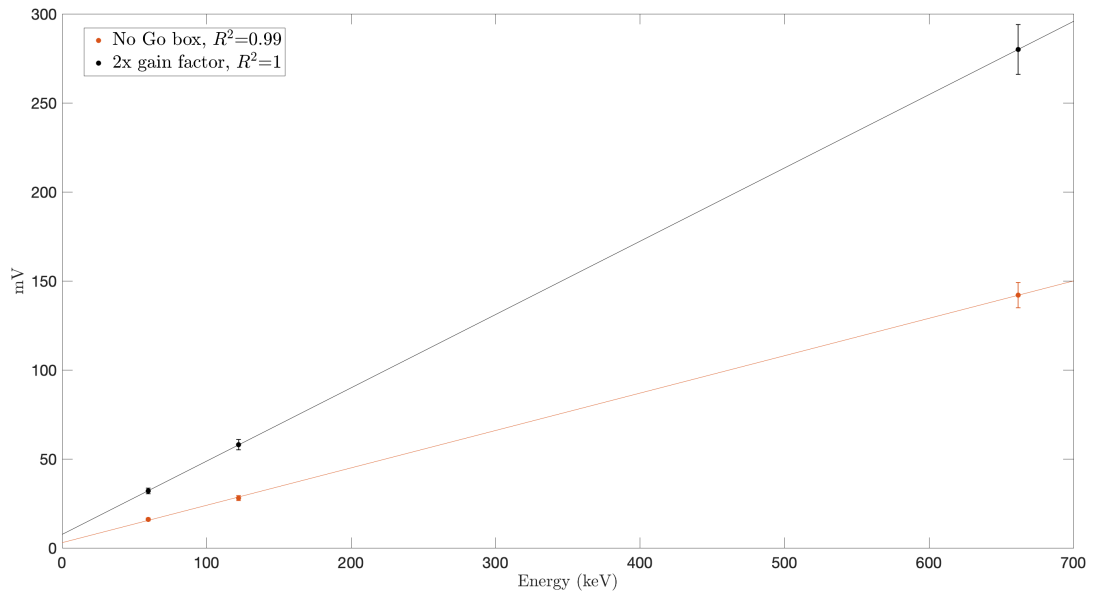
**Figure 5.26:** The collected voltage response to 59 keV, 122 keV, and 660 keV gammas for the first absorber detector. Two linear fits for 2X gain factor and without using GO box (without gain).

For the scatterer detector, using 26 keV, 59 keV, and 122 keV gammas and the collected voltage response to those energy in plot, as shown in Figure 5.25. The maximum energy that the digitizer can process for 5X, 2X gain factor and without using GO box were 1.2 MeV $\pm$ 0.1 MeV, 3.1 MeV $\pm$ 0.2 MeV, and 6.4 MeV $\pm$ 0.4 MeV, respectively. For the first absorber detector, using 59 keV, 122 keV, and 660 keV gammas and the collected voltage response to those energy in plot as shown in Figure 5.26. The maximum energies that the digitizer can process for the 2X gain factor and without using GO box were 5.5 MeV $\pm$ 0.2 MeV and 10.7 MeV $\pm$ 0.2 MeV, respectively.

For the current setting, the maximum possible scattering angle is 64.7°, as shown in Figure 5.4. Thus, for the 6.13 MeV gamma placed 25 cm from the scatterer detector, the possible energy range can be deposited in the scatterer and the first absorber will be 4 keV to 5.3 MeV and 780 keV to 6.1 MeV, respectively. This calculation and previous experimental results suggest that both the scatterer and the first absorber have a limited energy range that the digitizer can process when using any gain factor within the GO box. It would still be possible to use the GO box to adjust the baseline position. However, using custom-made cards have a gain factor of 1X.

## 5.4.2 Energy selection

In the current setting of the Gri+ system, the energy deposited on the DC side of the scatterer and first absorber detector were used in reconstructed image. This is because of the superior energy resolution of DC side at low energy. However, the AC side of the first absorber detector displays better energy resolution for gamma energy higher than 900 keV, as discussed in Chapter 4 Section 4.1.1.

This section evaluates the implications of using the energy deposited on AC side instead of using DC side energy in reconstruction image and decide how to implement this method. To this ends, a range of gamma rays of 344.2 keV, 778.9 keV, 963.4 keV, 1406.5 keV, and 1.8 MeV from $^{152}$Eu and $^{88}$Y sources were used. These sources were place 10 cm away from the Gri+ system while the system operated in coincidence mode.
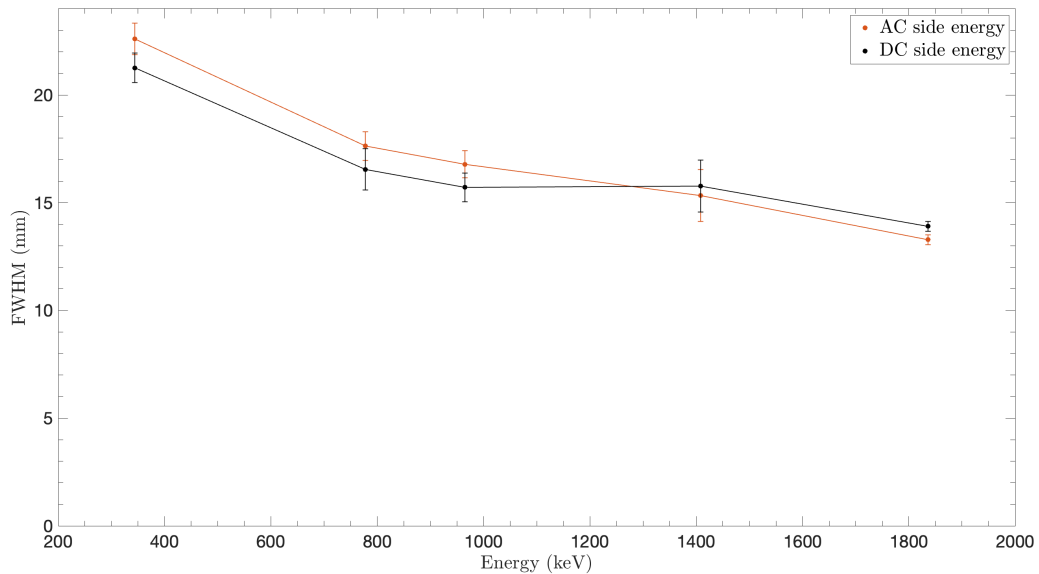


**Figure 5.27:** The image resolution used the AC side and DC side energy over range of gamma rays energy. Only Fold 1 events and 2-tier type were used.

Using the AC and DC side energy in the imaging was evaluated for the range of gamma-ray energies 344 keV to 1.8 MeV where only Fold 1 and 2-tier type events were used. The image resolution using the DC side energy shows superior image resolution until the gamma-ray energy of 963.4 keV. Then, at 1408 keV, the image resolution using the AC side energy has slightly better image resolution. However, the image resolution using the AC side energy has superior image resolution at 1836 keV, as shown in Figure 5.27. To understand such behaviour, the percentage of gamma-rays that are deposited below and above 900 keV in the first absorber detector will be explored as the 900 keV is the threshold where the AC side has

better energy resolution than the DC side. This investigate was for a range of gamma rays energy of 344.2 keV to 1.8 MeV, as reported in Table 5.8.

**Table 5.8:** The percentage of the gamma rays that deposited part of its energy below and above 900 keV in the first absorber detector. The Gri+ system was operated in coincidence mode and only Fold 1 events and 2-tier type were used.

| Incoming gamma energy (keV) | Below 900 keV (%) | Above 900 keV (%) |
|:---:|:---:|:---:|
| 344.2 | 100 | 0 |
| 778.9 | 100 | 0 |
| 963.4 | 85 | 15 |
| 1406.5 | 32 | 68 |
| 1836 | 5 | 95 |

For 344.2 keV, keV 778.9 keV gamma-ray, all their gamma rays were deposited below 900 keV because the full energy of the incoming gamma ray was less than 900 keV. While, for 963.4 keV gamma-ray, 85 % of the gamma rays were deposited below 900 keV. However, for the 1406.5 keV gamma-ray, 32 % of the gamma rays were deposited below 900 keV, whereas 68 % were deposited above 900 keV, which might explains the slightly improve in image resolution when the AC side energy was used. For 1.8 MeV gamma-ray, almost all the gamma rays were deposited above 900 keV. It can see from this result that the percentage of the gamma-ray is deposited above 900 keV in the first absorber detector can be the deciding factor in the choice of the AC side energy instead of the DC side energy in the imaging. This investigation was only for Fold 1 and 2-tier type events. However, at high gamma-ray energy, the fold level tends to increase with an increase in the incoming gamma energy, so the percentage of the gamma rays that deposited part of their energy below and above 900 keV in the first absorber detector for Fold1 and Fold 2 events were investigated. A similar result was found for all energies apart from 1406.5 keV and 1.8 MeV, as reported in Table 5.9.

**Table 5.9:** The percentage of the gamma rays that deposited part of its energy below and above 900 keV in the first absorber detector. The Gri+ system was operated in coincidence mode and both Fold 1 and Fold 2 events and 2-tier type were used.

| Incoming gamma energy (keV) | Below 900 keV (%) | Above 900 keV (%) |
|:---:|:---:|:---:|
| 1406.5 | 24 | 76 |
| 1836 | 3 | 97 |

In addition, the events categorised as 3-tier type tend to increase with an increase in the gamma-ray energy where about 35 % of the events were categorised
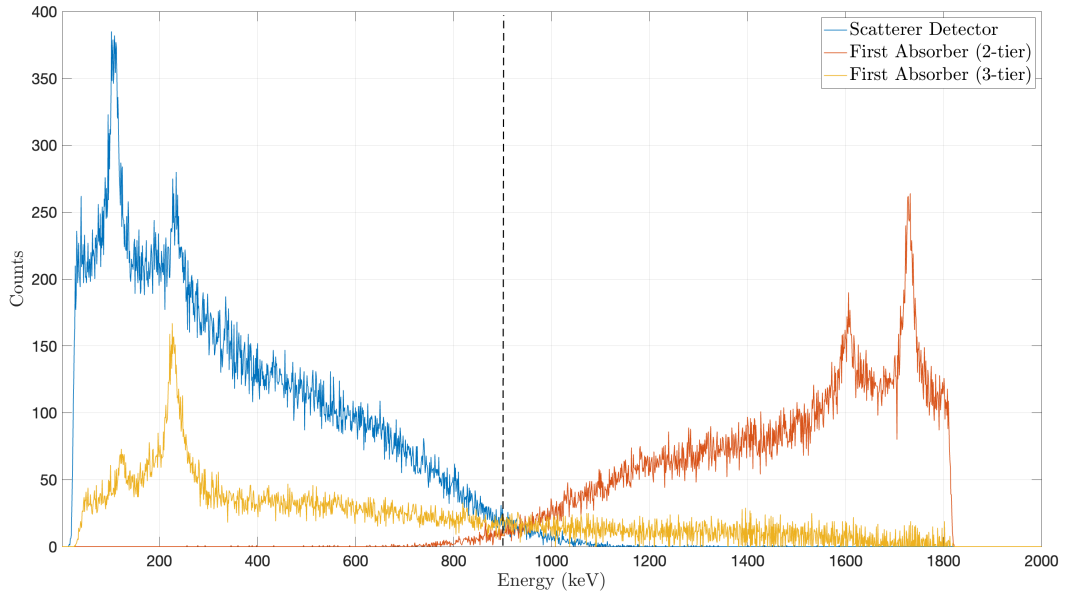
**Figure 5.28:** The DC energy addback spectra for the scatterer and the first absorber detectors (2-tier and 3-tier) with the gate on the total energy deposited in the system of 1.8 MeV. The black dash line is to indicate the 900 keV in spectrum.

as a 3-tier type at the 1406.5 keV gamma-ray, as discussed in Section 4.2.3. For 1.8 MeV gamma rays, about 41 % of the events were categorised as a 3-tier type. Figure 5.28 displays the DC energy addback spectra for the scatterer and the first absorber detector using 2-tier and 3-tier event type with applied energy gate on total energy deposited in the system of 1.8 MeV. This figure shows that a large fraction of the gamma-ray deposited part of its energy above the 900 keV in the first absorber detector as a 2-tier type. The percentage of gammas that deposited part of its energy below and above 900 keV for the gamma ray energy of 1.8 MeV was reported in Table 5.10.

**Table 5.10:** The percentage of the gamma rays that deposited part of its energy below and above 900 keV in the DC addback energy spectrum of the first absorber detector. The Gri+ system was operated in coincidence mode and both Fold 1 and Fold 2 events were used.

| First Absorber | Below 900 keV % | Above 900 keV % | Total % |
|:---:|:---:|:---:|:---:|
| 2-tier | 3 | 97 | 100 |
| 3-tier | 80 | 20 | 100 |

Most gammas deposited part of their energy above 900 keV as a 2-tier type. However, for the 3-tier type, most gamma rays deposited part of their energy below 900 keV. Thus, using the AC side energy for the 2-tier type events and the

DC side energy for the 3-tier type events are recommended in high gamma ray energy.

Using the AC side energy has a variant effect on the image resolution depending on the energy of the incoming gamma-ray. In addition, the number of gamma-rays deposited part of their energy above 900 keV in the first absorber detector. Using the AC side energy in the imaging improves the image resolution at 1.8 MeV. Thus, using the AC side energy for the 2 -tier type events and the DC side energy for the 3-tier type events are recommended for imaging higher gamma energy than 1406.5 keV. However, this evaluation might be limited to the current experiment geometry. Because of the detector separation and the source to the detector distance can influence the energy range deposited in the first absorber.

## 5.5   Summary

The energy spectra analysis for a high-energy gamma-ray of 1.8 MeV revealed that about 55% of the $\gamma$-ray experienced a narrow scattering angle. The fold level tends to be more complex with increases in the incoming gamma energy. The Fold 2 event was $\sim$50% and Fold 3 was $\sim$27% at 1.8 MeV gamma energy. Using Fold 2 events significantly increased the Gri+ system's imaging efficiency from $\sim$ 27% to 70% for all events registered in the system at 1.8 MeV gamma energy emitted from $^{88}$Y. A more complex event sequence is expected for prompt $\gamma$-ray imaging during proton therapy, which could significantly influence Compton imaging efficiency. The Gri+ system can successfully image a high-energy $\gamma$-ray of 1.8 MeV for Fold 1 and Fold 2 events. Imaging Fold 2 greatly degrades image resolution. Image resolution compression using online and offline algorithms demonstrated that offline algorithms had superior image resolution for Fold 1 and Fold 2 events. Therefore, the offline algorithm can significantly mitigate the image resolution degradation of Fold 2 events, however, with an additional computational time and cost. The best achievable image resolution using an offline algorithm was $7.2 \pm 0.6$ mm and $10.5 \pm 0.8$ mm for Fold 1 and all fold events, respectively. The current Gri+ system setup has a limited energy processing capability of up to 3.1 MeV because of the gain used in the GO box. The D-DAQ must be set up without using the GO box or a GO box with a gain factor of 1X to image the prompt $\gamma$-rays of 4.4 MeV and 6.1 MeV during proton therapy. For imaging the $\gamma$-ray of energy higher than 1.4 MeV, it is recommended to use the AC side energy for imaging the 2-tier events instead of the DC side energy and the DC side energy for imaging the 3-tier events.

# Chapter 6

# Evaluation of Gri+ performance at high count rates

Evaluating the Gri+ system performance in a high-count rate scenario is essential because of the high level of radiation present in the proton therapy environment. The system performance of Gri+ has been evaluated using a phantom filled with high activity radioactive solution. This was followed by a count rate investigation where the Gri+ digital system (D-DAQ) count rate was compared with the analogue pulse counting and the analogue pulse height analysis system's count rate. The effect of increasing the number of detector channels used in the D-DAQ system was then investigated. Finally, the Gri+ system performance when it is setup for Compton imaging was determined.

## 6.1    The system performance using a high activity phantom

A phantom used to evaluate performance was 3D printed and designed by the Royal University Liverpool hospital. It modelled an anatomically correct thyroid as shown in Figure 6.1. The phantom was a cylinder designed to mimic the neck with a hollow volume shaped like a thyroid. The hollow volume was filled by a medical physicist from the hospital with $^{99m}$Tc solution which had an activity of 10 MBq as measured by a calibrator within the hospital. $^{99m}$Tc has a half-life of 6.01 hours and the main decay is a gamma ray of 140.5 keV with a 89% probability of emission. The phantom was placed on a rotary Velmex table with a wooden support to ensure alignment of the thyroid at the centre of the field of view. This was rotated to different angular projections (0°, 30°, 60°, 90°, and 330°) and imaged for different time periods based on the phantom activity throughout the measurement. Longer measurements were required as the activity reduced. Table 6.1 shows the average phantom activity, the angular projections,

and the measurement time of the data set. The centre of rotation as noted was the geometric centre of the phantom. This measurement was mainly taken as part of another project that examined the imaging capability of the Gri+ in nuclear medicine, which explains the choice of the phantom shape and the low gamma-ray energy. Sorting this data shows a significant data loss, which led to a detailed count rate investigation for the Gri+ system in this thesis. The data were recorded when the Gri+ system was in 2-tier configuration because it is sufficient for low gamma energy of 140.5 keV which does not penetrate into the third detector due to its path length. The system was operated in coincidence mode with Output as all masked and the entire 48 channels of D-DAQ system were used. MIDAS version 5 and the D-DAQ system firmware version 4.15 were used in this experiment.
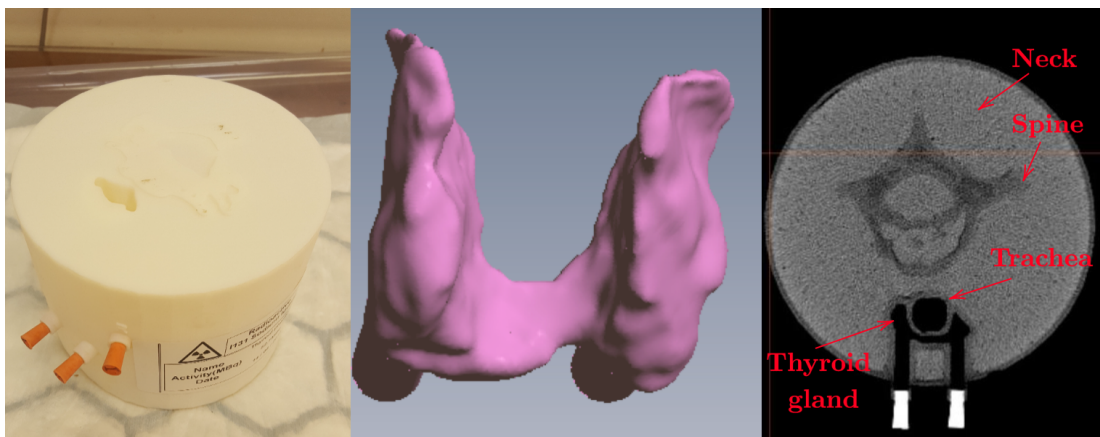


**Figure 6.1: Left** A photograph of the phantom, **Middle** CAD drawing of the fillable volume of thyroid gland within the phantom and **Right** Transaxial slice of the phantom by CT scan. The images were provided by the Royal University Liverpool hospital.

**Table 6.1:** Experiment data set information.

| *Average Activity (MBq) | Angular Projection (degrees) | Measurement Time (Hour) |
|---|---|---|
| 7 | 90 | 3.4 |
| 4.5 | 60 | 3.3 |
| 2.9 | 30 | 4 |
| 1.7 | 330 | 5 |
| 0.9 | 0 | 7 |

\*__Average activity__ corresponds to the phantom activity at the middle of the measurement time for each data set.

## 6.1.1   System performance indicators

To determine the system performance, the system count rate was extracted online from MIDAS and the data size was extracted from the data storage disk. The total

number of coincidence events and number of imageable events that can be input for image reconstruction were extracted offline from sorted data using MTsort. As the measurement times for all five datasets were different, some of the system performance calculated indicators required division by the measurement time in seconds to report as average rates, these instances are clearly indicated within the text. The key system performance indicators are defined as:

- **The system count rate** is the accepted trigger rate that the digitiser cards (CAEN V1724) processed (CPS) for each of the 48 channels, measured only at the beginning of each dataset.

- **The data storage rate** is the size of stored data (Kbytes) in the disk during the data acquisition for each of the five datasets. This indicator will be divided by the measured time.

- **The total event rate** is an event counter extracted and sorted from saved data from the disk using MTsort without the inclusion of energy or fold gates, divided by the measured time (CPS).

- **The peak-to-total ratio** is the total count of the full energy peak in the DC addback energy spectrum divided by the total number of counts greater than 100 keV in the spectrum without applying fold gates.

- **The imageable event rate** is the number of events that pass the energy gates and the event fold gate while requiring that the event has only interacted once with each detector, divided by the measured time (CPS).

## 6.1.2   Data sorting

The fivesets of data were sorted using MTsort to obtain the necessary indicators. A preliminary sorting exhibited several false coincidence events. A gamma-ray line of 281 keV is observed in the total energy spectra occurring as a consequence of a summing random coincidence whereby a 140.5 keV gamma-ray is accounted for in both the scatterer and first absorber detectors within the coincidence window as shown in Figure 6.2. These are more probable at a high rate.
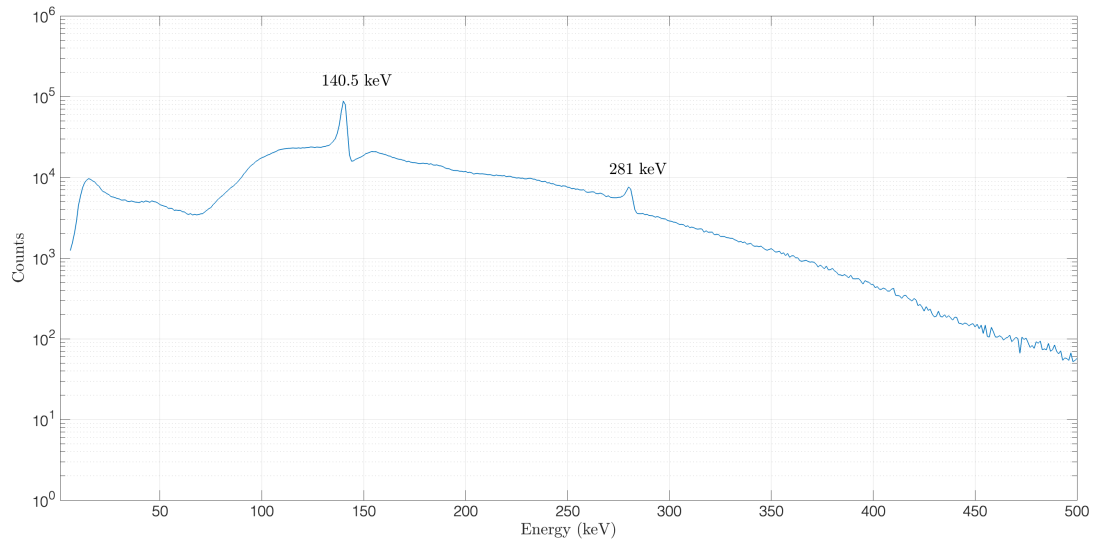
**Figure 6.2:** The DC addback energy spectrum produced for the first dataset of average activity 7 MBq, clearly showing the random coincidence peak of 281 keV. This spectrum is generated by summing the DC addback spectra for the scatterer and the first absorber detector, as is used for Compton images.

To reduce random coincidence events contributing to the Compton image, three energy gates were applied during the sorting process. The first energy gate was applied to the total energy deposited in the system (138.5 keV -142.5 keV) which selects $\gamma$'s that have deposited full energy in the system. In addition, two single energy gates were applied on the scatterer and the first absorber, respectively. Both single energy gates were estimated by calculating the maximum Compton scattering angle geometrically possible from the scatterer detector. This estimation is dependent on the position of the phantom to the scatterer detector and the separation between the scatterer and the first absorber detector. By calculating the maximum Compton scattering angle and using Equation 3.5 in Chapter 3 Section 3.1.2, the maximum gamma energy deposited in the scatterer detector can be estimated, with the rest of the 140.5 keV being deposited in the first absorber. As a consequence of the phantom's rotational movement, the position of the phantom to the scatterer detector was not constant. This variation in phantom-detector position was taken in to account when calculating the single energy gates, and the largest possible Compton scattering angle of this set up was selected. For a phantom placed 55 mm from the scatterer detector, with a detector separation of 15 mm, the maximum Compton scattering angle was estimated to be 80.7° and the maximum possible energy deposited in the scatterer detector will therefore be 26.7 keV. For a $\gamma$-ray fully absorbed in the Gri+ system, the remaining 114.8 keV will be deposited in the first absorber. Considering the low energy threshold of 4 keV applied to the scatterer detector, the single energy gate on the scatterer

is 4 keV- 26.7 keV, and on the first absorber is therefore 114.8 keV − 136.5 keV. The energy and fold gates described here will only affect the imageable events indicator.

### 6.1.3 Results and discussion

Maintaining personal safety while recording the system count rate through the experiment presented a challenge. Specifically, there was a risk of over-exposure to researchers due to the phantom's high activity, given that the computer was placed next to the detector system and a stable remote connection to another PC could not be achieved on the experiment day. However, the value was recorded at the start of each data acquisition run. The current study found that the system count rate and the data storage rate exhibit a linear correlation with the total event rate, as shown in Figure 6.3. As a result of these linear correlations, the total events indicator can and will be used for further system performance analyses.
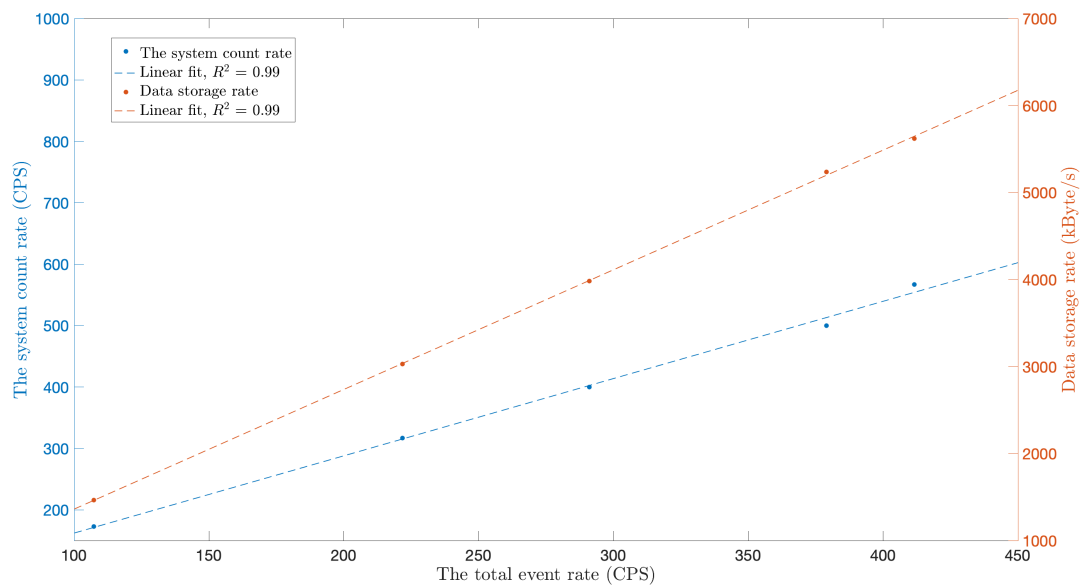


**Figure 6.3:** The linear corelation between the system count rate and the data size with total events indicators.

The phantom activity is expected to be observed as an exponential decay with a starting activity (first dataset) of 8.34 MBq, which is calculated to reduce to 0.56 MBq by the end of the fifth dataset. The total event rate is expected to show a direct proportional response to the phantom activity if the dead time and change in detection efficiency due to geometrical variation through phantom rotation do not occur. However, the total events indicator shows only a slight increase with decreasing phantom activity between 7 MBq and 2.9 MBq and then

the total events indicator exhibits a steady decrease as shown in Figure 6.4. For the ideal detection system without considering the system dead time effect, the total events indicator should have a direct proportional response to the phantom's activity thus there is a significant data loss for activities greater than 2.9 MBq. By extrapolating a linear regression beyond the three lowest dataset, as shown in Figure 6.4 then the data loss is calculated to be 72 % compared to the expected total event rate at activity of 7 MBq and 41 % at 4.5 MBq.
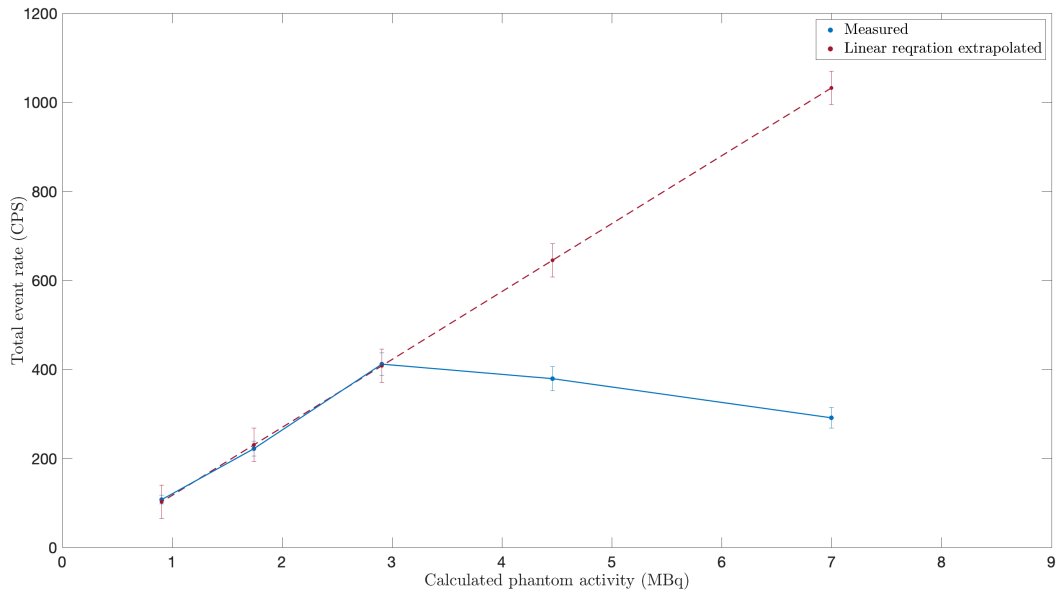


**Figure 6.4:** The measured total event rate across the five data sets as the activity decreases (blue line). The red dashed line is the expected total event rate calculated from the linear regression of the total event rate from data of activity below 2.9 MBq.

The steady decrease of the total event rate observed when the phantom activity is below 2.9 MBq follows the expected direct proportional response to phantom activity decay. The slight increase in the total event rate observed with decreasing phantom activity between 7 MBq and 2.9 MBq may be a consequence of the detector dead time and/or the decreased phantom-detector distance. For further investigation, the distance between the detector and the phantom has therefore been plotted as a function of phantom activity, as shown in Figure 6.5. It can be seen that the distance is similar for measurements when activity was 0.9, 1.7 and 2.9 MBq. However, the distance is increased at 4.5 and 7 MBq. Given that the distance between the phantom and the detector changes as the phantom rotates, the radiation flux on Gri+ will also change depending on the distance from the average radiation centre because the radiation flux is inversely proportional to the square of the distance (the inverse square law). In addition, the position of the active volume inside the phantom was changed within the Compton camera's

field of view when the phantom was rotated. A variation of imaging efficiency as a function of source position within the Compton camera's field of view for the Gri+ system was reported by [64]. This introduces an additional source of uncertainty to this experiment.
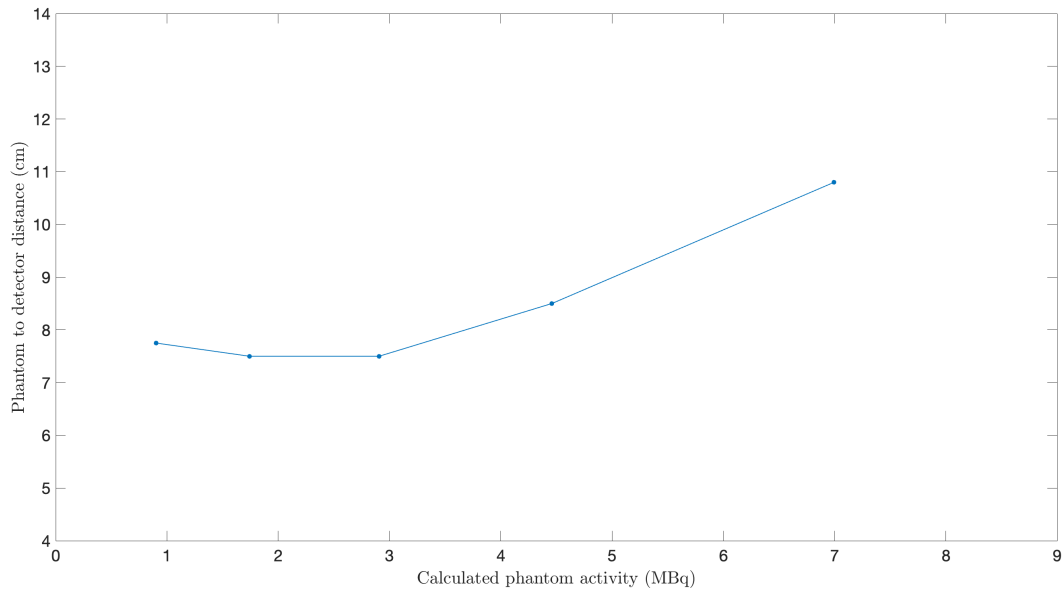


**Figure 6.5:** The distance between the detector and the phantom nearest point for the five datasets. The estimated uncertainty was $\pm$ 0.1 cm which is too small to be observed in this plot.

A correction for the variation in count rate because of the phantom to detector distance variation has been attempted. The phantom to detector distance has been decided from the nearest point for the phantom without considering the centre of the radiation because of the complex shape of the phantom. This will introduce an uncertainty to this correction. However, a correction for the imaging efficiency variation was not possible due to the difficulty of finding the exact position of the active volume inside the phantom to correlated into the Compton camera's field of view. Therefore, the applied correction can to some extent reduce the effects of the phantom to the detector distance (R). It is known from the inverse square law that the total event rate ($T$) will vary with distance ($R$) as $T \propto \frac{1}{R^2}$. Thus the corrected total event rate ($T_{Corrected}$) for each dataset will be as following: $T \times R^2$ and then it will normalised by dividing by $R^2$ of the dataset with shortest R (dataset of 1.7 and 2.9 MBq and R = 7.5 cm). The aim is to determine a better correction to allow relative comparison of the five datasets, rather than an evaluation of the true rates. This will align the total event rate with the corrected total event rate as shown in Figure 6.6.
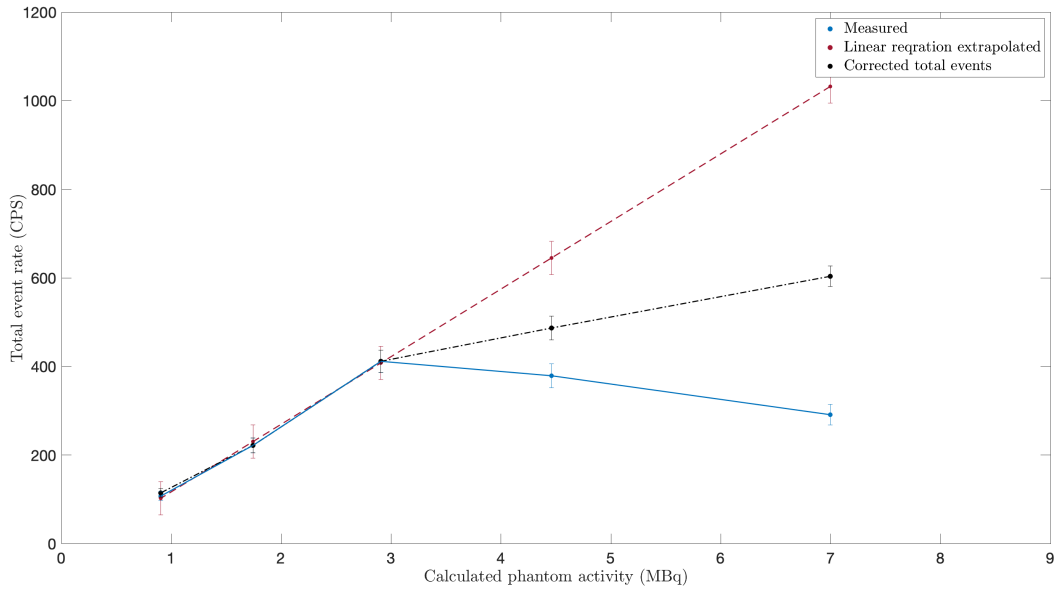
**Figure 6.6:** The total event rate measured for the five data sets as the activity decreases (blue line). The red dashed line is the expected total event rate calculated from the linear regression of the total event rate from data of activity below 2.9 MBq. The corrected total event rate from Figure 6.5 is shown as the black dashed line.

The corrected total event rate still shows a data loss for the phantom activity between 7 MBq and 2.9 MBq and data loss of 42% compared to the expected total event rate at activity of 7 MBq but with an improvement from uncorrected 72 % loss, as shown in Figure 6.6. Therefore, it is likely that the system has also experienced a dead time or count rate limitation that led to additional data loss of 30 %. This will be investigated further in Section 6.2. It has been decided to exclude the data for the phantom activity 7 MBq and 4.5 MBq for further analyses. Because the Gri+ system has experienced a huge data loss for those datasets and the active volume is far from the centre of the camera's field of view. Therefore, the attempt to correct the data for the phantom activity 7 MBq and 4.5 MBq will introduce a high uncertainty to the data and might influence the results.
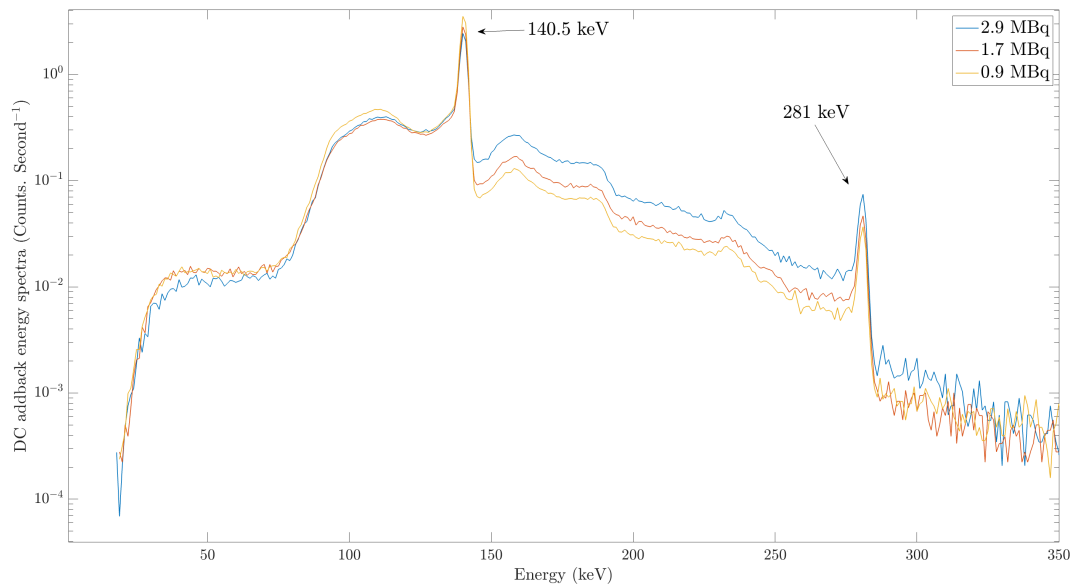
**Figure 6.7:** The DC addback energy spectra for three datasets with average activity of 2.9 MBq (blue), 1.7 MBq (red) amd 0.9 MBq (yellow). It clearly shows the random coincidence peak of 281 keV and the true coincidence peak of 140.5 keV.

Figure 6.7 shows the spectra for three datasets (average activity of 2.9 MBq 1.9 MBq and 0.9 MBq) where it shows that the background counts were high in comparison to peak when the phantom activity was high relative to low. It clearly also shows the random coincidence peak of 281 keV. To investigate the features of these spectra, the peak-to-total ratio was calculated for the 140.5 keV and 281 keV peaks from the DC addback energy spectra of those three datasets. The peak-to-total ratio shows the system's ability to fully absorb the gamma ray in comparison to all the gamma rays interacting in it. For a standalone detector, the peak-to-total ratio is not dependent on the radioactive source shape or the source to detector distances but strongly depends on the detector dimensions and material, the gamma-ray energy, and the detector surrounding material that the gamma ray may interact with [65], [66]. This suggestion might not be appropriate for the Compton camera system because the system geometry affects the accepted gamma ray register in the Compton camera. The decrease in the source to the detector distance will increase the possible maximum scattering angle resulting in a broader range of gamma-ray energy allowed to deposit their energy in the system. Therefore, possibly more accepted gamma rays are registered in the Compton camera.
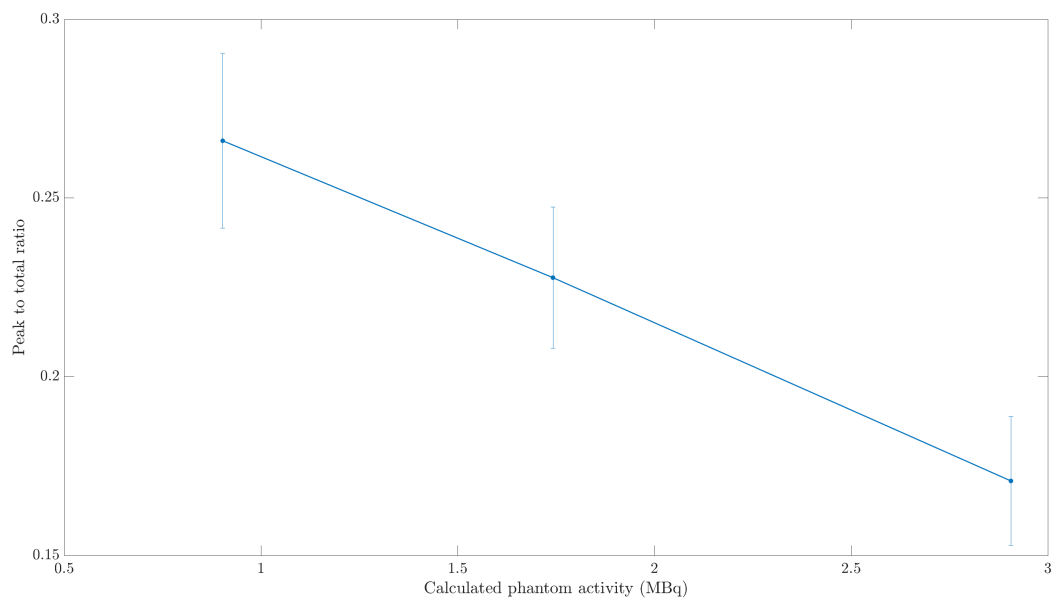
**Figure 6.8:** The peak to total ratio calculated for 140.5 keV at phantom activities of 2.9 MBq, 1.9 MBq and 0.9 MBq.
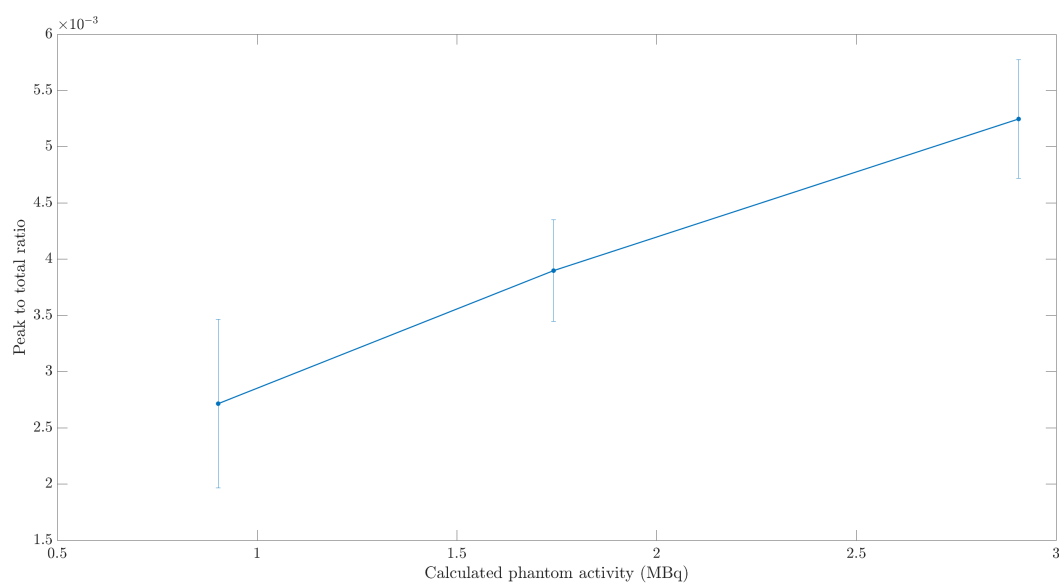


**Figure 6.9:** The peak to total ratio calculated for 281 keV at phantom activities of 2.9 MBq, 1.9 MBq and 0.9 MBq.
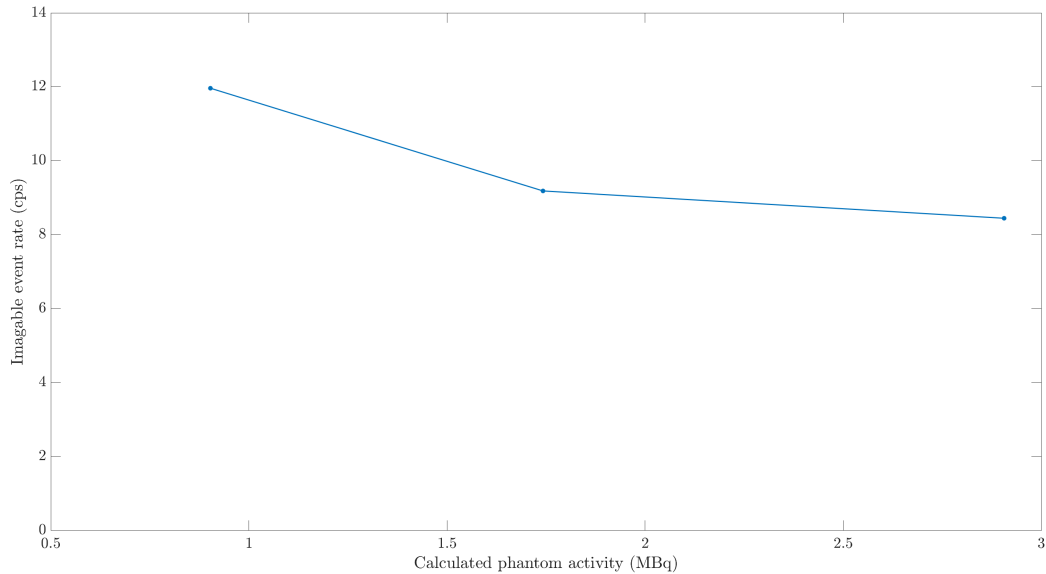
**Figure 6.10:** The imageable events count rate for the three datasets of activities 2.9 MBq, 1.9 MBq and 0.9 MBq.

It can be seen that the peak-to-total ratio for 140.5 keV increases with the decrease of phantom activity, as shown in Figure 6.8. While for 281 keV, the peak-to-total ratio decreases with the decrease of phantom activity, as shown in Figure 6.9. This result suggests that the true coincidence events increase and the random coincidence events decrease with decreasing the phantom activity. This observation needs more investigation along with a detailed study of system efficiency. This behaviour is also observed in the increase in the imageable events with the decrease of the phantom activity throughout the experiment as shown in Figure 6.10. This is an unexpected observation, it is expected to be proportional to phantom activity.

The data losses reported at higher activities could point to a count rate issue, which may be a consequence of the detector system experiencing dead time or having a limited count rate capability which will impact on how data can be recorded during proton beam therapy in the future. In addition, the peak-to-total ratio reports the true coincidence events increase and the random coincidence events decrease with decreasing the phantom activity. This behaviour also observed in the increase in the imageable events with the decrease of the phantom activity throughout the experiment. However, given the set up, it is difficult to draw any firm quantitative conclusion from this experiment. The complex geometry of the phantom and the variable phantom-to-detector distance and the phantoms short half-life combine to increase the uncertainty and difficulty of determining the cause of these effects. A further investigation is required in which a simpli-

fied approach may be applied. In the upcoming section, the Gri+ system will be further investigated using a long half-life, uniform shaped source.

## 6.2   The Gri+ system count rate investigation

In the previous experiment, a significant loss of data within the Gri+ system for measurement of the phantom at high activity was observed. An investigation in to the digital data acquisition system (D-DAQ) used in the Gri+ system was therefore implemented. In this experiment, the count rate from the sorted data using the D-DAQ system will be compared with analogue data acquisition (A-DAQ), then the count rate will be explored via the D-DAQ system component. To achieve this, different process stages will be investigated. The maximum count rate that the Gri+ system can process when setup for Compton imaging will be reported.

### 6.2.1   Comparison of analogue and digital acquisition systems

Two analogue data acquisition systems were setup in parallel with the D-DAQ system (see Chapter 4 Section 4.1). The D-DAQ system was operated with the optimum parameters that have been defined for this thesis. The energy spectra recorded from each strip from the detectors were calibrated using $^{241}$Am and $^{152}$Eu point sources. In addition, the $^{241}$Am point source was used to set the trigger threshold for each strip to be marginally greater than 59.5 keV. The D-DAQ system was operated in single mode and output as all masked. For D-DAQ, only the DC6 channel from the first absorber was instrumented, whereas the remaining channels were switched off.
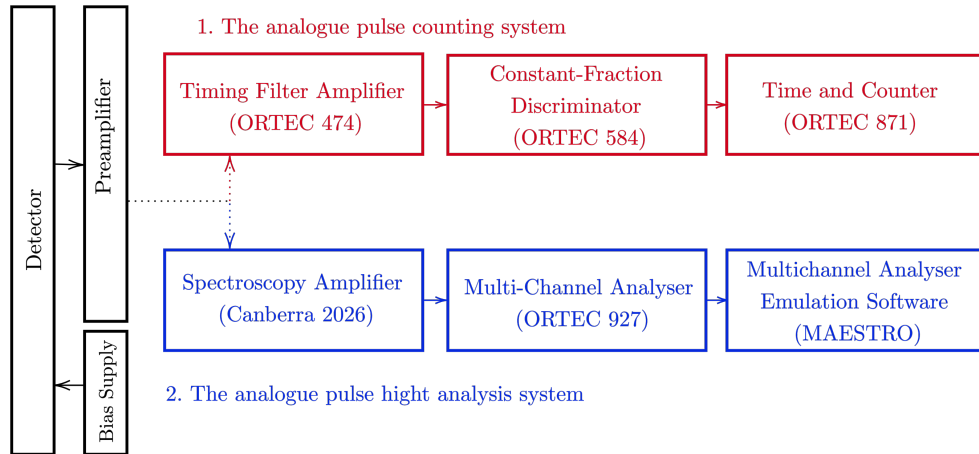
**Figure 6.11:** Schematic diagram for the analogue pulse counting and the analogue pulse height analysis systems setup.

Of the three parallel systems, the first was the analogue pulse counting system, which used a Timing Filter Amplifier (ORTEC 474), Constant-Fraction Discriminator (ORTEC 584), and Timer and Counter (ORTEC 871). A circuit diagram for the pulse counting system setup is shown in Figure 6.11. An oscilloscope was used to define the CFD threshold at a level marginally above 59.5 keV energy level. Since the equipment retains the fast timing, this system will provide the true count rate for one channel of the examined detector. It does not produce energy spectra.

The second system was an analogue pulse height analysis system. This used a spectroscopy Amplifier (Canberra 2026), Multi-Channel Analyser (MCA) (ORTEC Model ASPEC-927) and Multichannel Analyzer Emulation Software (MAESTRO). A circuit diagram for the analogue pulse height analysis system setup is also shown in Figure 6.11. The coarse gain of the spectroscopy amplifier was 50 and the shaping time was 4 μs. A shorter shaping time will result in better dead time. However, choosing this shaping time is because it comparable energy resolution to what will observe with D-DAQ system. The $^{241}$Am source used to again set the lower-level discrimination within MAESTRO Software for the individual strips to be marginally higher than 59.5 keV. This system can be used to produce energy spectra for comparison with D-DAQ spectrum.

A $^{137}$Cs vial with activity of 6.9 MBq was placed at 3, 5, 10 ,15, 20 and 25 cm distances from the first absorber detector. The experiment was conducted across the noted distances to vary the incident gamma rate and therefore detected count rate in the detector. The three systems were connected to the DC6 strip from the first absorber detector one at a time. To minimise the experimental setup error,

the source was not moved until each of the three systems finished taking data at the specified distance, and only the connector cable for attaching DC6 of the first absorber detector was switched between measurements with each system.
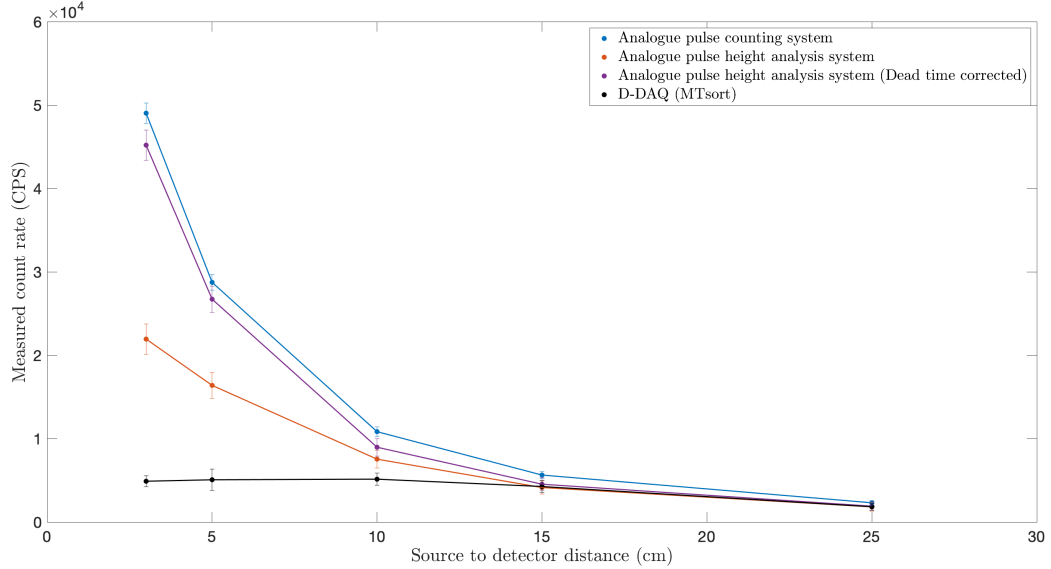


**Figure 6.12:** The count rate for the three systems: the analogue pulse counting (blue), the analogue pulse height analysis (red), the dead time corrected of the analogue pulse height analysis (purple), and the digital acquisition system (MTsort) (black) at different source to detector distances.

Figure 6.12 shows the count rate for the three systems measured across the range of source to detector distances. In the analogue pulse counting system, the count rate was measured for 300 seconds and repeated three times and the average was reported. While for the analogue pulse height analysis system, the count rate and the corrected count rate were extracted from the total counts in the DC6 energy spectrum using MAESTRO software. The count rate from the digital acquisition system was the total counts in the DC6 energy spectrum that was extracted from the sorted data using MTsort, and is denoted as the D-DAQ (MTsort) count rate. In the analogue pulse counting system, the count rate increases from 2k to 49k CPS as the source to detector distance decreases from 25 to 3 cm. Similarly, the analogue pulse height analysis system shows increasing count rate (1.8k to 22k CPS) as the distance decreases; however, it exhibits a dead time from 4% to 60%. The dead time values were extracted directly from MAESTRO. The D-DAQ (MTsort) shows increasing count rates as the source to detector distance decreased to 10 cm, thereafter then the count rate did not increase further. This result shows that the D-DAQ system appears to be limited to a count rate of 5.1k CPS when triggered and reading out a single detector

channel.  Figure 6.13 shows the differences between the analogue pulse counting system and the D-DAQ (MTsort) count rate.  Consequently, the investigation presented in the following section focuses on the D-DAQ system count rate by investigating the D-DAQ system through its different stages.
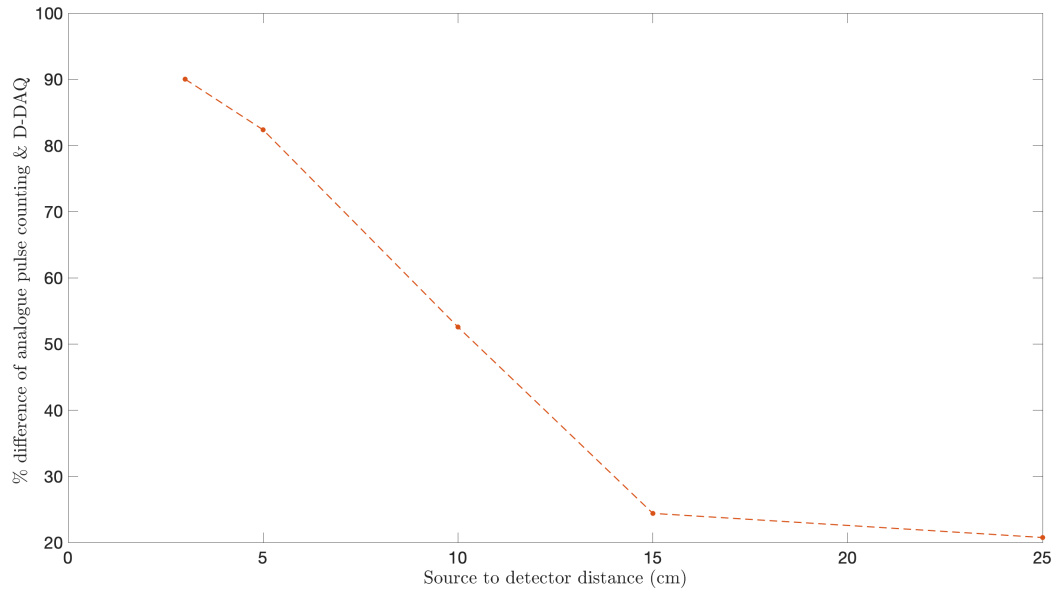


**Figure 6.13:** The differences between the analogue pulse counting system and D-DAQ (MTsort)count rate.

## 6.2.2   The D-DAQ system count rate investigation

A $^{137}$Cs vial with activity 6.9 MBq was placed at distances of 3, 5, 10, 15, 20 and 25 cm from the first absorber detector.  The first absorber detector was used as standalone detector.  This experiment was conducted across a variety of distances to facilitate a gradual increase the count rate at the detector as described in the previous section.  The D-DAQ system was operated in singles-mode and output as all masked.  Only the DC6 channel from the first absorber detector was operational in the D-DAQ system, while the remaining channels were off.  MIDAS version 7 and the D-DAQ system firmware version 4.19 were used in this experiment.  The DAQ system was investigated through the three stages shown in Figure 6.14.
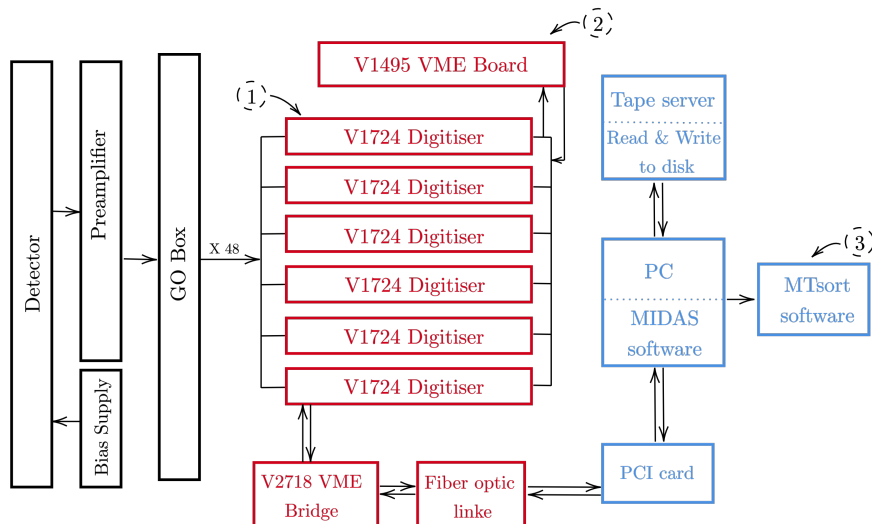
**Figure 6.14:** A Schematic diagram of the digital acquisition system and the three stages investigated.

Investigating the count rate within the D-DAQ system component in this manner, clearly demonstrated the count rate limitation through the D-DAQ components. For the first stage, the initial trigger rate that passes to the CAEN V1495 is used to determine whether the trigger logic requirements were met prior to passing to the digitiser cards for processing. In the following discussion, this stage will be called the Trigger. In the second stage, which will be termed the Digitiser, represents the accepted trigger rate that was processed in the digitiser cards (CAEN V1724) after meeting the requirements of the trigger logic from the CAEN V1495. The third stage, termed herein as MTsort, is the number of events that MTsort has sorted from saved data in the disc. This third stage determines the output of the MTsort and tests the optical link bridge, the throughput of the fibre optic link, the PCI card located in the PC, the PC processing ability, and the tape server (read and write to disk).
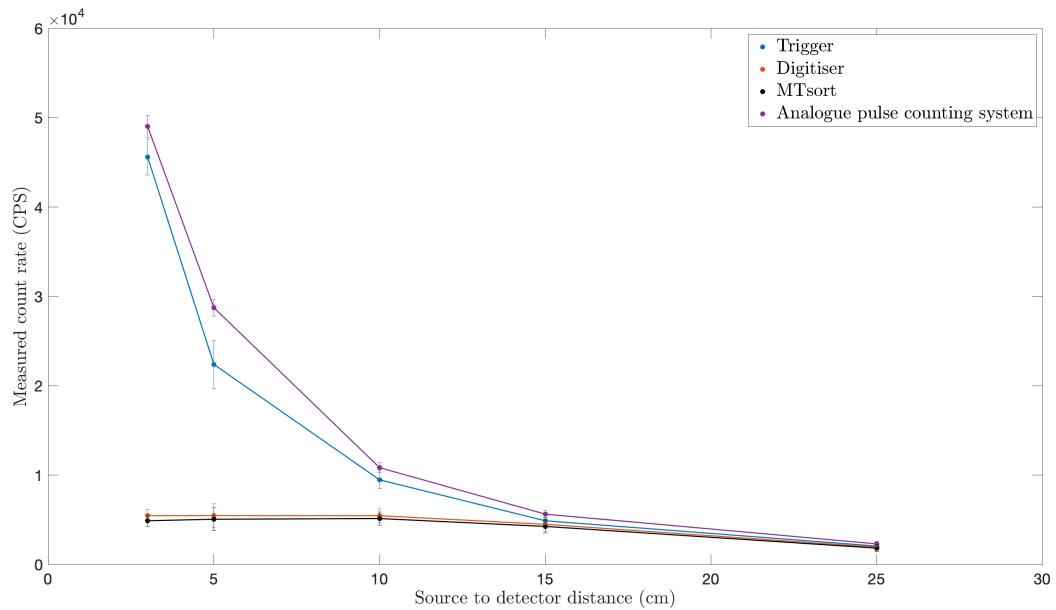
**Figure 6.15:** The count rates for the three stages in the D-DAQ system measured at different source to detector distances. In addition, the count rate from the analogue pulse counting system is shown.
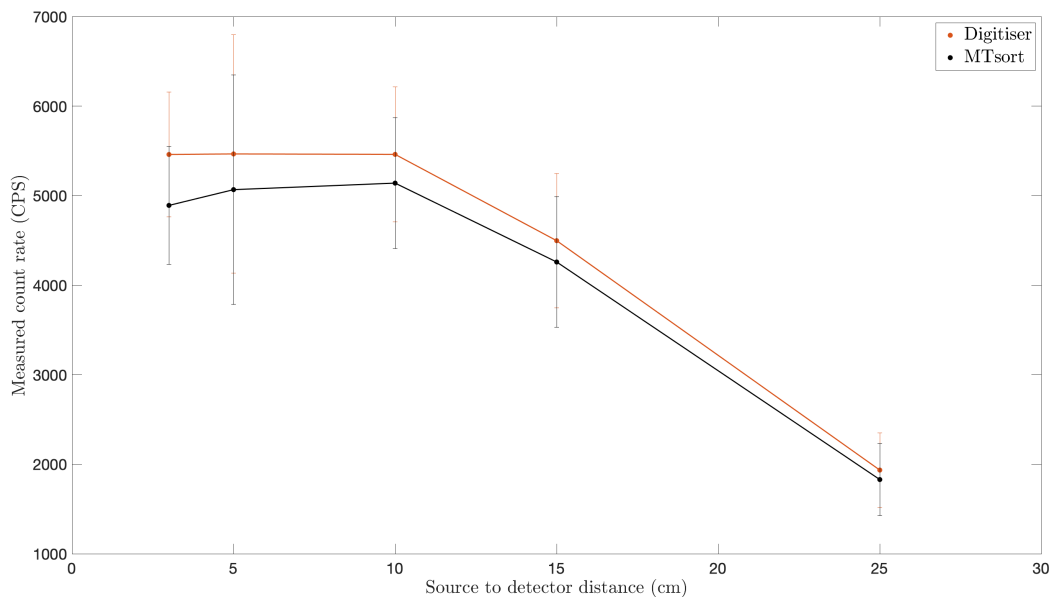


**Figure 6.16:** The count rate for Digitiser (stage 2) and MTsort (stage 3) in the D-DAQ system measured at different source to detector distances.

Figure 6.15 and 6.16 display the count rate at stage 2 and 3 for the D-DAQ at each source-detector distance. Figure 6.15 also includes stage 1 and the analogue pulse counting system. The number of triggers per second passed to the CAEN V1495 card (Trigger) increased as the source to detector distance decreased from 2k to 46k triggers per second as shown in Figure 6.15. The Trigger count rate is

shown as comparable to the count rate from the pulse count test in the previous section 6.2.1 which was increased as the source to detector distance decreased from 2k to 45k CPS. However, the count rate that is processed in the CAEN V1724 cards (Digitiser) and then extracted from the sorted data (MTsort) both increase as the source to detector distance decreased to 10 cm and thereafter did not increase further. The limited count rates for the Digitiser and sorted data (MTsort) as shown in Figure 6.16 were 5.4k and 5.1k CPS, respectively. This minor discrepancy between these two values can be attributed to the algorithm used in MTsort, however, the variation between these two values lies within the uncertainty value. These results show that the data loss occurs in the D-DAQ between stages 1 and 2, with only negligible data lost between stages 2 and 3.

The apparent data loss between stages 1 and 2 could be a consequence of the CAEN V1724 cards having reached their process capability such that they cannot process a higher count rate. Alternatively, it could be attributed to the time taken for the CAEN V1724 and the CAEN V1495 cards to pass and accept the initial trigger. It may also be that, due to a limited bandwidth between the cards, which results in the passage of only a limited amount of the data. If the issue is a consequence of limited bandwidth capacity, the count rate will be expected to scale linearly as the number of the channel used in the DAQ system is increased, given that the same bandwidth capacity will be divided across the number of channels used.

In the previous count rate investigations, only one channel was used. Therefore, given that the DAQ system has 48 channels, the effect of increasing the number of detector channels on the count rate in the Digitiser was investigated. The $^{137}$Cs source with activity of 6.9 MBq was placed 5 cm away from the scatterer detector and the number of detector channels written out was increased by using the web interface from the MIDAS software. The number of channels used were 1, 2, 8, 24 and 48 and the results are plotted in Figure 6.17.
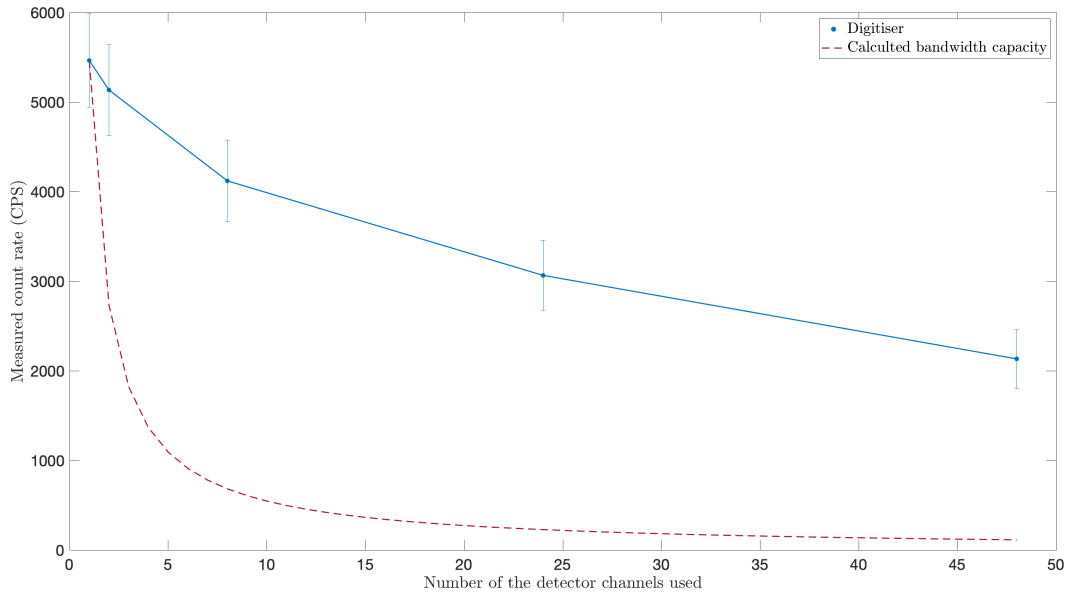
**Figure 6.17:** The count rate as a function of the number of the channels used in the digital acquisition system at a constant source to detector distance (blue line). The calculated bandwidth capacity response to increasing the number of channels (red dash line) is also shown.

It can be seen in Figure 6.17 that the count rate significantly decreased as the number of detector channels increased. The count rate when only one channel was used was 5.4k compared to 2.1k when 48 channels was used, as shown in Figure 6.17, corresponding to a 62% reduction in count rate. The maximum possible count rate that the Digitiser can process is 5.4k CPS, which is when only one channel was used. This bandwidth capacity of 5.4k CPS is divided by the number of channels used to show the response to increasing the number of channels is shown in Figure 6.17 as a red dash line. The manner in which the measured count rate decreased as the number of channels increased suggested that the issue was not a purely limited bandwidth capacity. Different combinations of the DAQ software settings have been examined, such as oscilloscope mode and baseline average window. Both settings reduce the throughput of the data in the digitiser. However, changing these settings did not solve the problem. An alternative, as suggested previously, may be that the CAEN V1724 and the CAEN V1495 cards took a long time to pass the initial trigger and receive the accepted trigger. It might be that the digitiser experienced a dead time due to the board memory being full [67]. It could be the CAEN V1724 card has a firmware or hardware issue that limits the capability of the card to process a high-count rate and write out the data. This issue cannot be fixed or further investigated in the university laboratory, so the developer company (CAEN) has been contacted regarding this issue.

### 6.2.3   The system performance for Compton imaging

In this section, the performance of the Gri+ for Compton imaging will be investigated, including the system count rate, the Compton imaging count rate, the imageable event rate and the peak-to-total ratio. The system count rate reports the event that passes the trigger criteria, whereas the Compton imaging count rate reports the event that passes the trigger criteria and has been validated by the BLD method to use in the imaging process. The imageable event rate reports the event that lies within the peak area of 661 keV from Compton addback spectra for fold 1 and 2 and 3-tier configuration event types. The peak-to-total ratio is the total count of the 661 keV peak in the DC addback energy spectrum divided by the total number of counts greater than 100 keV in the spectrum without applying fold gates.

In this section the Gri+ system is evaluated with all 48 channels of the D-DAQ system instrumented, which is operated in coincidence mode and with the output as all masked. The data were recorded when the Gri+ system was in 3-tier configuration. MIDAS version 7 and the D-DAQ system firmware version 4.19 were used in this experiment. The experiment used a $^{137}$Cs vial with an activity of 6.9 MBq which was placed at 3, 5, 10,15, 20 and 25 cm from the scatterer detector to examine the system ultimate data processing limit.
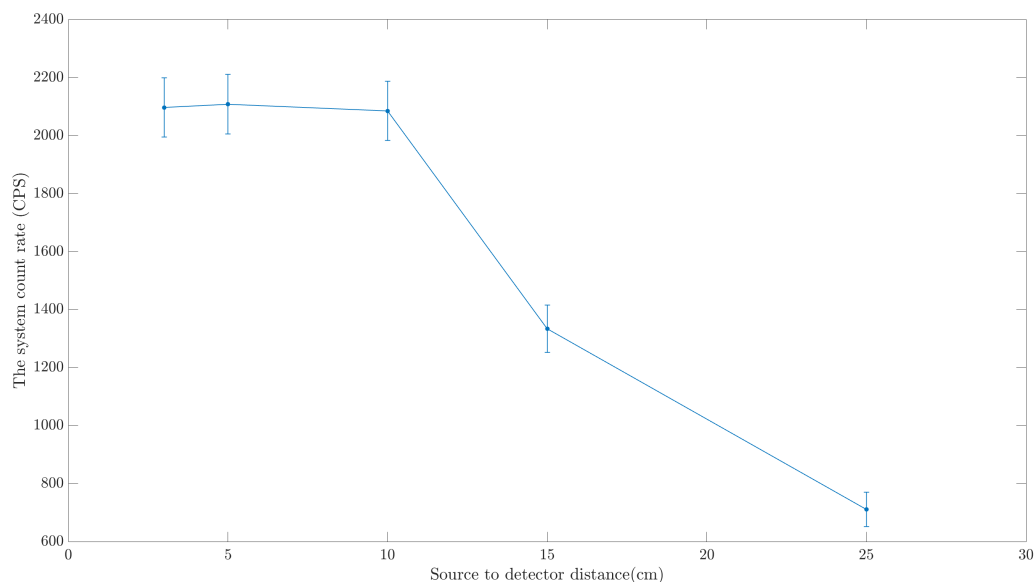


**Figure 6.18:** The system count rate for the digital acquisition system while operated in coincidence mode for Compton imaging at different source-to-detector distances.

The system count rate shows an increase with a decrease in the source-to-detector distance up to 10 cm, where the count rate appears to be saturated, as

shown in Figure 6.18. The maximum count rate is 2.1K CPS, which indicates the ultimate count rate capacity of the current D-DAQ for the Gri+ system.
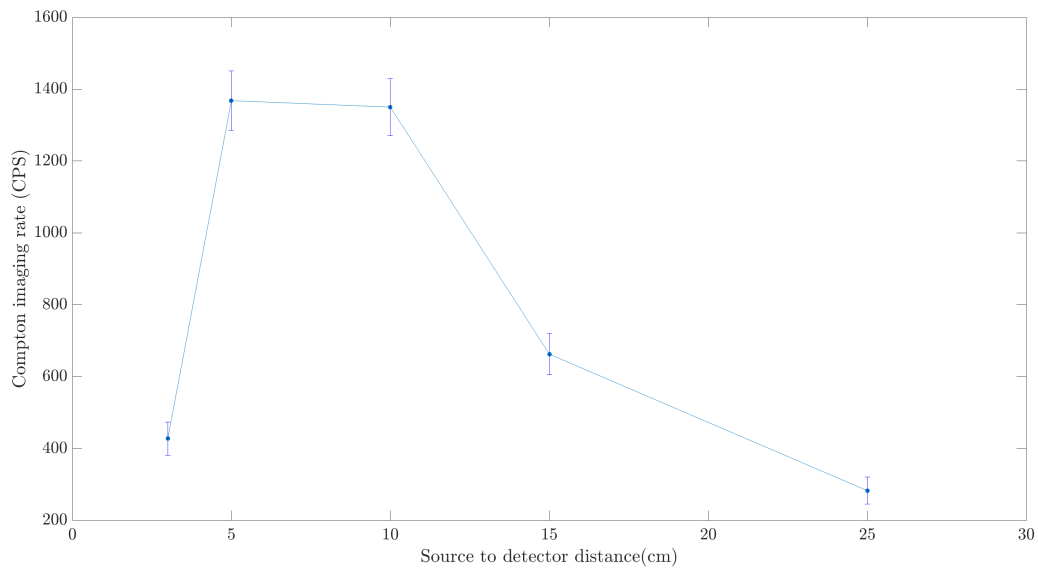


**Figure 6.19:** The Compton imaging count rate measured for the digital acquisition system while operated in coincidence mode for Compton imaging at different source-to-detector distances.

The Compton imaging rate increases as the source-to-detector distance decrease to 10 cm, and thereafter it appears to be saturated up to the source-to-detector distance of 5 cm. After that, the Compton imaging rate drops, as shown in Figure 6.19. It shows that the system exceeds its data processing ability and the Compton imaging rate is severely affects. The maximum Compton imaging rate that the Gri+ system can process is 1.4k CPS. By overlaying the true count rate from the previous section to this result, the system has optimum behaviour up to 11k CPS, and then the system has usable performance up to 29k CPS. The system data processing ability was severely affected at a true count rate of 49k CPS.
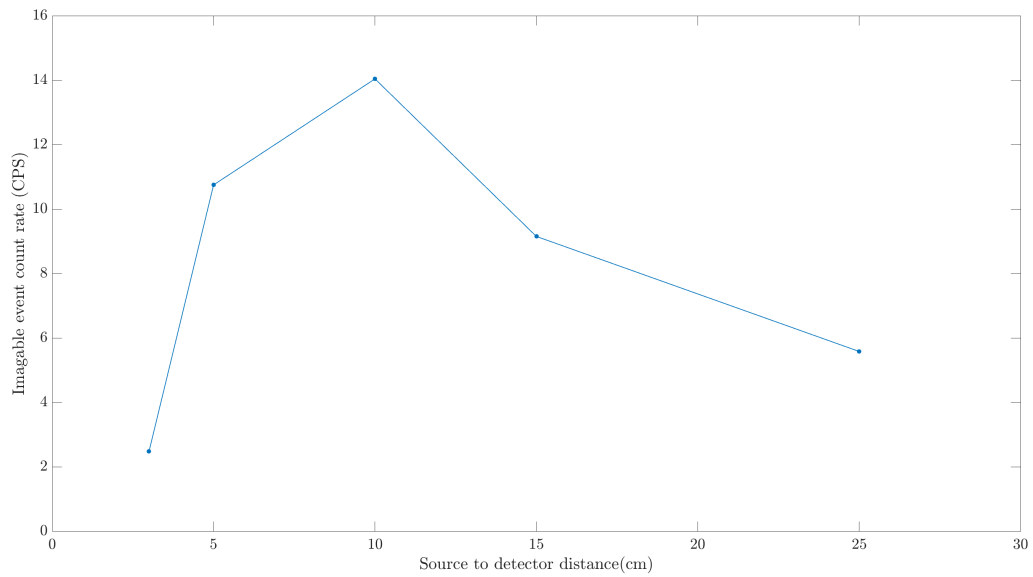
**Figure 6.20:** The imageable event rate for the datasets at different source-to-detector distances.
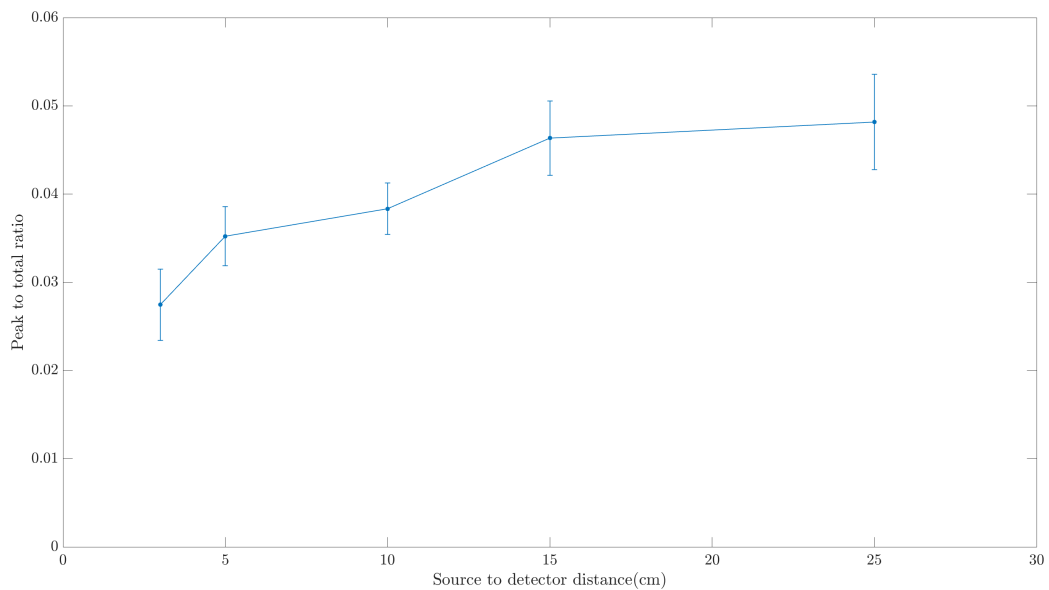


**Figure 6.21:** The peak to total ratio for the 661 keV peak at different source-to-detector distances.

The imageable event rate follows the increasing trends in the system and the Compton imaging rates up to the source to detector distance of 10 cm. After that, the imageable event rate sharply decreases, as shown in Figure 6.20. The discrepancy between the Compton imaging and the imageable event rates can be attributed to the system peak-to-total ratio behaviour. The peak-to-total ratio shows a slight decrease up to the source-to-detector distance of 15 cm; after that, it

shows a steady decrease up to 5 cm, then a sharp decrease, as shown in Figure 6.21. The peak-to-total ratio is in agreement with the previous investigation in Section 6.1.3, where the peak-to-total is decrease with increase the flux of radiation (count rate). The possible effect of the source-to-detector distance on the peak-to-total ratio for Compton camera system was not investigated in this work.

From this result, we conclude that there is a limited count rate for the D-DAQ system, irrespective of it being operated in coincidence or singles mode, which concurs with our earlier noted findings when using the 48 channels of the D-DAQ. In addition, there is a limited Compton imaging rate for the D-DAQ system when using the 48 channels of 1.4 CPS, and there is a critical situation where the system lost the ability to process the Compton imaging events at a true count rate of 49k CPS. The imageable event rate is severely affects when the system exceeds its data processing ability.

## 6.3   Summary

The system performance of the Gri+ when using a high activity phantom exhibits data loss when the phantom activity is greater than 2.9 MBq corresponding to Compton imaging rate of 411 CPS. As a consequence of the complex source shape and experiment setup, in addition to using a short half-life source, a further count rate investigation was undertaken with a simpler setup, and uniform source shape with a longer half-life. This investigation initiated by comparing the Gri+ system (D-DAQ) with analogue acquisition systems, which resulted in the identification of a significant data loss in D-DAQ system.

The D-DAQ system components were investigated, which firstly showed that the CAEN V1724 card (Digitiser) has a limited count rate capability. Next, exploring the effect of increasing the use channel number in D-DAQ system showed that the maximum count rate that the D-DAQ system can process decreases as the operational channel numbers increase.

Lastly, the system performance for Compton imaging shows that there is a limited count rate for the D-DAQ system of 2.1k CPS irrespective if the system is being operated in coincidence or singles mode. The maximum Compton imaging rate that the Gri+ system could process was 1.4k CPS. The Compton imaging rate at high activity phantom experiment in Section 6.1 was 411 CPS, and the subsequent investigation in Section 6.2 was 1.4k CPS. The discrepancy in the Compton imaging rate can be attributed to the use of different tier configurations and firmware. This conclude that the current DAQ system used in the Gri+ has a limited count rate capability and has critical situation where system data

processing ability was severely affected,resulting in limited capability to operated in the proton beam therapy.

Given that there is a huge amount of radiation in a proton therapy environment (about $10^9$ $\gamma$-ray emissions per second at 160 MeV proton beam energy). Clearly, the count limitation makes the current D-DAQ used in the Gri+ system unsuitable for dosimetric verification at proton therapy and highly possible to push the system to lose the ability to process the Compton imaging events. Collaboration with CAEN to restore the count losses will be essential before taking the Gri+ system to the Clatterbridge cancer centre for imaging measurement. This is an important recommendation of this thesis study.

# Chapter 7

# Spectrometry measurements at Clatterbridge Cancer Centre

It is important to understand the radiation present in the proton therapy environment to inform how the Gri+ system can operate there in the future. To this end, an experiment was conducted at proton therapy centre by members of the nuclear physics group in the University of Liverpool prior to this thesis. The work of this thesis was to analyse the data. The effect of using different targets, shield materials and detection angles will be analysed to determine the detection visibility of 4.44 MeV and 6.13 MeV gamma rays. This chapter begins with a brief introduction to the Proton Therapy facility. This is followed by the experiment setup and the methodology used in the spectrometry measurements. Then, the experiment result and dissection will be reported. Finally, the experiment limitation and future work will be outlined.

## 7.1 Introduction

The experiment was conducted at the National Centre for Eye Proton Therapy in the Clatterbridge Cancer Centre NHS foundation trust. This is one of a few dedicated proton therapy centres worldwide for eye tumours. The facility is operated at a low proton beam energy of 60 MeV with a maximum range of 31 mm in water [68]. The beam has superficial depth compared to higher proton beam energy, where the majority of proton therapy centres operate at higher energies (i.e. > 160 MeV). This experiment was conducted at low beam energy as the first step to understanding the radiation present in the proton therapy environment. Eventually, this experiment needs to be conducted at a broader range of proton energy. The focus of gamma analysis was on the most likely discrete PG from tissue by analysing the PG rays emitted from water and paraffin targets. The

characteristic 6.13 MeV PG emission from $^{16}$O and the 4.44 MeV PG emission from $^{12}$C during proton irradiation was used.

## 7.2  Experimental setup

Passive scattering proton beam produced by a MC62-P Scanditronix single-particle isochronous cyclotron with energy of 60 MeV was used [69]. A low beam intensity range of 0.075 nA to 0.13 nA was used and delivered doses of 0.99 to 1.26 Gy. The use of low intensity and relatively low dose compared to the clinical dose was due to the concern of a large amount of scattering radiation produced from the passive scatter beam line elements in these first measurements.

Two detectors were used, one for gamma spectroscopy and the other for neutron counting namely: a HPGe detector (trans-SPEC-DX-100T developed by ORTEC) and 3-helium detector for neutrons. Both detectors were aligned with the beam axis using supported materials and placed at different angles from that axis as shown in Figure 7.1. Analysis of the neutron data was not undertaken because it was a preliminary dataset, and it was taken for a basic measurement assay.



**Figure 7.1:** Photograph of the treatment room. The HPGe detector and the 3-helium detector were aligned with the beam axis using supported materials and placed at different angles from the beam axis.

The HPGe detector was calibrated by using two-point sources ($^{22}$Na and $^{60}$Co) before and after the experiment to make sure there is no change in the detector

gain throughout the experiment. In addition, each dataset has been individually calibrated by using visible gamma lines originating in the detector material (0.140 MeV from $^{75}$Ge), support structure (1.014 MeV from $^{27}$Al), and beamline element (0.847 and 1.038 MeV from $^{56}$Fe). Figure 7.2 shows a schematic diagram for the experiment setup where all the detectors were placed at the forward angles from the beam axis. Detailed information about the detection angles, the distance between the detector and the irradiated target, beam intensity and the delivered dose as reported by the system dose monitor are shown in Table 7.1.
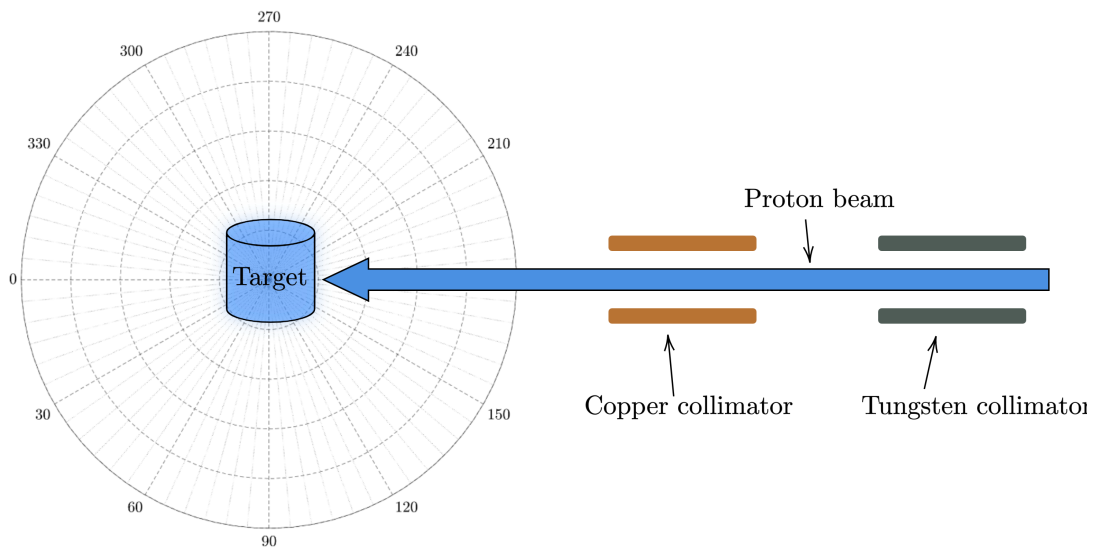


**Figure 7.2:** A schematic diagram for the experiment setup shows the detection angle with respect to the beam axis for the HPGe detector and the 3He detector.

**Table 7.1:** The detection angle, the detector to irradiated target distance, the beam intensity, and the delivered dose during the experiment for the HPGe detector.

| Detection angle (°) | Distance (cm) | Water target | | Paraffin target | |
|---|---|---|---|---|---|
| | | Beam intensity (nA) | Dose (Gy) | Beam intensity (nA) | Dose (Gy) |
| 8 | 42 | 0.092 | 1.26 | 0.086 | 1.17 |
| 33 | 43 | 0.088 | 1.17 | 0.083 | 1.17 |
| 71 | 35 | 0.08 | 1.08 | 0.08 | 1.08 |
| 90 | 136 | 0.075 | 0.99 | 0.075 | 0.99 |

A plastic beaker with a diameter and height of 16 cm and 19 cm respectively was filled with two litres of water and a paraffin cylinder ($C_nH_{2n+2}$) with a diameter and height of 10 cm and 19 cm respectively were used in the experiment as targets. The targets were aligned with the beam axis and placed 19 cm from upstream at the end nozzle, where the maximum range of proton beam in the water reported by [69] to be 3.1 cm. The shielding materials that have been used were lead with 5 cm of thickness and wax with 6 cm of thickness to reduce the amount of

neutrons reaching the detector. The gamma spectrum from the HPGe detector was taken across 16k channels. The spectra were rebinned because of the statistical fluctuation. The gamma spectrum was analysed by a least-squares peak-fitting program called GF3 [70], which is designed primarily to analyse the gamma-ray spectra from HPGe detectors. The HPGe detector experienced extremely high dead time during this experiment, which led to significant potential systematic errors in the data. Throughout the experiment, the HPGe detector dead time was extracted directly from MAESTRO software, as shown in Figure 7.3. It can be seen that across all measurements, the detector experienced between 50% and 90% dead time.
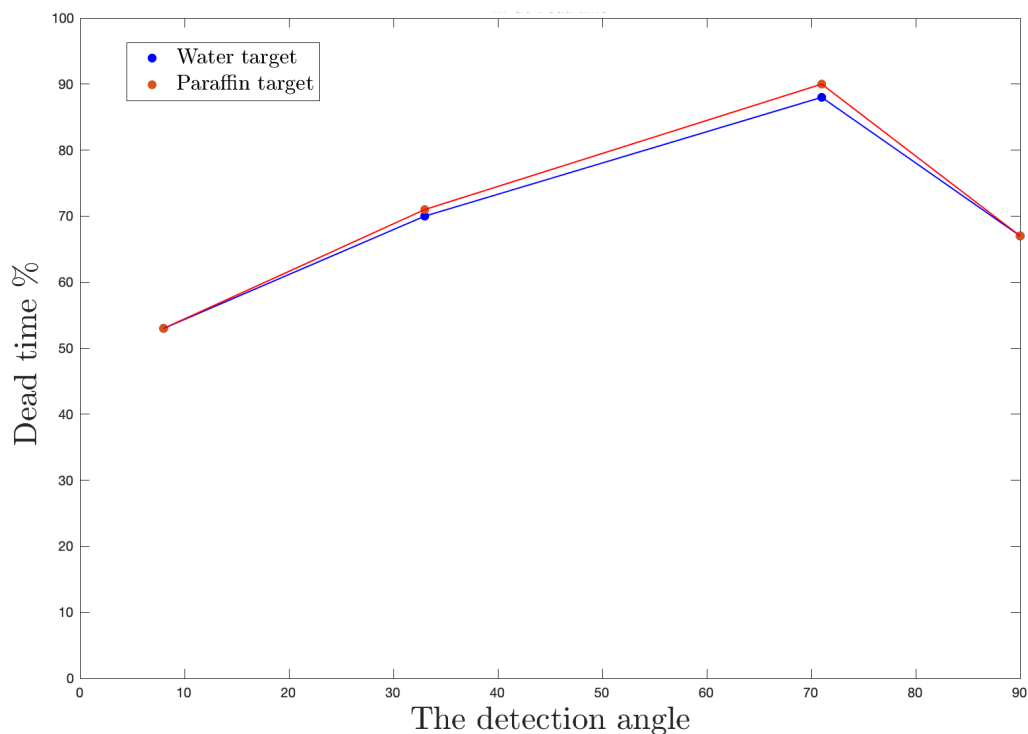


**Figure 7.3:** The HPGe detector dead time recorded through the experiment for water and paraffin targets.

As shown in Table 7.1, the experiment datasets were not conducted in a systematic way. The datasets have a different distance between the detector and the irradiated target. This variation in the distance will result in a variation in the gamma detection as the radiation intensity is inversely proportional to the square of the distance (the inverse square law). A range of different beam intensities was used in the experiment, which resulted in different times needed to deliver the dedicated dose. In addition, the variation in the delivered doses will result in the variation in protons delivered. Therefore, the prompt gamma emits will be affected. These datasets need to be correct to make them comparable.

For gamma spectroscopy measurements, the datasets have been corrected by dividing the datasets counts by the measurement live-time to obtain the count rate and then divided by the value of 511 keV for each dataset. Using 511 keV (positron annihilation) was suggested because of its isotropic emissions and has been used to measure the delivered dose by positron emission tomography (PET) [9]. In addition, 511 keV is a constant factor that is subject to all other variations in the experiment setup, such as target to detector distance, detector dead-time and the delivered dose.

## 7.3 Result and discussion

### 7.3.1 Gamma-ray energy spectra

The gamma ray spectra measured for the irradiated water target and paraffin target are shown in Figure 7.4. For the water target, the expected PG ray 6.13 MeV from $^{16}$O as well as the single and double escape peaks at 5.61 and 5.11 MeV respectively were clearly visible. While the 4.4 MeV emitted from $^{12}$C have been observed only at detection angles of 8° with low intensity. For the paraffin target, the expected PG ray 4.4 MeV emitted from $^{12}$C have been identified for all detection angles apart from the experiment at 90°. However, its single and double escape peaks at 3.9 MeV and 3.4 MeV respectively were only identified at detection angles of 8° and 33° due to the high background radiation. All paraffin target datasets demonstrated some PG from $^{16}$O and some water target datasets demonstrated some PG from $^{12}$C which are observed with weak intensity. It was believed such case occurred because of oxygen present in the air in addition to PMMA ($C_5O_2H_8$) which was used as a range modulation in the beamline.

**Figure 7.4:** Gamma ray spectrum from HPGe detector for water and paraffin targets irradiated by a 60 MeV beam energy. Detection angle was 8° from the beam axis.

Interestingly, a gamma line with a sharp peak at 4.422 MeV was present in all the irradiated targets spectra. However, another broad peak of 4.460 MeV was only present in paraffin target spectra as shown in Figure 7.5, where the centroid of this peak was changed as a function of detection angle. The sharp gamma line was emitted after nuclear interaction between the protons with a stationary nucleus. However, the broad gamma line was emitted after nuclear interaction between protons with a recoiling nucleus in flight, resulting in Doppler broadening. In terms of 4.4 MeV from the $^{12}$C, most of the protons have nuclear interaction with the recoiling carbon nucleus, thus most of the decay happened in flight which resulted in the Doppler broadening [11]. Such occurrence suggests that the origin of the broad peak is the prompt gamma line from $^{12}$C while the origin of the gamma line with a sharp peak is unknown. This peak was reported by published work about the gamma-ray production by proton-induced reactions on $^{12}$C and $^{16}$O by [71].
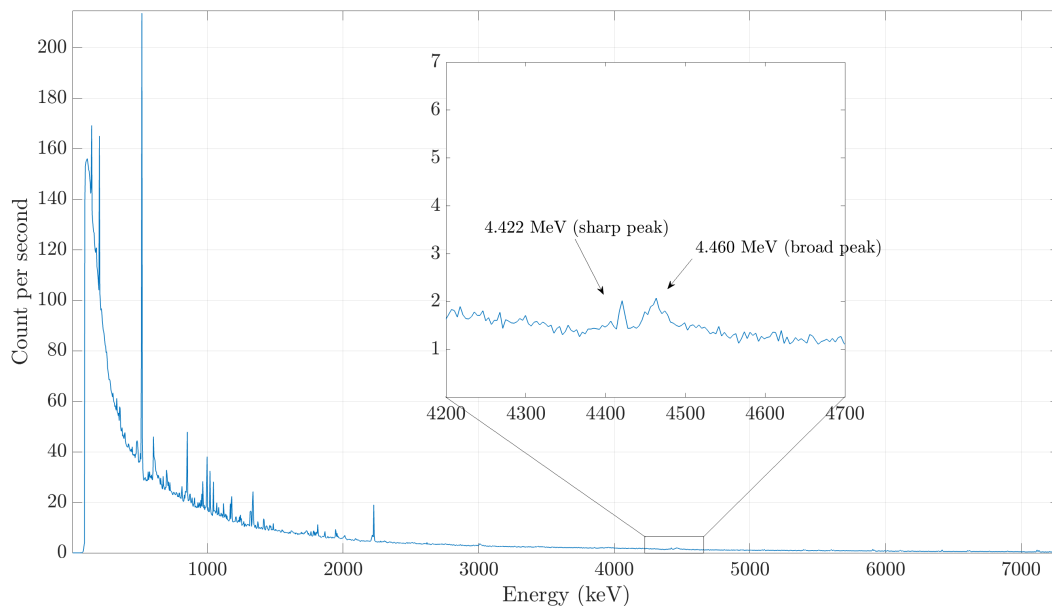
**Figure 7.5:** The sharp peak at 4.422 MeV and broad peak of 4.460 MeV are clearly shown in the spectrum. This spectrum from HPGe detector for paraffin targets irradiated by a 60 MeV beam energy. Detection angle was 8° from the beam axis.

In both spectra, some other PGs were emitted from isotopes that were created due to the interactions between protons or secondary neutrons and elemental nuclei of these materials, resulting in one or more nucleons being ejected and producing an isotope in an excited state decays through the emission of a gamma-ray of different energy. The origin of these PG rays was from a detector material (0.140 MeV from $^{75}$Ge), support structure (1.014 MeV from $^{27}$Al), and beamline element (0.847 and 1.038 MeV from $^{56}$Fe) and (6.618 MeV from $^{64}$Cu). Another gamma line of 2.2 MeV was also present in both spectra as a result of neutron being captured by hydrogen. In addition, a strong peak of 511 keV was present in the measured spectrum for both irradiated targets. This arises from the positron annihilation as a result of beta decay of short-lived oxygen and carbon isotopes during the proton irradiation as shown in Figure 7.6.
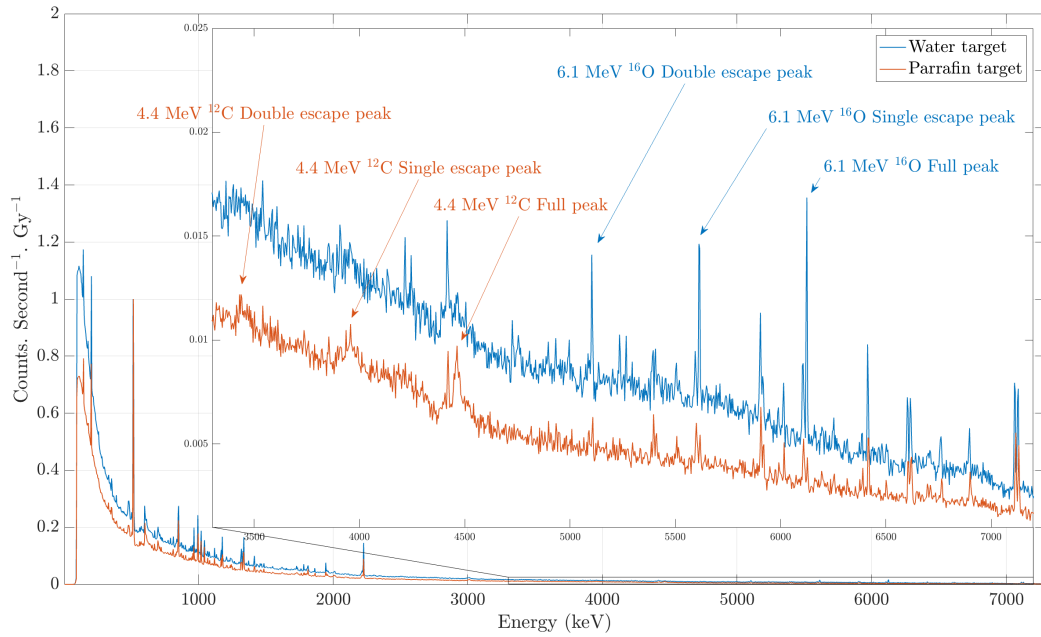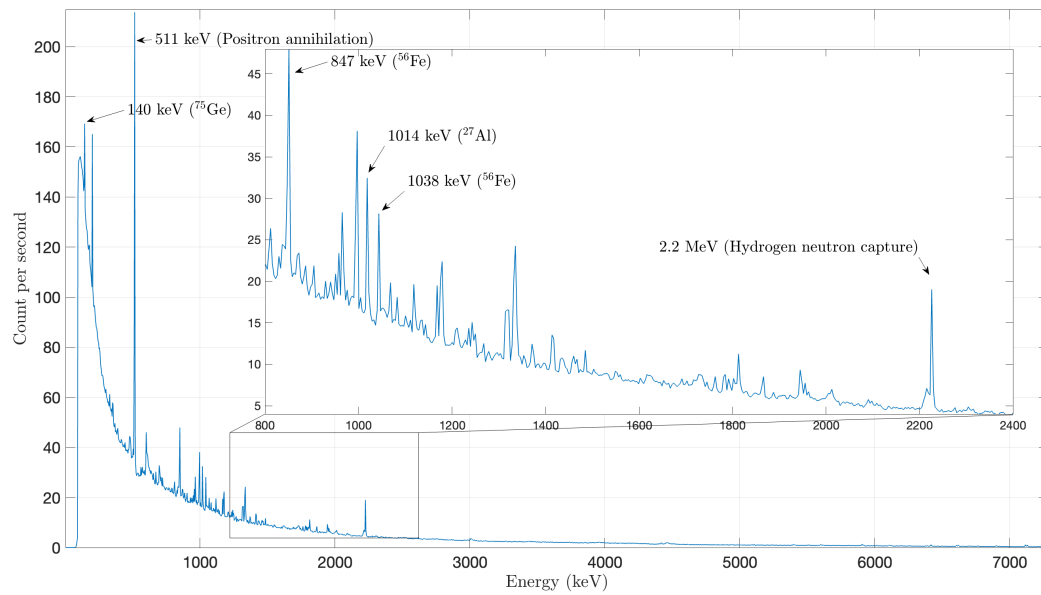
**Figure 7.6:** Gamma ray spectrum from HPGe detector for paraffin targets irradiated by a 60 MeV beam energy. Detection angle was 8° from the beam axis.

## 7.3.2   Angular distribution

In this section, the angular distribution of both 4.4 MeV and 6.1 MeV will be discussed. As it discussed early in Section 7.2, the data was corrected and these corrections only allowed to compare the data to each other. The following result will shows the normalised count rate of the interesting gamma lines as a function of the detection angle.

**Figure 7.7:** Gamma ray spectrum from HPGe detector for water targets irradiated by a 60 MeV beam energy. The spectra is zoomed into the 4.4 MeV region where the 4.4 MeV gamma line was not visible.



**Figure 7.8:** Gamma ray spectrum from HPGe detector for paraffin targets irradiated by a 60 MeV beam energy. The spectra is zoomed into the 4.4 MeV region to illustrate that the 4.4 MeV gamma line was not visible when the detection angle was only at 90°.

**Figure 7.9:** The 4.44 MeV gamma line count rate as function of detection angle for paraffin targets. The 4.44 MeV gamma line was not visible at a detection angle of 90°.

The 4.4 MeV gamma line was not visible for the water target dataset, as shown in Figure 7.7. In contrast, for the paraffin target dataset, the 4.4 MeV gamma line was not visible when the detection angle was only at 90°, as shown in Figure 7.8. This might be due to the detector being placed at 136 cm from the irradiated target and the lowest dose was delivered at this angle, as shown in Table 7.1. However, the count rate was increased when the detector was moved away from a 90° detection position toward forwarding detection angle, as shown in Figure 7.9. This result shows that 33° was the best detection position for the 4.4 MeV gamma line.
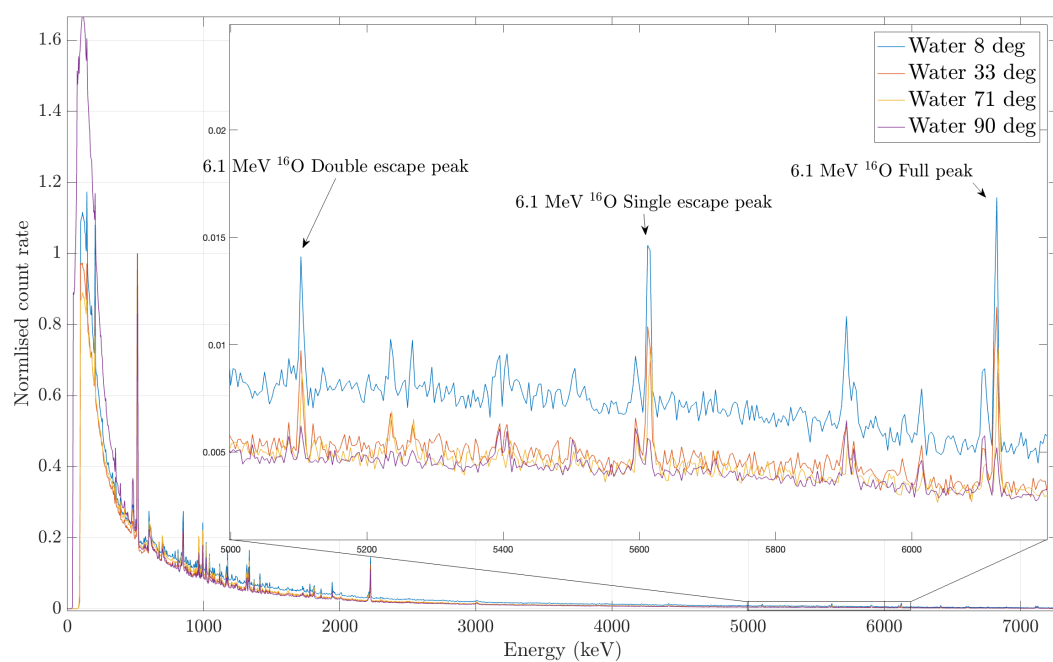
**Figure 7.10:** Gamma ray spectrum from HPGe detector for water targets irradiated by a 60 MeV beam energy. The spectra is zoomed into the 6.1 MeV region where the 6.1 MeV gamma line was visible for all detection angles.
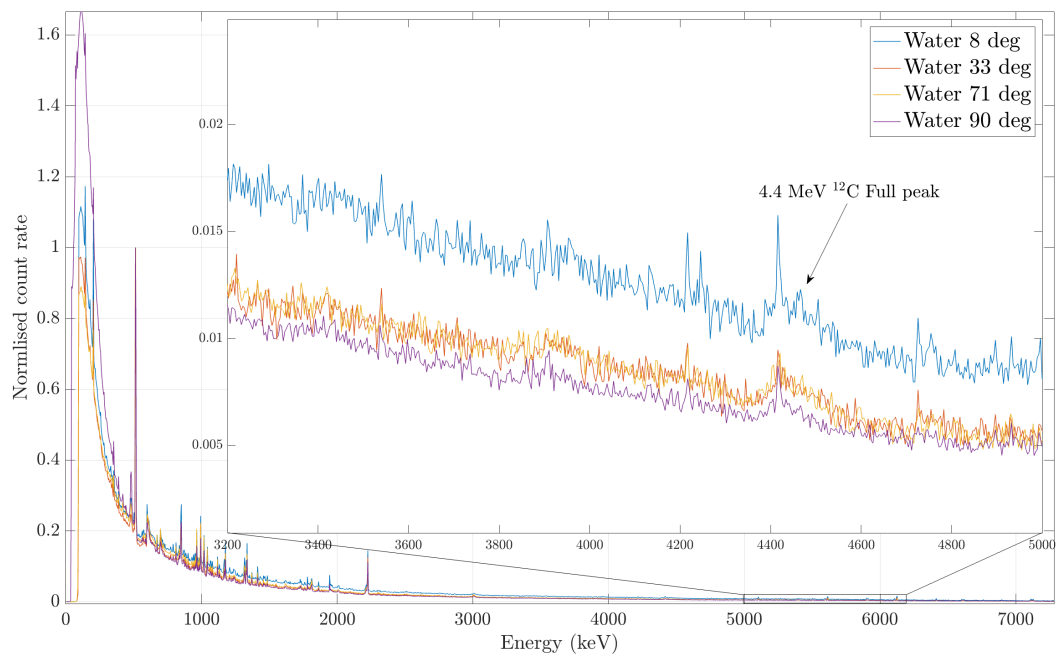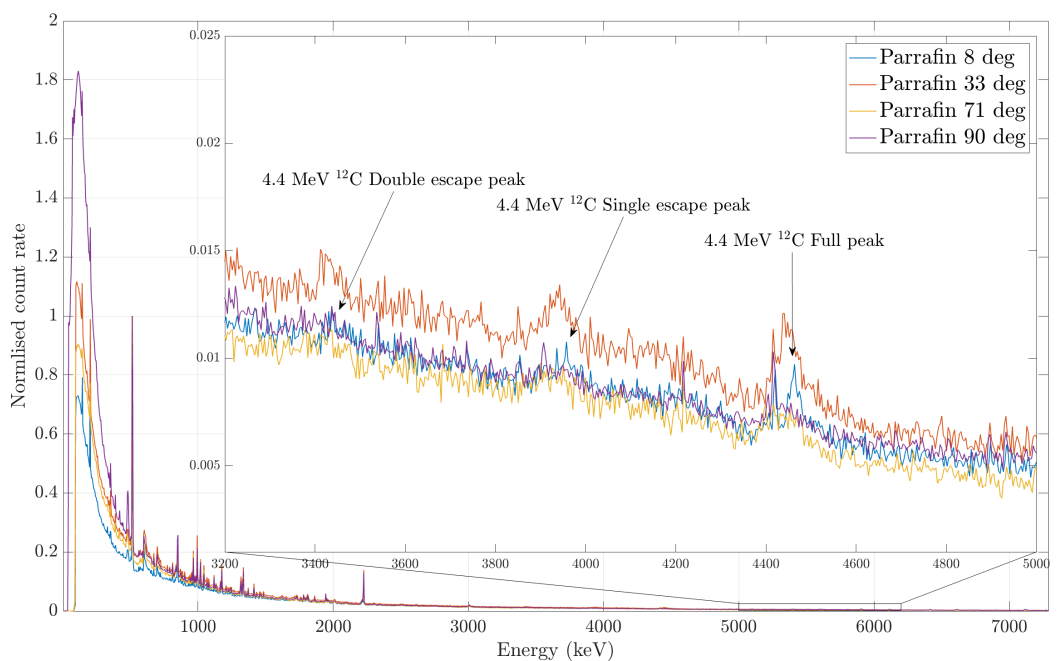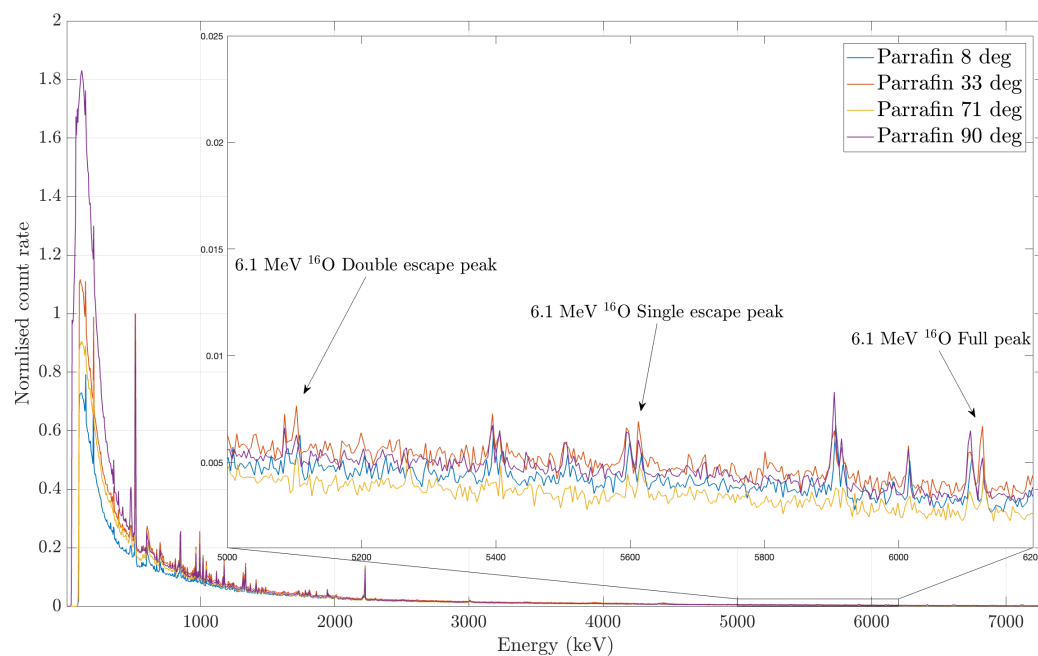


**Figure 7.11:** Gamma ray spectrum from HPGe detector for paraffin targets irradiated by a 60 MeV beam energy. The spectra is zoomed into the 6.1 MeV region where the 6.1 MeV gamma line was visible for all detection angles.
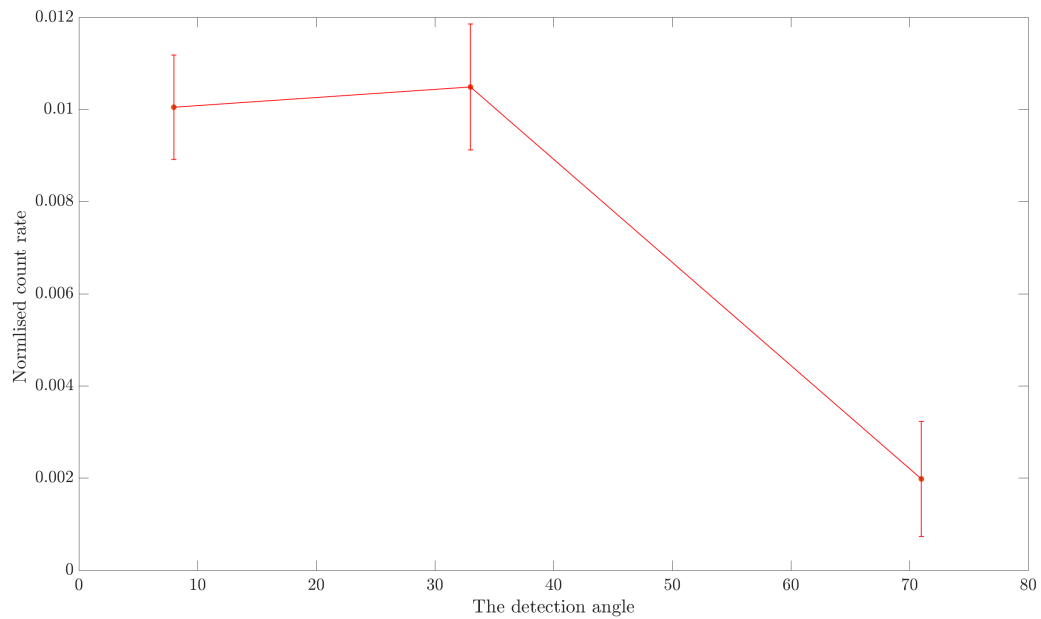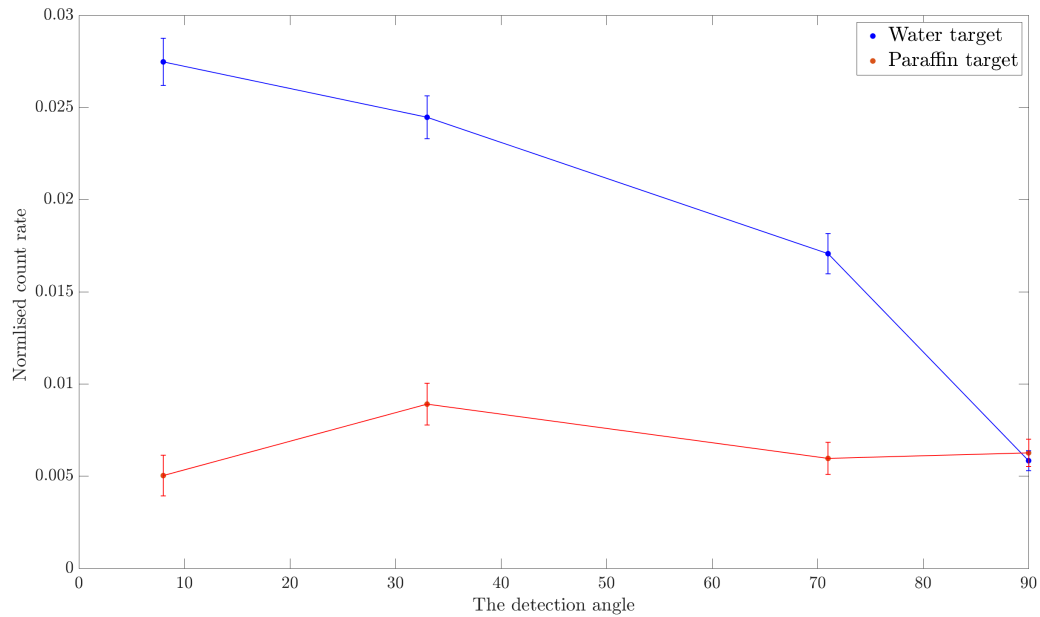
**Figure 7.12:** The 6.129 MeV gamma line count rate as function of detection angle for water and paraffin targets.

The 6.13 MeV gamma line was visible at both the water and paraffin target datasets for all detection angles, as shown in Figure 7.10 and 7.11. However, the 6.13 MeV was a very low count rate for paraffin target datasets. On average, the count rate of the 6.13 MeV gamma line at all the water target datasets were about 1.5 to 2.5 times greater than in the paraffin target datasets for all detection angles apart from detection at 90 degrees. There were very small differences in the 6.13 MeV gamma line count rate for the water and paraffin target datasets at this detection angle, as shown in Figures 7.12. It might be because the detector was placed 136 cm from the irradiated target, and the delivered dose was low at this angle which might affect the detection of the 6.13 MeV gamma line in a similar manner that affects the detection of the 4.4 MeV gamma line at the paraffin target. This might suggest that the origin of this gamma line was not from the interaction of proton with the water target material. The water target datasets have a larger component of the 6.1 MeV gamma line which clearly demonstrate the material composition of oxygen in the water. The count rate was increased when the detector was moved away from a 90° detection position toward forwarding detection angle, as shown in Figure 7.12. This result shows that 8° was the best detection position for the 6.1 MeV gamma line.

Overall, a firm conclusion was not possible. However, the most likely explanation was reported. The result was, to some extent was, in accordance with the gamma-ray production as a function of the angle detection that published by [16], as shown in Figure 2.6. The result demonstrated that the detection of the 4.4 MeV

and 6.13 MeV prompt gamma rays was angular dependent, and using a shallow angle to measure these gamma lines is recommended.

### 7.3.3 Shielding effects
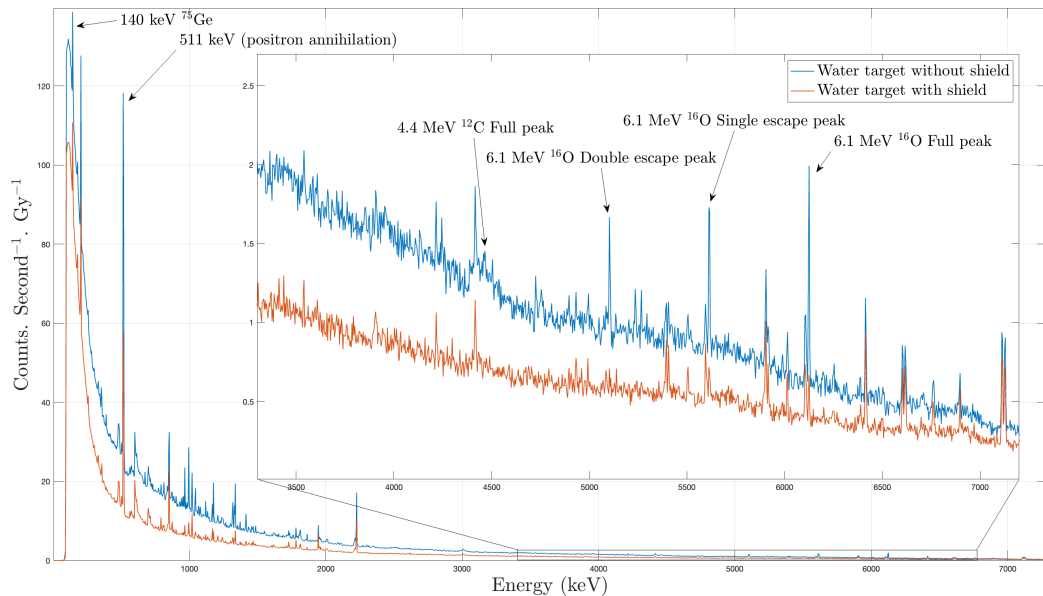


**Figure 7.13:** Gamma spectrum from HPGe detector for water target (with and without shielding material) at 60 MeV proton beam energy and detection angle was 8 degree from the beam axis.

Using an effective shield will benefit from decreasing the background radiations and number of the secondary neutron reach the detector in addition spared the interested gamma-ray. The following discussion will show the result from using shielding material for one setup as it was the only available data from this experiment campaign. Figure 7.13 demonstrates two spectra were measured during the irradiated water target with and without shielding material. The shielding material used was 5 cm of lead and 6 cm of paraffin wax. The shielding material was placed in close proximity to the water target between the detector and the irradiated target. The use of lead and paraffin wax shielding have resulted in the Compton continuum in the spectrum being reduced as shown in Figure 7.13, as well as the other background PGs has reduced such as the 140 keV, which was emitted from the interactions between secondary neutrons and the germanium detector. It was reduced by about 20 %. However, it may be that the lead shielding was placed in close proximity to the irradiated target and only attenuated (or scattered away) the PGs ray emitted from the target and spared the background PGs. The result demonstrates that using shielding in this setup reduces the de-

tector dead time by 17% as well as the neutron interactions with the detector in addition to reducing the detection of the 6.13 MeV gamma ray.

## 7.4   Summary

It is not possible to report a firm conclusion from the spectroscopy measurement in the Clatterbridge Cancer Centre because the experiment was not conducted systematically. However, the most likely explanation was reported. The 6.13 MeV gamma line from $^{16}$O and the single and double peaks at 5.61 and 5.11 MeV, respectively, are visible for the water target. The 4.4 MeV gamma line emitted from $^{12}$C has been identified for all detection angles apart from the experiment at 90° for the paraffin target. However, its single and double escape peaks at 3.9 MeV and 3.4 MeV respectively were only identified at detection angles of 8° and 33°. The result showed that the detection of the 4.4 MeV and 6.13 MeV were angular dependent which is roughly in agreement with the publication. Using a relatively shallow angle to measure these gamma lines is recommended.

The effect of using shielding material has been investigated for one setup as it was the only available data from this experiment campaign. Lead and paraffin wax shielding were used, which resulted in reducing the Compton continuum in the spectrum as well as the 6.13 MeV gamma line. The other background PGs were not affected apart from 140 keV, which was emitted from the interactions between secondary neutrons and the germanium detector, and was reduced by about 19%. The setup of the shielding material requires more investigations in order to determine the best possible setup. In this experiment, the HPGe detector experienced extremely high dead time, which led to significant potential systematic errors in the data.

## 7.5   Experiment challenges and limitations

There were several uncertainties in this investigation. Firstly, the detector to irradiate target distance was varied for some of the detection angles for the HPGe detector where gamma-ray detection is distance dependant. In addition, the HPGe detector has experienced a huge dead time of up to 90%. Another major source of uncertainty was that the delivered dose and the proton beam intensity were varied for some of the detection angles where the number of protons produced were affected by these parameters; thus, the production of the PGs ray will be affected. Further data collection is required to determine the optimum detection angle and a suitable shielding design that can be used with the Gri+ system.

There was an agreement with the Clatterbridge Cancer Centre to conduct

another experiment in May 2020. To prepare for this experiment, the HPGe detector dead time was evaluated in the university laboratory and reduced from 90% to about 50% for high count rate. Irradiated targets were prepared to be used in the experiment with different concentration of carbon and oxygen. The experiment plan was set and agreed with my supervisors and the Clatterbridge Cancer Centre team. However, due to the COVID-19 pandemic, the NHS was being overwhelmed, and I did not have access to the facility as of writing of this chapter.

# Chapter 8

# Conclusion and Future Work

## 8.1 Conclusion

This thesis determined the potential imaging capabilities of the Gri+ system for prompt gamma rays during proton therapy. The Gri+ system was evaluated in a setting that approximated the proton radiotherapy environment. This was achieved by using high-energy gamma-ray radioactive source emitters and high-activity radioactive sources. This was followed by spectroscopy measurements at the proton therapy facility to determine the best detection position for the Gri+ system for future in situ evaluations.

**High energy gamma-ray radioactive sources emitters**

The energy spectra analysis for the 1.8 MeV gamma ray emitted from $^{88}$Y revealed that about 55% of the $\gamma$-ray experienced a narrow scattering angle. This analysis presented a technique for predicting the system response. Then, the geometrical setup and system parameters for measuring higher gamma rays, including the 4.4 MeV and 6.1 MeV $\gamma$-rays during proton therapy, were optimised. This was achieved using a calculated method and was then validated with the experimental results.

The fold level increased with increases in the incoming gamma energy, where the Fold 2 event was $\sim$50% and Fold 3 was $\sim$27% at 1.8 MeV gamma energy. Using a Fold 2 event significantly increased the Gri+ system imaging efficiency from $\sim$ 27% to 70% for all events registered in the system at 1.8 MeV gamma energy ($^{88}$Y). For prompt gamma-ray imaging during proton therapy, Fold 2 will therefore significantly influence Compton imaging efficiency.

Using an online analysis algorithm showed that including the Fold 2 event greatly degraded the image resolution. This was in contrast to using an offline analysis algorithm, which demonstrated superior image resolution across all Fold

categories. However, computational costs and time limitations are potential limitations to implementing offline analysis in clinical situations, unless acceleration methods are employed. The Gri+ system successfully imaged the high-energy gamma ray from $^{88}$Y (1.8 MeV). The best achievable image resolution was 7.2 $\pm$ 0.6 mm and 10.5 $\pm$ 0.8 mm for Fold 1 and all fold events, respectively. This was achieved using the offline analysis algorithm and the $16^{th}$ iteration of the MLEM reconstruction code.

The trade-off between image resolution and Compton image efficiency by including Fold 2 events in imaging is a challenge. Using an offline analysis algorithm might be a good solution. However, this algorithm requires further development to mitigate computational costs and time limitations. In addition, developments are need to integrate this algorithm into MTsort to be an online analysis algorithm.

The current Gri+ system setup has a limited energy processing capability of up to 3.1 MeV because of the gain used in the GO box. To image the prompt gamma rays of 4.4 MeV and 6.1 MeV during proton therapy, the D-DAQ must be set up without using the GO box or a GO box with a gain factor of 1X. For high gamma-ray energy greater than 1.4 MeV, the AC side energy is recommended for imaging the 2-tier event instead of the DC side energy, and the DC side energy should be used to image the 3-tier event. The superior AC side energy resolution of the first absorber detector at high-energy gamma rays contributes to the Compton image resolution.

**High activity radioactive sources**

The Gri+ performance using a high-activity phantom showed a significant loss of data. As a consequence of the complex source shape and experimental setup, in addition to using a short half-life source, a further count rate investigation using a long half-life uniform-shaped source was conducted. This investigation concluded that the CAEN V1724 card (Digitiser) had a limited count rate capability of 5.1k when operating using one channel. The count rate processing capability decreased as the number of operational channels increased to be 2.1k when operating using 48 channels irrespective if the system is being operated in coincidence or singles mode. The maximum Compton imaging rate that the Gri+ system could process is 1.4k CPS and there is a critical situation where the system lost the ability to process the Compton imaging events at a true count rate of 49k CPS.

It could not be concluded whether the CAEN V1724 card had a firmware or hardware issue that limited the capability of the card to process a high count rate, so the developer company (CAEN) was contacted regarding this issue. The count rate issue makes the current D-DAQ used in the Gri+ system unsuitable for

dosimetric verification in proton therapy, and is highly possible that the system will be pushed to lose its ability to process Compton imaging events. It is essential to restore the count losses before taking the Gri+ system to the Clatterbridge Cancer Centre for imaging measurements.

**Spectroscopy measurements at proton therapy facility**

The spectroscopy measurements in the Clatterbridge Cancer Centre were not conducted systematically. It is not possible to report a firm conclusion from this experiment; instead, the most likely explanation was reported. The results showed that the detection of 4.4 MeV and 6.13 MeV was angular dependent, roughly agreeing with prior publications. Using a relatively shallow angle to measure these gamma lines is recommended which made it the best position for the Gri+ system to detect prompt gamma rays. The setup of the shielding material requires further investigation to determine the best possible setup. Given the experimental uncertainties and the huge dead time for the HPGe detector, further data collection is required.

## 8.2 Limitations and challenges

Some of this work is limited to the current geometry of Compton camera. This might have influenced the range of the energy deposited in each detector, the Compton image efficiency and the Compton image resolution. This work did not investigate system detection efficiency, which is an important aspect, especially for high-energy gamma rays, where detection efficiency is a challenge that must be overcome. This is because the firmware issue prevents the extraction of the necessary information.

There was an agreement with the Clatterbridge Cancer Centre to conduct another spectroscopy measurement in May 2020. The experiment plan was set and agreed upon with my supervisors and the Clatterbridge Cancer Centre team. However, due to the COVID-19 pandemic, the NHS was overwhelmed, and I could not obtain access to the facility. Since then, my progress has been severely hampered by COVID restrictions. Due to local and national lockdown restrictions, there has been very limited access to campus facilities, specifically the radiation detector laboratory. For several months, I was not able to access the facilities at all, and then there was a staged reopening of the lab to ensure compliance with social distancing measures. During the staged reopening, I was able to attend on certain days, according to risk assessments. In addition, the research-grade equipment needed for this thesis had to be sent back to the manufacturer for

repair in March 2020, and it was not returned until March 2021.

## 8.3   Future Work

Due to the scope of this thesis and the limited time available during the PhD, some aspects need further investigation and improvement. This would contribute to achieving optimum performance of the Gri+ system to imaging the prompt gamma rays during the proton therapy. Some of these aspects are discussed below.

- Future research should expand the offline analysis (database PSA) to include the scatterer detector. This could improve the image resolution and increase the Compton imaging efficiency by including a Fold 2 event. This can be achieved in a similar manner as reference [52]. First, the detector response needs to be experimentally characterised as a function of position and simulate the detector's signal for each position within the detector volume and subsequent validation at selected points.

- The offline analysis (database PSA) should be improved to overcome computational costs and consumable time. This might be achieved by using other programming languages, such as Python, and acceleration methods, such as GPU in addition to integrate this algorithm into MTsort to be an online analysis algorithm.

- The effect of the detector's separation on the Compton image efficiency and the Compton image resolution should be experimentally evaluated. For the Compton image efficiency, a minimum detector separation is recommended to maximise Compton image efficiency for detection the low energy gamma ray. This is because the maximum possible scattering angle increase by decreasing the detector's separation and the low energy gamma ray tend to experience a wide scattering angle. However, for high-energy gamma rays, the gamma rays experience a narrow scattering angle where the detector separation might not affect the Compton image efficiency. For the Compton image resolution, increasing the detector separation might decrease the affect of the angular uncertainties on the Compton image resolution as suggested by [72].

- The trigger map and energy threshold should be optimised to produce an energy window that can be used to select the energy range. This could potentially reduce the count rate throughput of the D-DAQ and eventually mitigate the high count rate challenge.

- Conduct spectroscopy measurements at the proton therapy facility in a systematic way. It is recommended to focus on the shallow angles (0° to 70°) to measure the PG rays. It is also essential to explore the neutron density map in the proton treatment room where the high energy and thermal neutron will be present. This will help determine the best detection angle for PG rays and the lowest neutron background.

# Bibliography

[1] T. I. Yock and N. J. Tarbell, "Technology insight: Proton beam radiotherapy for treatment in pediatric brain tumors," *Nature Clinical Practice Oncology*, vol. 1, no. 2, pp. 97–103, 2004, ISSN: 17434254. DOI: 10.1038/ncponc0090.

[2] W. D. Newhauser and R. Zhang, "The physics of proton therapy," *Physics in Medicine and Biology*, vol. 60, no. 8, R155–R209, 2015, ISSN: 13616560. DOI: 10.1088/0031-9155/60/8/R155.

[3] H. A. Bethe, "Molière's Theory of Multiple Scattering," *Physical Review*, vol. 89, no. 6, pp. 1256–1266, Mar. 1953. DOI: 10.1103/PhysRev.89.1256.

[4] S. Yajnik, *Proton beam therapy: How protons are revolutionizing cancer treatment.* 2013, pp. 1–117, ISBN: 9781461452980. DOI: 10.1007/978-1-4614-5298-0.

[5] A. C. Knopf and A. Lomax, "In vivo proton range verification: a review," *Phys. Med. Biol*, vol. 58, no. 15, pp. 131–160, 2013, ISSN: 0031-9155. DOI: 10.1088/0031-9155/58/15/R131.

[6] E. J. Tryggestad, W. Liu, M. D. Pepin, C. L. Hallemeier, and T. T. Sio, "Managing treatment-related uncertainties in proton beam radiotherapy for gastrointestinal cancers," *Journal of Gastrointestinal Oncology*, vol. 11, no. 1, pp. 212–224, 2020, ISSN: 2219679X. DOI: 10.21037/jgo.2019.11.07.

[7] H. Paganetti, "Range uncertainties in proton therapy and the role of Monte Carlo simulations," *Physics in Medicine and Biology*, 2012, ISSN: 0031-9155. DOI: 10.1088/0031-9155/57/11/R99.

[8] C.-H. Min, C. H. Kim, M.-Y. Youn, and J.-W. Kim, "Prompt gamma measurements for locating the dose falloff region in the proton therapy," *Applied Physics Letters*, vol. 89, no. 18, p. 183 517, Oct. 2006, ISSN: 0003-6951. DOI: 10.1063/1.2378561.

[9]   M. Moteabbed, S. España, and H. Paganetti, "Monte Carlo patient study on the comparison of prompt gamma and PET imaging for range verification in proton therapy," *Physics in Medicine and Biology*, vol. 56, no. 4, pp. 1063–1082, 2011, ISSN: 00319155. DOI: 10.1088/0031-9155/56/4/012.

[10]  V. Bom, L. Joulaeizadeh, and F. Beekman, "Real-time prompt gamma monitoring in spot-scanning proton therapy using imaging through a knife-edge-shaped slit," *Physics in Medicine and Biology*, vol. 57, no. 2, pp. 297–308, 2012, ISSN: 00319155. DOI: 10.1088/0031-9155/57/2/297.

[11]  J. C. Polf, S. Peterson, M. McCleskey, B. T. Roeder, A. Spiridon, S. Beddar, and L. Trache, "Measurement and calculation of characteristic prompt gamma ray spectra emitted during proton irradiation," *Physics in Medicine and Biology*, vol. 54, no. 22, 2009, ISSN: 00319155. DOI: 10.1088/0031-9155/54/22/N02.

[12]  R. J. Murphy, B. Kozlovsky, and R. Ramaty, "Nuclear deexcitation gamma-ray lines from accelerated particle interactions," pp. 523–541, 2002.

[13]  F. L. Lang, C. W. Werntz, C. J. Crannell, J. I. Trombka, and C. C. Chang, "Cross sections for production of the 15.10-MeV and other astrophysically significant gamma-ray lines through excitation and spallation of C12 and O16 with protons," *Physical Review C*, vol. 35, no. 4, pp. 1214–1227, 1987, ISSN: 05562813. DOI: 10.1103/PhysRevC.35.1214.

[14]  J. M. Verburg, H. A. Shih, and J. Seco, "Simulation of prompt gamma-ray emission during proton radiotherapy," *Physics in Medicine and Biology*, vol. 57, no. 17, pp. 5459–5472, 2012, ISSN: 00319155. DOI: 10.1088/0031-9155/57/17/5459.

[15]  J. M. Verburg and J. Seco, "Proton range verification through prompt gamma-ray spectroscopy," *Physics in Medicine and Biology*, vol. 59, no. 23, pp. 7089–7106, 2014, ISSN: 13616560. DOI: 10.1088/0031-9155/59/23/7089.

[16]  J. Kiener, M. Berheide, N. L. Achouri, A. Boughrara, A. Coc, A. Lefebvre, F. de Oliveira Santos, and C. Vieu, "$\gamma$ -ray production by inelastic proton scattering on 16O and 12C," *Physical Review C*, vol. 58, no. 4, pp. 2174–2179, 1998, ISSN: 0556-2813. DOI: 10.1103/physrevc.58.2174.

[17]  F. Hueso-González, F. Fiedler, C. Golnik, T. Kormoll, G. Pausch, J. Petzoldt, K. E. Römer, and W. Enghardt, "Compton Camera and Prompt Gamma Ray Timing: Two Methods for In Vivo Range Assessment in Pro-

ton Therapy," *Frontiers in Oncology*, vol. 6, 2016, ISSN: 2234-943X. DOI: 10.3389/fonc.2016.00080.

[18] I. Perali, A. Celani, L. Bombelli, C. Fiorini, F. Camera, E. Clementel, S. Henrotin, G. Janssens, D. Prieels, F. Roellinghoff, J. Smeets, F. Stichelbaut, and F. V. Stappen, "Prompt gamma imaging of proton pencil beams at clinical dose rate," *Physics in Medicine and Biology*, vol. 59, no. 19, pp. 5849–5871, 2014, ISSN: 13616560. DOI: 10.1088/0031-9155/59/19/5849.

[19] M. Priegnitz, S. Helmbrecht, G. Janssens, I. Perali, J. Smeets, F. Vander Stappen, E. Sterpin, and F. Fiedler, "Detection of mixed-range proton pencil beams with a prompt gamma slit camera," *Physics in Medicine and Biology*, vol. 61, no. 2, pp. 855–871, 2016, ISSN: 13616560. DOI: 10.1088/0031-9155/61/2/855.

[20] C. Richter, G. Pausch, S. Barczyk, M. Priegnitz, I. Keitz, J. Thiele, J. Smeets, F. V. Stappen, L. Bombelli, C. Fiorini, L. Hotoiu, I. Perali, D. Prieels, W. Enghardt, and M. Baumann, "First clinical application of a prompt gamma based in vivo proton range verification system," *Radiotherapy and Oncology*, vol. 118, no. 2, pp. 232–237, 2016, ISSN: 18790887. DOI: 10.1016/j.radonc.2016.01.004.

[21] C. H. Min, J. W. Kim, M. Y. Youn, and C. H. Kim, "Determination of distal dose edge location by measuring right-angled prompt-gamma rays from a 38 MeV proton beam," *Nuclear Instruments and Methods in Physics Research, Section A: Accelerators, Spectrometers, Detectors and Associated Equipment*, 2007, ISSN: 01689002. DOI: 10.1016/j.nima.2007.05.235.

[22] C. H. Min, H. R. Lee, C. H. Kim, and S. B. Lee, "Development of array-type prompt gamma measurement system for in vivo range verification in proton therapy," *Medical Physics*, vol. 39, no. 4, pp. 2100–2107, 2012, ISSN: 00942405. DOI: 10.1118/1.3694098.

[23] M. Pinto, D. Dauvergne, N. Freud, J. Krimmer, J. M. Letang, C. Ray, F. Roellinghoff, and E. Testa, "Design optimisation of a TOF-based collimated camera prototype for online hadrontherapy monitoring," *Physics in Medicine and Biology*, vol. 59, no. 24, pp. 7653–7674, 2014, ISSN: 13616560. DOI: 10.1088/0031-9155/59/24/7653.

[24] D. Kim, H. Yim, and J.-W. Kim, "Pinhole Camera Measurements of Prompt Gamma-rays for Detection of Beam Range Variation in Proton Therapy," *Journal of the Korean Physical Society*, vol. 55, no. 4, p. 1673, 2009, ISSN: 0374-4884. DOI: 10.3938/jkps.55.1673.

[25]  J. Smeets, F. Roellinghoff, D. Prieels, F. Stichelbaut, A. Benilov, P. Busca, C. Fiorini, R. Peloso, M. Basilavecchia, and T. Frizzi, "Prompt Gamma Imaging with a slit camera for real-time range control in proton therapy," *Physics in medicine and biology*, vol. 57, no. 11, pp. 3371–3405, 2012, ISSN: 0031-9155. DOI: 10.1088/0031-9155/57/11/3371.

[26]  F. Roellinghoff, A. Benilov, D. Dauvergne, G. Dedes, N. Freud, G. Janssens, J. Krimmer, J. M. Létang, M. Pinto, D. Prieels, C. Ray, J. Smeets, F. Stichelbaut, and E. Testa, "Real-time proton beam range monitoring by means of prompt-gamma detection with a collimated camera," *Physics in Medicine and Biology*, vol. 59, no. 5, pp. 1327–1338, 2014, ISSN: 00319155. DOI: 10.1088/0031-9155/59/5/1327.

[27]  G. W. Phillips, "Gamma-ray imaging with Compton cameras," *Nuclear Inst. and Methods in Physics Research, B*, vol. 99, no. 1-4, pp. 674–677, 1995, ISSN: 0168583X. DOI: 10.1016/0168-583X(95)80085-9.

[28]  D. Everett, J. Fleming, R. Todd, and J. Nightingale, "Gamma-radiation imaging system based on the Compton effect," *Proceedings of the Institution of Electrical Engineers*, vol. 124, no. 11, p. 995, 1977, ISSN: 00203270. DOI: 10.1049/piee.1977.0203.

[29]  T. Werner, J. Berthold, F. Hueso-González, T. Koegler, J. Petzoldt, K. Roemer, C. Richter, A. Rinscheid, A. Straessner, W. Enghardt, and G. Pausch, "Processing of prompt gamma-ray timing data for proton range measurements at a clinical beam delivery," *Physics in Medicine & Biology*, vol. 64, no. 10, p. 105 023, May 2019, ISSN: 1361-6560. DOI: 10.1088/1361-6560/ab176d.

[30]  M. McCleskey, W. Kaye, D. S. Mackin, S. Beddar, Z. He, and J. C. Polf, "Evaluation of a multistage CdZnTe Compton camera for prompt $\gamma$ imaging for proton therapy," *Nuclear Instruments and Methods in Physics Research, Section A: Accelerators, Spectrometers, Detectors and Associated Equipment*, vol. 785, pp. 163–169, 2015, ISSN: 01689002. DOI: 10.1016/j.nima.2015.02.030.

[31]  E. Draeger, D. Mackin, S. Peterson, H. Chen, S. Beddar, and J. Polf, *SU-F-J-189: A Method to Improve the Spatial Resolution of Prompt Gamma Based Compton Imaging for Proton Range Verification.* Jun. 2016, vol. 43, p. 3451. DOI: 10.1118/1.4956097.

[32]  J. C. Polf, S. Avery, D. S. Mackin, and S. Beddar, "Imaging of prompt gamma rays emitted during delivery of clinical proton beams with a Compton camera: feasibility studies for range verification," *Physics in Medicine and Biology*, vol. 60, no. 18, pp. 7085–7099, Sep. 2015. DOI: 10.1088/0031-9155/60/18/7085.

[33]  G. Llosá, J. Barrio, J. Cabello, A. Crespo, C. Lacasta, M. Rafecas, S. Callier, C. De La Taille, and L. Raux, "Detector characterization and first coincidence tests of a Compton telescope based on LaBr3crystals and SiPMs," in *Nuclear Instruments and Methods in Physics Research, Section A: Accelerators, Spectrometers, Detectors and Associated Equipment*, vol. 695, 2012, pp. 105–108, ISBN: 9781467301183. DOI: 10.1016/j.nima.2011.11.041.

[34]  G. Llosá, M. Trovato, J. Barrio, A. Etxebeste, E. Muñoz, C. Lacasta, J. F. Oliver, M. Rafecas, C. Solaz, and P. Solevi, "First Images of a Three-Layer Compton Telescope Prototype for Treatment Monitoring in Hadron Therapy," *Frontiers in Oncology*, vol. 6, 2016. DOI: 10.3389/fonc.2016.00014.

[35]  P. Solevi, E. Muñoz, C. Solaz, M. Trovato, P. Dendooven, J. E. Gillam, C. Lacasta, J. F. Oliver, M. Rafecas, I. Torres-Espallardo, and G. Llosá, "Performance of MACACO Compton telescope for ion-beam therapy monitoring: First test with proton beams," *Physics in Medicine and Biology*, vol. 61, no. 14, pp. 5149–5165, 2016, ISSN: 13616560. DOI: 10.1088/0031-9155/61/14/5149.

[36]  A. Kishimoto, J. Kataoka, T. Nishiyama, T. Taya, and S. Kabuki, "Demonstration of three-dimensional imaging based on handheld Compton camera," *Journal of Instrumentation*, vol. 10, no. 11, 2015. DOI: 10.1088/1748-0221/10/11/P11001.

[37]  T. Taya, J. Kataoka, A. Kishimoto, Y. Iwamoto, A. Koide, T. Nishio, S. Kabuki, and T. Inaniwa, "First demonstration of real-time gamma imaging by using a handheld Compton camera for particle therapy," *Nuclear Instruments and Methods in Physics Research, Section A: Accelerators, Spectrometers, Detectors and Associated Equipment*, vol. 831, pp. 355–361, 2016, ISSN: 01689002. DOI: 10.1016/j.nima.2016.04.028.

[38]  F. Roellinghoff, M. H. Richard, M. Chevallier, J. Constanzo, D. Dauvergne, N. Freud, P. Henriquet, F. Le Foulher, J. M. Létang, G. Montarou, C. Ray, E. Testa, M. Testa, and A. H. Walenta, "Design of a Compton camera for 3D prompt-$\gamma$ imaging during ion beam therapy," *Nuclear Instruments and Methods in Physics Research, Section A: Accelerators, Spectrometers, Detectors*

*and Associated Equipment*, vol. 648, no. SUPPL. 1, 2011, ISSN: 01689002. DOI: 10.1016/j.nima.2011.01.069.

[39] M. Fontana, J.-L. Ley, D. Dauvergne, N. Freud, J. Krimmer, J. M. Letang, V. Maxim, M.-H. Richard, I. Rinaldi, and E. Testa, "Monitoring Ion Beam Therapy With a Compton Camera: Simulation Studies of the Clinical Feasibility," *IEEE Transactions on Radiation and Plasma Medical Sciences*, vol. 4, no. 2, pp. 218–232, 2019, ISSN: 2469-7311. DOI: 10.1109/trpms.2019.2933985.

[40] P. Thirolf, S. Aldawood, C. Lang, and K. Parodi, "SU-E-I-80: Development of a Compton Camera for Online Range Monitoring of Laser-Accelerated Proton Beams," in *Medical Physics*, vol. 40, 2013, p. 144, ISBN: 2014661103. DOI: 10.1118/1.4814191.

[41] C. Golnik, D. Bemmerer, W. Enghardt, F. Fiedler, F. Hueso-González, G. Pausch, K. Römer, H. Rohling, S. Schöne, L. Wagner, and T. Kormoll, "Tests of a Compton imaging prototype in a monoenergetic 4.44 MeV photon field—a benchmark setup for prompt gamma-ray imaging devices," *Journal of Instrumentation*, vol. 11, no. 06, P06009–P06009, Jun. 2016. DOI: 10.1088/1748-0221/11/06/P06009.

[42] C. Hyeong Kim, J. Hyung Park, H. Seo, and H. Rim Lee, "Gamma electron vertex imaging and application to beam range verification in proton therapy," *Medical Physics*, vol. 39, no. 2, pp. 1001–1005, 2012, ISSN: 00942405. DOI: 10.1118/1.3662890.

[43] H. R. Lee, S. H. Kim, J. H. Park, W. G. Jung, H. Lim, and C. H. Kim, "Prototype system for proton beam range measurement based on gamma electron vertex imaging," *Nuclear Instruments and Methods in Physics Research, Section A: Accelerators, Spectrometers, Detectors and Associated Equipment*, vol. 857, pp. 82–97, 2017, ISSN: 01689002. DOI: 10.1016/j.nima.2017.03.022.

[44] Glenn F. Knoll, *Radiation Detection and Measurement*, 1. 2010, pp. 1–5. DOI: 10.1007/s13398-014-0173-7.2.

[45] G. Lutz, *Semiconductor Radiation Detectors*. Springer Berlin Heidelberg, 2007. DOI: 10.1007/978-3-540-71679-2.

[46] S. M. Sze and K. K. Ng, "Physics of Semiconductor Devices, 3rd Edition - Simon M. Sze, Kwok K. Ng," *Physics of Semiconductor Devices, 3rd Edition.; John Wiley & Sons, Inc.; NJ*, 2007.

[47] O. Klein and Y. Nishina, *The scattering of light by free electrons according to Dirac's new relativistic dynamics [2]*, 1928. DOI: 10.1038/122398b0.

[48] D. A. Neamen, *Semiconductor Physics and Devices Basic Principles.* 2006, ISBN: 0072321075.

[49] W. Shockley, "Currents to conductors induced by a moving point charge," *Journal of Applied Physics*, vol. 9, no. 10, pp. 635–636, Apr. 1938, ISSN: 00218979. DOI: 10.1063/1.1710367.

[50] M. Nakhostin, *Signal processing for radiation detectors.* 2017. DOI: 10.1002/9781119410225.

[51] L. J. Harkness, D. S. Judson, A. J. Boston, H. C. Boston, J. R. Cresswell, P. J. Nolan, A. Sweeney, J. Beau, M. Lampert, B. Pirard, and M. Zuvic, "Characterisation of a Si(Li) orthogonal-strip detector," *Nuclear Instruments and Methods in Physics Research, Section A: Accelerators, Spectrometers, Detectors and Associated Equipment*, vol. 726, pp. 52–59, 2013, ISSN: 01689002. DOI: 10.1016/j.nima.2013.05.143.

[52] E. J. Rintoul, "Characterisation of an Electrically Cooled Planar Germanium Detector for use in the GRI+ Compton Camera System," Ph.D. dissertation, University of liverpool, 2020.

[53] E. Rintoul, A. J. Boston, H. C. Boston, A. Caffrey, J. R. Cresswell, L. J. Harkness-Brennan, D. S. Judson, P. J. Nolan, J. Platt, C. Unsworth, T. F. Woodroof, I. H. Lazarus, J. Simpson, J. Cocks, D. Walker, B. Pirard, and P. Quirin, "Characterisation of the charge collection properties in a segmented planar HPGe detector," *Nuclear Instruments and Methods in Physics Research, Section A: Accelerators, Spectrometers, Detectors and Associated Equipment*, vol. 987, no. September 2020, p. 164 804, 2021, ISSN: 01689002. DOI: 10.1016/j.nima.2020.164804.

[54] CAEN, "User Manual UM3248 V1724," Tech. Rep., 2018. [Online]. Available: www.caen.it/support-services/documentation-area.

[55] ——, "User Manual UM6769_724-781_782_DPP_PHA_Registers," Tech. Rep., 2020. [Online]. Available: www.caen.it/support-services/documentation-area.

[56] ——, "V1495_Technical Information Manual," Tech. Rep. July, 2008. [Online]. Available: http://www.caen.it/csite/LibrarySearch.jsp.

[57] *Multi Instance Data Acquisition System.* [Online]. Available: http://npg.dl.ac.uk/MIDAS/.

[58] A. Georgiev, W. Gast, and R. M. Lieder, "An analog-to-digital conversion based on a moving window deconvolution," *IEEE Transactions on Nuclear Science*, vol. 41, no. 4, pp. 1116–1124, 1994, ISSN: 1558-1578 VO - 41. DOI: 10.1109/23.322868.

[59] J. Cresswell and J. Sampson, "MTsort Language - EDOC033," 2009. [Online]. Available: http://ns.ph.liv.ac.uk/MTsort-manual/edoc033.pdf.

[60] R. J. Cooper, A. J. Boston, H. C. Boston, J. R. Cresswell, A. N. Grint, L. J. Harkness, P. J. Nolan, D. C. Oxley, D. P. Scraggs, I. Lazarus, J. Simpson, and J. Dobson, "Charge collection performance of a segmented planar high-purity germanium detector," *Nuclear Instruments and Methods in Physics Research, Section A: Accelerators, Spectrometers, Detectors and Associated Equipment*, vol. 595, no. 2, pp. 401–409, 2008, ISSN: 01689002. DOI: 10.1016/j.nima.2008.07.106.

[61] A. Caffrey, "The Development and Evaluation of a Compton Camera for Imaging Spent Fuel Rod Assemblies by," Ph.D. dissertation, University of Liverpool, 2019.

[62] E. Rintoul, A. Boston, H. Boston, A. Caffrey, L. Harkness-Brennan, D. Judson, P. Nolan, J. Platt, C. Unsworth, J. Wright, T. Woodroof, and P. Quirin, "Simulation and validation of a planar HPGe detector signal database for use in pulse shape analysis," *Nuclear Instruments and Methods in Physics Research Section A: Accelerators, Spectrometers, Detectors and Associated Equipment*, vol. 1034, no. April, p. 166 641, 2022, ISSN: 01689002. DOI: 10.1016/j.nima.2022.166641.

[63] R. J. Cooper, "Performance of the SmartPET Positron Emission Tomography System for Small Animal Imaging," Ph.D. dissertation, University of Liverpool, 2007.

[64] T. Woodroof, "Quantitative Compton Imaging of Caesium-137 in Porous Media," Ph.D. dissertation, University of Liverpool, 2019.

[65] A. Cesana and M. Terrani, "An empirical method for peak-to-total ratio computation of a gamma-ray detector," *Nuclear Instruments and Methods in Physics Research Section A: Accelerators, Spectrometers, Detectors and Associated Equipment*, vol. 281, no. 1, pp. 172–175, 1989, ISSN: 0168-9002.

[66] P. P. Aguiar-Amado, V. A. Amado, and J. C. Aguiar, "Full-energy peak determination from total efficiency and peak-to-total ratio calculations," *Nuclear Instruments and Methods in Physics Research Section A: Accelerators,*

*Spectrometers, Detectors and Associated Equipment*, vol. 990, p. 164 980, 2021.

[67] CAEN, "Manual of Digital Pulse Height Analyzer for 724 series compliant with DPP- PHA firmware," Tech. Rep. 2, 2013, p. 46. DOI: 10.1049/esn.1986.0048.

[68] J. Yap, J. Resta-López, A. Kacperek, R. Schnuerer, S. Jolly, S. Boogert, and C. Welsch, "Beam characterisation studies of the 62 MeV proton therapy beamline at the Clatterbridge Cancer Centre," *Physica Medica*, vol. 77, no. August, pp. 108–120, 2020, ISSN: 1724191X. DOI: 10.1016/j.ejmp.2020.08.002.

[69] A. Kacperek, "Dose verification by activation in vivo following proton beam eye radiotherapy," *Journal of Radioanalytical and Nuclear Chemistry*, vol. 271, no. 3, pp. 731–740, 2007, ISSN: 02365731. DOI: 10.1007/s10967-007-0334-7.

[70] Oak Ridge National Laboratory, "GF3," 2019. [Online]. Available: https://radware.phy.ornl.gov/gf3/.

[71] A. Belhout, J. Kiener, A. Coc, J. Duprat, C. Engrand, C. Fitoussi, M. Gounelle, A. Lefebvre-Schuhl, N. De Séréville, V. Tatischeff, J. P. Thibaud, M. Chabot, F. Hammache, and H. Benhabiles-Mezhoud, "$\gamma$-ray production by proton and $\alpha$-particle induced reactions on C12, O16, Mg24, and Fe," *Physical Review C - Nuclear Physics*, vol. 76, no. 3, pp. 1–19, 2007, ISSN: 1089490X. DOI: 10.1103/PhysRevC.76.034607.

[72] C. E. Ordonez, "Angular uncertainties due to geometry and spatial resolution in compton cameras," *IEEE Transactions on Nuclear Science*, vol. 46, no. 4 PART 2, pp. 1142–1147, 1999, ISSN: 00189499. DOI: 10.1109/23.790848.